

REPORT DOCUMENTATION PAGE			Form Approved OMB NO. 0704-0188		
<p>The public reporting burden for this collection of information is estimated to average 1 hour per response, including the time for reviewing instructions, searching existing data sources, gathering and maintaining the data needed, and completing and reviewing the collection of information. Send comments regarding this burden estimate or any other aspect of this collection of information, including suggestions for reducing this burden, to Washington Headquarters Services, Directorate for Information Operations and Reports, 1215 Jefferson Davis Highway, Suite 1204, Arlington VA, 22202-4302. Respondents should be aware that notwithstanding any other provision of law, no person shall be subject to any penalty for failing to comply with a collection of information if it does not display a currently valid OMB control number.</p> <p>PLEASE DO NOT RETURN YOUR FORM TO THE ABOVE ADDRESS.</p>					
1. REPORT DATE (DD-MM-YYYY) 01-10-2013		2. REPORT TYPE Final Report		3. DATES COVERED (From - To) 1-Jul-2009 - 30-Jun-2013	
4. TITLE AND SUBTITLE Final Report: Non-Catalytic Reforming with Applications to Portable Power			5a. CONTRACT NUMBER W911NF-09-1-0176		
			5b. GRANT NUMBER		
			5c. PROGRAM ELEMENT NUMBER 611102		
6. AUTHORS Janet L. Ellzey, Erica Belmont, Colin H. Smith			5d. PROJECT NUMBER		
			5e. TASK NUMBER		
			5f. WORK UNIT NUMBER		
7. PERFORMING ORGANIZATION NAMES AND ADDRESSES University of Texas at Austin 101 East 27th Street Suite 5.300 Austin, TX 78712 -1539			8. PERFORMING ORGANIZATION REPORT NUMBER		
9. SPONSORING/MONITORING AGENCY NAME(S) AND ADDRESS(ES) U.S. Army Research Office P.O. Box 12211 Research Triangle Park, NC 27709-2211			10. SPONSOR/MONITOR'S ACRONYM(S) ARO		
			11. SPONSOR/MONITOR'S REPORT NUMBER(S) 55985-EG.17		
12. DISTRIBUTION AVAILABILITY STATEMENT Approved for Public Release; Distribution Unlimited					
13. SUPPLEMENTARY NOTES The views, opinions and/or findings contained in this report are those of the author(s) and should not be construed as an official Department of the Army position, policy or decision, unless so designated by other documentation.					
14. ABSTRACT Fuel cells are a promising technology as an alternative for portable power applications, because they offer higher power densities, do not include moving parts, and thus are free of noise and vibrations. At the current state of development, fuel cell systems cannot effectively use hydrocarbon fuels unless they have been processed, or reformed, into a syngas consisting of hydrogen, carbon monoxide, and other species. Conventional reforming technologies utilize catalysts which may have strict requirements on fuel purity and operating conditions. The					
15. SUBJECT TERMS reforming, syngas, portable power, rich combustion, lean combustion					
16. SECURITY CLASSIFICATION OF:		17. LIMITATION OF ABSTRACT		15. NUMBER OF PAGES	19a. NAME OF RESPONSIBLE PERSON
a. REPORT UU	b. ABSTRACT UU	c. THIS PAGE UU	UU		Janet Ellzey
					19b. TELEPHONE NUMBER 512-471-7020

## Report Title

Final Report: Non-Catalytic Reforming with Applications to Portable Power

### ABSTRACT

Fuel cells are a promising technology as an alternative for portable power applications, because they offer higher power densities, do not include moving parts, and thus are free of noise and vibrations. At the current state of development, fuel cell systems cannot effectively use hydrocarbon fuels unless they have been processed, or reformed, into a syngas consisting of hydrogen, carbon monoxide, and other species. Conventional reforming technologies utilize catalysts which may have strict requirements on fuel purity and operating conditions. The development of a robust non-catalytic technique has the advantage of using a variety of logistics fuels. In this project, conversion of various fuels was demonstrated in two different non-catalytic reactors. The conversion of butanol and Jet-A were demonstrated in a filtration reactor consisting of a packed bed of spheres. A second reactor, consisting of counterflowing channels, has the advantage of stationary reactions zones and the ability to operate continuously. Conversion of heptane was demonstrated in this reactor and a computational study was conducted to understand the scaling of the reactor for various applications. These results show the promise of non-catalytic technologies for the reforming of a wide range of fuels.

---

**Enter List of papers submitted or published that acknowledge ARO support from the start of the project to the date of this printing. List the papers, including journal references, in the following categories:**

**(a) Papers published in peer-reviewed journals (N/A for none)**

<u>Received</u>	<u>Paper</u>
06/27/2013	12.00 Colin H. Smith, Daniel I. Pineda, Janet L. Ellzey. Syngas production from burner-stabilized methane/air flames: The effect of preheated reactants, Combustion and Flame, (03 2013): 0. doi: 10.1016/j.combustflame.2012.10.022
06/27/2013	13.00 Colin H. Smith, Daniel I. Pineda, Casey D. Zak, Janet L. Ellzey. Conversion of jet fuel and butanol to syngas by filtration combustion, International Journal of Hydrogen Energy, (12 2012): 0. doi: 10.1016/j.ijhydene.2012.10.102
08/30/2012	11.00 Erica L. Belmont, Sam M. Solomon, Janet L. Ellzey. Syngas production from heptane in a non-catalytic counter-flow reactor, Combustion and Flame, (07 2012): 0. doi: 10.1016/j.combustflame.2012.07.001
10/01/2013	16.00 Erica L. Belmont, Ingmar Schoegl, Janet L. Ellzey. Experimental and analytical investigation of lean premixed methane/air combustion in a mesoscale counter-flow reactor, Proceedings of the Combustion Institute, (01 2013): 3361. doi: 10.1016/j.proci.2012.06.087
<b>TOTAL:</b>	<b>4</b>

**Number of Papers published in peer-reviewed journals:**

---

**(b) Papers published in non-peer-reviewed journals (N/A for none)**

Received          Paper

**TOTAL:**

**Number of Papers published in non peer-reviewed journals:**

---

**(c) Presentations**

**Number of Presentations:**      0.00

---

**Non Peer-Reviewed Conference Proceeding publications (other than abstracts):**

Received          Paper

04/08/2010	1.00	C. Smith, C. Zak, J. Ellzey. Conversion of Bio-butanol to Syngas via Filtration Combustion, . . . ,
04/08/2010	2.00	E. Belmont, J. Ellzey. Experimental Study of Syngas Production in a Non-Catalytic Counterflow Reactor, . . . ,
06/27/2013	14.00	Erica Belmont, Janet Ellzey. Lean Combustion of Propane in a Non-Catalytic Mesoscale Counter-flow Reactor, 8th US National Combustion Meeting. 2013/05/19 01:00:00, . . . ,
08/24/2011	4.00	Casey Zak, Daniel Pineda, Janet Ellzey, Colin Smith. Conversion of Jet A to Syngas by Filtration Combustion, 7th US Technical Meeting of the Combustion Institute. 2011/03/20 01:00:00, . . . ,
08/24/2011	3.00	Erica Belmont, Sam Solomon, Janet Ellzey. Syngas Production from Heptane in a Non-Catalytic Counterflow Reactor, 7th US National Technical Meeting of the Combustion Institute. 2011/03/20 01:00:00, . . . ,
08/30/2012	8.00	Erica Belmont, Sam Solomon, Janet. Ellzey. Impact of Operating Conditions on Syngas Production from Hydrocarbon Fuels in the Counter-Flow Reactor, 2011 Fall Technical Meeting of the Western States Section of the Combustion Institute. 2011/10/17 01:00:00, . . . ,
08/30/2012	9.00	Colin Smith, Daniel Pineda, Janet Ellzey. Effect of preheating on rich combustion for syngas production: experiments and modeling of burner-stabilized flames, 2011 Fall Technical Meeting Of the Western States Section of the Combustion Institute. 2012/10/17 01:00:00, . . . ,

**TOTAL:**                      **7**

Number of Non Peer-Reviewed Conference Proceeding publications (other than abstracts):

---

**Peer-Reviewed Conference Proceeding publications (other than abstracts):**

Received            Paper

**TOTAL:**

Number of Peer-Reviewed Conference Proceeding publications (other than abstracts):

---

**(d) Manuscripts**

Received            Paper

06/27/2013	15.00	Erica Belmont, Janet Ellzey. Lean Combustion in a Non-Catalytic Mesoscale Counter-flow Reactor, Combustion and Flame (06 2013)
08/30/2012	6.00	Erica Belmont, Ingmar Schoegl, Janet Ellzey. Experimental and Analytical Investigation of Lean Premixed Methane/Air Combustion in a Mesoscale Counter-Flow Reactor, Proceedings of the Combustion Institute (01 2012)
08/30/2012	7.00	Colin Smith, Daniel Pineda, Janet Ellzey. Syngas Production From Burner-Stabilized Methane/Air Flames: The Effect of Preheated Reactants, Combustion and Flame (05 2012)
08/31/2011	5.00	Erica Belmont, Sam Solomon, Janet Ellzey. Syngas Production from Heptane in a Non-Catalytic Counter-Flow Reactor, Combustion and Flame (08 2011)

**TOTAL:            4**

Number of Manuscripts:

---

**Books**

Received            Paper

**TOTAL:**

**Patents Submitted**

---

**Patents Awarded**

---

**Awards**

---

**Graduate Students**

<u>NAME</u>	<u>PERCENT SUPPORTED</u>	Discipline
Erica Belmont	0.50	
Colin Smith	0.25	
<b>FTE Equivalent:</b>	<b>0.75</b>	
<b>Total Number:</b>	<b>2</b>	

**Names of Post Doctorates**

<u>NAME</u>	<u>PERCENT SUPPORTED</u>
<b>FTE Equivalent:</b>	
<b>Total Number:</b>	

**Names of Faculty Supported**

<u>NAME</u>	<u>PERCENT SUPPORTED</u>	National Academy Member
Janet Ellzey	0.00	
<b>FTE Equivalent:</b>	<b>0.00</b>	
<b>Total Number:</b>	<b>1</b>	

**Names of Under Graduate students supported**

<u>NAME</u>	<u>PERCENT SUPPORTED</u>
<b>FTE Equivalent:</b>	
<b>Total Number:</b>	

**Student Metrics**

This section only applies to graduating undergraduates supported by this agreement in this reporting period

- The number of undergraduates funded by this agreement who graduated during this period: ..... 0.00
- The number of undergraduates funded by this agreement who graduated during this period with a degree in science, mathematics, engineering, or technology fields:..... 0.00
- The number of undergraduates funded by your agreement who graduated during this period and will continue to pursue a graduate or Ph.D. degree in science, mathematics, engineering, or technology fields:..... 0.00
- Number of graduating undergraduates who achieved a 3.5 GPA to 4.0 (4.0 max scale):..... 0.00
- Number of graduating undergraduates funded by a DoD funded Center of Excellence grant for Education, Research and Engineering:..... 0.00
- The number of undergraduates funded by your agreement who graduated during this period and intend to work for the Department of Defense ..... 0.00
- The number of undergraduates funded by your agreement who graduated during this period and will receive scholarships or fellowships for further studies in science, mathematics, engineering or technology fields: ..... 0.00

**Names of Personnel receiving masters degrees**

<u>NAME</u>
<b>Total Number:</b>

**Names of personnel receiving PHDs**

<u>NAME</u>
Colin H. Smith
<b>Total Number:</b> 1

**Names of other research staff**

<u>NAME</u>	<u>PERCENT SUPPORTED</u>
<b>FTE Equivalent:</b>	
<b>Total Number:</b>	

**Sub Contractors (DD882)**

**Inventions (DD882)**

**Scientific Progress**

See Attachment

**Technology Transfer**

ARO Final Report on  
**Non-catalytic Reforming with Applications to Portable Power**  
*Army Research Office grant number W911NF-09-1-017*

Table of Contents

	Page #
List of Appendixes, figures, and tables	2
1. Statement of problem	3
2. Summary of most important results	5
3. Bibliography	10
4. Appendixes	12

## List of Appendixes

- A. Non-catalytic reforming of butanol and Jet-A
- B. Reforming of heptane in counterflow reactor
- C. Critical design parameters for counterflow reactor
- D. Operation of the counterflow reactor at lean conditions
- E. Effect of preheat on premixed methane/air flames

# 1 Statement of the problem

Dramatic innovations in mission critical electronic equipment have led to an increased demand for portable power in the field. In addition, advances in small mobile autonomous robotic devices, e.g. unmanned aerial vehicles (UAV's) or unmanned ground vehicles (UGV's), as well as biomechatronic exoskeletons [Pons, 2008] are limited by power demands that go beyond the capabilities of current battery technologies. Replacing batteries by fuel cells is a promising approach, as fuel cells offer higher power densities, do not include moving parts, and thus are free of noise and vibrations. If deployed, fuel cell based power systems can greatly reduce the weight burden compared to conventional batteries, ease refueling, and increase mission duration.

At the current state of development, fuel cell systems face the critical issue of hydrogen generation and storage [NRC, 2002]. A potential solution to this problem is fuel reforming, where a hydrogen-rich syngas is generated from liquid hydrocarbon fuels. Liquid hydrocarbons have the advantage of high volumetric energy densities and an existing infrastructure with the potential of using standard battlefield fuels. Those fuels, however, are not tailored to the specific needs for fuel reforming and are further hampered by a high sulfur content of up to 0.3 wt% [MIL-DTL-83133F, 2008]. Fuel reforming based on conventional catalytic techniques is difficult, as operating conditions and fuel quality need to meet stringent requirements to prevent catalyst degradation due to excessive temperatures and sulfur poisoning [Moon et al., 2004]. An alternative approach is non-catalytic fuel reforming, which promises a more robust design due to the lack of damageable catalytic surfaces.

Non-catalytic fuel reformers have the advantage of not containing damageable catalytic surfaces and thus can operate at a wide range of temperatures with no restrictions regarding quality and sulfur content of the fuel. Optimal operating conditions for non-catalytic fuel reforming are in the very fuel-rich regime, either near or beyond the conventional rich flammability limit, where reaction rates are slow and some means of enhancing the rates is necessary for practical reactors. One option for enhancing the reaction rates is to recirculate heat such that local temperatures are *superadiabatic* i.e. higher than those predicted by equilibrium. The classic means of producing superadiabatic temperatures is by reaction of a fuel/air mixture in a *filtration reactor* consisting of a single flow channel filled with a porous matrix [Dhamrat and Ellzey, 2006; Fay, et al, 2005, Bingue, et al. 2002](Fig. 1.1a). Filtration combustion is characterized by a propagating reaction front that is self-sustaining once it is established. In the ultra-rich regime typical for fuel reforming, the reaction front propagates downstream (co-flowing) into a region where the solid has already been heated by the hot product gases, thus producing superadiabatic temperatures locally. The high local temperatures are sufficient to drive the reactions of mixtures that are otherwise not flammable. One of the major practical limitations, however, of the filtration reactor is that it cannot be operated continuously. Due to the downstream propagation, the reaction front ultimately reaches the end of the bed and the process must be restarted or the flow direction reversed, thus complicating the design of the reactor.

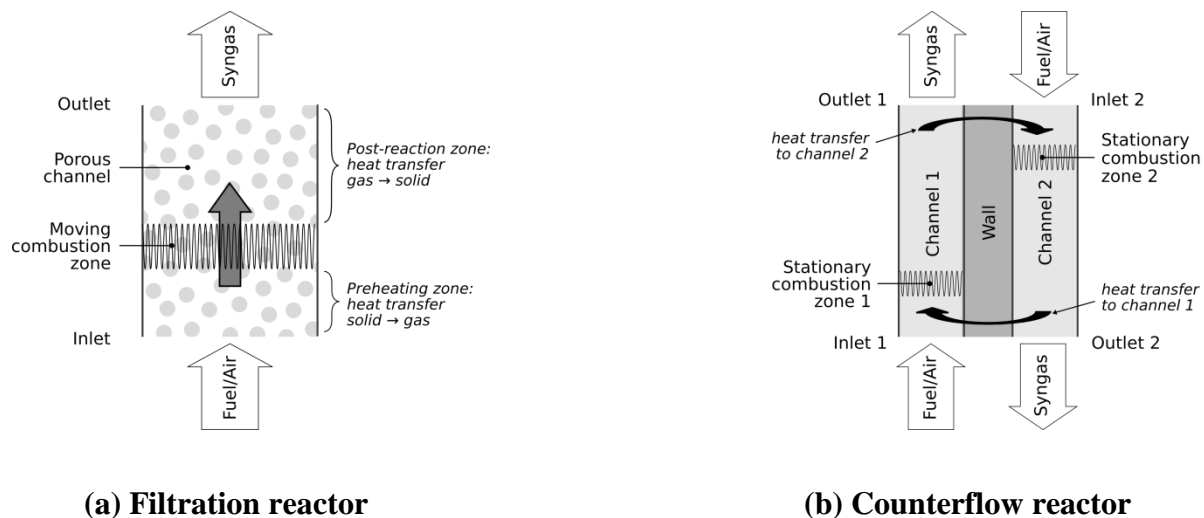


**Figure 1.1: Reactors used in this study**

In order to overcome the limited operation time of a filtration reactor, we have developed a novel *counterflow reactor* concept with stationary combustion zones [Schoegl and Ellzey, 2007; Schoegl and Ellzey 2009] that is capable of continuous operation. In this design, heat is transferred from hot reaction products to cold reactants across a wall dividing adjacent flow channels (Fig. 1.1b). The operating principle is based on preheating of the reactants by counterflow heat exchange, which enables combustion of otherwise non-flammable mixtures typical for fuel reforming. Thus, superadiabatic temperatures are attained with stationary reaction zones allowing continuous operation.

In the research conducted with ARO support, both reactor designs were used to study the feasibility of non-catalytic reforming of butanol, heptane and Jet-A. The more rugged filtration reactor (Fig. 1.1a) was used to demonstrate the conversion of butanol and Jet-A, and the counterflow reactor (Fig. 1.1b) was used for heptane. Together these results greatly increase our understanding of the potential for non-catalytic reforming.

## 1.1 Project Objectives

To address the challenges regarding the increasing power demands in portable or mobile devices, we investigated the principles of a compact, *non-catalytic* fuel reformer to produce a hydrogen-rich syngas from heptane, butanol, and Jet-A. The purpose of this project was to (1) demonstrate the principle of non-catalytic reforming of butanol and Jet-A, (2) demonstrate that liquid fuels can be reformed in the counterflow reactor, and (3) understand the critical design parameters controlling the conversion efficiency in the counterflow reactor and develop scaling laws for down-sizing the counterflow reactor for applications to systems with delivered power of 200-1000 W.

In Section 2, a summary of the major findings is presented. Sub-sections 2.1-2.3 discuss results related to the specific objectives of the project. Sub-sections 2.4 and 2.5 present additional results related to the project.

## **2 Summary of most important results**

In this section, the most important results from the study of non-catalytic conversion of liquid and gaseous fuels are presented. More detailed results are included in the appendixes.

### **2.1 Non-catalytic reforming of butanol and Jet-A**

Both butanol and Jet-A were successfully converted in the filtration reactor. Results of the conversion of butanol and jet fuel to syngas via non-catalytic transient filtration combustion are summarized: At maximum, about 42% of the hydrogen in jet fuel was converted to H<sub>2</sub> and 56% of carbon was converted to CO. The H<sub>2</sub> yield continued to increase with  $\phi$  in the jet fuel experiments whereas in the butanol experiments the yields for H<sub>2</sub> and CO both reached peaks within the tested operating range. The peak CO yield for experiments with butanol was 72% and the peak H<sub>2</sub> yield was 43%. Most of the chemical energy exiting the reactor was bound in H<sub>2</sub> and CO, but CH<sub>4</sub>, C<sub>2</sub>H<sub>2</sub> and C<sub>2</sub>H<sub>4</sub> were observed in substantial amounts in experiments with both fuels, especially in experiments with butanol at high  $\phi$ . In contrast, equilibrium predicted nearly negligible amounts of energy-containing compounds besides H<sub>2</sub>, CO and solid carbon.

Soot production proved to be substantial in experiments with both fuels, with the qualitative observation of soot from both fuels exceeding the soot production observed in similar experiments with methane, heptane, and ethanol. Soot production limited the maximum testable  $\phi$  for jet fuel experiments to  $\phi = 3.15$  since soot clogged the reactor when  $\phi$  exceeded this value. An analysis of the carbon balance for jet fuel experiments showed that up to 40% of the carbon entering the system was deposited on the porous medium. Similarly for butanol, the carbon balance showed significant loss up to  $\phi \sim 3$ . At the most extreme  $\phi$ , the reaction zone propagates downstream oxidizing some of the soot that has been deposited previously, resulting in an exhaust stream with more carbon atoms than are contained in the inlet fuel at the time of sample.

Equilibrium calculations and experimental results were analyzed to determine trends in fuel conversion efficiency as a function of fuel type. The equilibrium calculations predicted that larger fuel molecules would, generally, produce higher syngas yields, but the experimental results disagreed with this trend. Generally, experimental results show that smaller hydrocarbons produce higher syngas yields with jet fuel having the lowest hydrogen and carbon monoxide yields. The comparison of these equilibrium data with the experimental data available in the literature suggests that kinetic effects are very important in fuel conversion to syngas and equilibrium results should be interpreted carefully when predicting syngas production from the

combustion of very rich mixtures of fuel and air. Lastly, the demonstration of the conversion of jet fuel and butanol, along with previous demonstrations with methane, ethanol and heptane show the robustness of the non-catalytic filtration reactor.

Further details on the non-catalytic conversion of Jet-A and butanol are presented in Appendix A.

## **2.2 Reforming of heptane in counterflow reactor**

Experiments demonstrated the non-catalytic reforming of heptane to produce hydrogen-rich syngas in a counterflow reactor. A key advantage of this reactor is that the reaction zones are stationary, which permits continuous operation and practical applications. Stable operation of the reactor with premixed heptane/air reactants was established for equivalence ratios between 2.8 and 3.9 and inlet velocities between 50 cm/s and 200 cm/s. Peak wall temperatures were monitored throughout reactor operation and were at all points in excess of the adiabatic equilibrium temperature, thus excess-enthalpy flames were achieved through internal heat recirculation.

Exhaust gas composition was measured using gas chromatography for two sets of tests: equivalence ratio was varied from 2.9-3.8 with inlet velocity held constant at 125 cm/s, and equivalence ratio was held constant at 3.0 with inlet velocity varied from 50-200 cm/s. H<sub>2</sub> concentration decreased with increasing equivalence ratio from a maximum of 14.5% to a minimum of 10.6%, while CO concentration remained nearly constant around 17.0%. Both H<sub>2</sub> and CO concentrations showed little dependence overall on inlet velocity, with the former varying from 12.8-14.4% and the latter varying between 16.6-17.5%. The largest effect of inlet velocity was found at the lower end of the tested range where rates of heat release and temperatures are lower.

In all cases, unburned hydrocarbons were measured in excess of concentrations predicted by equilibrium composition. Total unburned hydrocarbon levels increased with increasing equivalence ratio. Soot was noted with significant formation observed at higher equivalence ratios and inlet velocities. These results and observations strongly suggested that the extent of fuel breakdown is reduced by insufficient reaction rate and residence time.

The results of this study showed trends similar to previously published studies on syngas production from methane and propane using the counterflow reactor [Schoegl and Ellzey, 2007; Schoegl and Ellzey 2009]. Each fuel had H<sub>2</sub> species and energy conversion efficiencies below equilibrium values, but total conversion efficiencies were comparable to equilibrium. In addition, energy-dense unburned hydrocarbon concentrations were in excess of equilibrium with concentrations an order of magnitude higher than predicted by equilibrium at the highest tested

equivalence ratios in this study. The comparison between the different fuels indicates that, although the stable operating range for heptane does include the theoretically optimal value as predicted by hydrogen conversion efficiencies calculated from equilibrium, the current reactor design does not permit complete fuel conversion at high equivalence ratios. In addition, the formation of soot at some conditions suggests the importance of operating at more moderate conditions for optimal performance.

This study demonstrated the fuel flexibility of the counterflow reactor by reforming a liquid fuel, and results supplemented previous reforming studies on the counterflow reactor. Peak H<sub>2</sub> conversion efficiency was significantly lower than that attained via filtration combustion in porous media, an alternate method of non-catalytic reforming. Differences were attributed to higher peak temperatures in the porous media reactor, which has higher specific surface area for heat transfer as compared to the counterflow reactor under investigation. Furthermore, although the tested equivalence ratio range in this study does include  $\phi = 2.9$ , where peak conversion efficiency is predicted to occur by equilibrium, previous studies predict peak conversion efficiencies over a range of  $\phi = 1.8$  to  $\phi = 3.5$ . The results of hydrogen conversion in this study indicate that the optimum equivalence ratio might be outside the operating range of the counterflow reactor.

Further details of non-catalytic reforming of heptane in the counterflow reactor are presented in Appendix B.

### **2.3 Critical design parameters for counterflow reactor**

A computational study was undertaken to determine the effect of geometric scale on fuel reforming in the meso-scale parallel-plate counterflow reactor. Length and height of the reactor channels were scaled relative to the original dimensions of the counterflow reactor that has been used in previous analytical and experimental investigations. Results were quantified in terms of steady state reactor operation, heat recirculation efficiency, temperature ratio, and hydrogen conversion efficiency.

Reactor operating range was found to be strongly impacted by channel scaling. Decreasing channel height resulted in a shift in stable operating range towards higher equivalence ratios. Decreasing channel length resulted in a significant narrowing of the stable equivalence ratio and inlet velocity ranges. Most stable operating points were above the conventional rich flammability limit and adiabatic flame speed of methane and air combustion based upon inlet conditions, which highlights the importance of heat recirculation in achieving operation of the counterflow reformer at these conditions.

Heat recirculation efficiency and temperature ratios were found to be significantly higher for reactors with decreased channel height. These findings indicate more effective heat recirculation with smaller channel height, where channel wall surface area-to-gas volume ratio is increased and the transverse distance for mass and heat diffusion is reduced. Channel length showed a less significant impact on heat recirculation, with shorter channel lengths producing slightly higher heat recirculation efficiencies and temperature ratios than longer lengths.

Hydrogen conversion efficiency decreased with increasing equivalence ratio for all reactors, with slightly higher conversion efficiencies found for smaller channel heights and lengths. Hydrogen conversion efficiency initially increased with inlet velocity at the lowest tested firing rates, and decreased at the highest tested inlet velocities, suggesting that an optimal firing rate exists.

Scaled down reactors were achieved by decreasing reactor channel height and length, although the latter resulted in a significantly narrowed stable range. The results of this study highlight the effectiveness of small scale reactor channels in achieving heat recirculation and significantly superadiabatic temperatures. These, in turn, permit the effective extension of flammability limits to stable operation at rich equivalence ratios. While increasing heat recirculation may be required to significantly extend the stable operating range, the results of this study suggest that superadiabatic temperatures serve to extend the flammable range of reactor operating points but otherwise do not strongly impact hydrogen conversion efficiencies.

Further details of the scaling study for the counterflow reactor are presented in Appendix C.

## **2.4 Operation of the counterflow reactor at lean conditions**

The funding from ARO was leveraged with funding from additional sources which allowed the investigation of related questions on the operation of the counterflow reactor. Specifically, lean premixed combustion of methane, propane and heptane was studied in the counterflow reactor. This reactor design was previously used to study the conversion of rich methane, propane and heptane reactant mixtures to hydrogen-rich synthesis gas. The current study expanded the established capability of the counterflow reactor to operate in the lean combustion regime on increasingly complex fuels. In particular, liquid fuels are generally easier and safer to transport than gaseous fuels, and are studied because of their logistical importance.

Results included reactor stability maps for methane, propane and heptane combustion that show stable operating points, as well as points where operation became unstable due to flashback, blow-off or extinction, for rich and lean reactant mixtures. Emissions of CO, NO<sub>x</sub> and UHC were presented for lean methane, propane and heptane operation. Additionally, operating regions were defined in terms of peak reactor wall temperatures. Similarities in trends between the three tested fuels highlight the correlation of emissions with peak reactor wall temperature, and support previous findings that a minimum firing rate is necessary for optimal performance.

Further analysis highlights the importance of achieving peak wall temperatures near, or in excess of, the calculated adiabatic equilibrium temperature of the fuel at inlet conditions in heat-recirculating reactors for emissions minimization and stable range extension.

Further details of counterflow reactor operation at lean conditions are presented in Appendix D.

## **2.5 Effect of preheat on premixed methane/air flames**

In the filtration reactor the analysis of the conversion of a fuel to syngas is complicated by the presence of the porous material. In order to better understand the effect of preheat on conversion an experimental and modeling study of burner-stabilized flames was conducted. First experiments were conducted with unheated reactants so that confidence in the models could be gained for their prediction of combustion characteristics, especially species yields, at high equivalence ratios. The effect of preheat was investigated by preheating reactants up to 630 K while holding the inlet velocity and equivalence ratio constant.

The results showed that the burner stabilized flame model accurately predicts standoff distance, limit conditions and species yields for experiments with flat flame burners. Experiments with preheated reactants demonstrated that the operating limits for a flat flame burner increase substantially with increased reactant temperature, allowing the stable operation of the burner at richer equivalence ratios—where syngas yields are greater—than those achievable with unheated reactants. The specific effect of inlet temperature was investigated, and it was found that inlet temperature did not affect the yield of syngas under the tested range of temperatures. Burner-stabilized flames with preheated reactants showed deviations from equilibrium results in terms of species yields, in contrast with unheated conditions where equilibrium predicts species yields for burner-stabilized flames very well. The burner-stabilized flame model was able to predict the deviation from equilibrium when reactants were preheated to ~630 K. At high preheat temperatures, the limiting operating conditions of the experiment were well-predicted by the burner-stabilized flame model but not by the laminar flame speed.

These results have important implications with regards to heat recirculating reactors. First, the models, and therefore the kinetics mechanism, performed very well up to richest equivalence ratio examined of 1.75, which exceeds the conventional rich flammability limit. The only significant difference between the models and the experiments was the difference between the limit equivalence ratio and the equivalence ratio where the laminar flame speed was 25 cm/s when the reactants were preheated to 617 K. This means that those working on reactor models for rich combustion should have confidence in GRI3.0 for predicting syngas production even beyond the rich flammability limit. In heat-recirculating reactors, preheat is accomplished by transport enhancement, which occurs in proximity to the reaction zone, as part of the reactor design. In the experiments described here, the preheat occurred far upstream of the reaction zone and was input from an external source. This experimental design provided a means to study the

effect of preheat temperature independent of enhanced transport mechanisms and interaction with the reaction zone. The results show that preheat is necessary to attain stable operation at extreme equivalence ratios. This was the expected result since conditions (such as downstream propagation of the reaction zone in a filtration reactor) that enhance preheat have been observed in heat-recirculating reactors when mixtures expected to be unstable are burned. It was also found that further preheat does not enhance syngas production. This result aids in the design of heat recirculating reactors because it indicates that maximal heat recirculation may not be necessary for conversion of fuel to syngas.

Further details of the study of the effect of preheat on premixed methane/air flames are presented in Appendix E.

### 3 Bibliography

- Bingue, J.P., A. V. Saveliev, A. A. Fridman, and L. A. Kennedy, "Hydrogen Production in Ultra-rich Filtration Combustion of Methane and Hydrogen Sulfide", *Int. J. Hydrogen Energy* 27 (2002) 643–649.
- Dhamrat, R. and J. L. Ellzey, "Numerical and Experimental Study of the Conversion of Methane to Hydrogen in a Porous Media Reactor", *Combust. Flame* 144 (2006) 698–709.
- Dixon, M.J., I. Schoegl, C. B. Hull, and J. L. Ellzey, "Experimental and Numerical Conversion of Liquid Heptane to Syngas through Combustion in Porous Media", *Combust. Flame* 154 (2008) 217–231.
- Dunn-Rankin, D., E.M. Leal, and D.C. Walther, "Personal Power Systems", *Prog. Energy Comb. Sci.*, 31, (2005) 422-465.
- Fay, M., R. Dhamrat, and J. L. Ellzey, "Effect of Porous Reactor Design on Conversion of Methane to Hydrogen", *Combust. Sci. Tech.* 177 (11) (2005) 2171–2189.
- Hackert, C.L., J.L. Ellzey, and O.A. Ezekoye, "Combustion and Heat Transfer in Model Two-Dimensional Porous Burners", *Combust. Flame* 116 (1999) 177-191.
- Hackert, C.L., J.L. Ellzey, and O.A. Ezekoye, "Effects of Thermal Boundary Conditions on Flame Shape and Quenching in Ducts", *Combust. Flame* 112 (1998) 73-84.
- Henneke, M.R., J.L. Ellzey, "Modeling of Combustion in a Packed Bed", *Combust. Flame* 117 (1999) 832-840.
- Iyoha, O., R. Enick, R. Killmeyer, B. Howard, B. Morreale, and M. Ciocco, "Wall-catalyzed Water-gas Shift Reaction in Multi-tubular Pd and 80 wt%Pd-20 wt%Cu Membrane Reactors at 1173 K", *J. Membrane Sci.* 298 (2007) 14–23.
- Kee, R.J., H. Zhu, and D. G. Goodwin, "Solid-oxide Fuel Cells with Hydrocarbon Fuels", *Proc. Combust. Inst.* 30 (2005) 2379–2404.
- Kee, R.J., J.F. Grcar, M.D. Smooke, and J.A. Miller, "A Fortran Program for Modeling Steady, One-Dimensional Premixed Flames", Sandia National Laboratories (1985).

- Kennedy, L.A., A.V. Saveliev, J.P. Bingue, A.A. Fridman, and S.I. Foutko, "Filtration Combustion of a Methane Wave in Air for Oxygen-rich and Oxygen-depleted Environments", *Proc. Combust. Inst.* 28 (2000) 1431-1438.
- Lin, H., E. V. Wagner, B. D. Freeman, L. G. Toy, and R. P. Gupta, "Plasticization-enhanced Hydrogen Purification Using Polymeric Membranes", *Science* 311 (2006) 639–642.
- Moon, D.J., J. W. Ryu, S. D. Lee, B. G. Lee, and B. S. Ahn, "Ni-based Catalyst for Partial Oxidation Reforming of Iso-octane", *Applied Catalysis A: General* 272 (2004) 53–60.
- National Research Council, *Technology Development for Army Unmanned Ground Vehicles* (2002), <http://www.nap.edu/catalog/10592.html> (accessed June 2008).
- Pedersen-Mjaanes, H., L. Chan, and E. Mastorakos, "Hydrogen Production from Rich Combustion in Porous Media", *Int. J. Hydrogen Energy* 30 (2005) 579-592.
- Pons, J.L., *Wearable Robots: Biomechatronic Exoskeletons*, Wiley (2008).
- Schoegl, I. and J. L. Ellzey, "A Mesoscale Fuel Reformer to Produce Syngas in Portable Power Systems", *Proc. Combust. Inst.* 32 (2009) doi:10.1016/j.proci.2008.06.079.
- Schoegl, I. and J. L. Ellzey, "Superadiabatic Combustion in Conducting Tubes and Heat Exchangers of Finite Length", *Combust. Flame* 151 (2007) 142–159.
- Schoegl, I., S. R. Newcomb and J. L. Ellzey, "Ultra-Rich Combustion in Parallel Channels to Produce Syngas from Propane", (2008) *in preparation*.
- Smith, C.H., D.M. Leahey, L.E. Miller, J.L. Ellzey, and M.E. Webber, "Conversion of Wet Ethanol to Syngas and Hydrogen", *Proc. ES2008* (2008) accepted.
- Stevinson, B.Y., D.L. Bourell, and J.J. Beaman, Jr., "Freeform Fabrication of Non-Metallic Objects by Selective Laser Sintering and Infiltration", *Materials Science Forum*, 561-565 (2007), 817-820.
- Turbine Fuels, Aviation, Kerosene Types: NATO F-34 (JP-8), NATO F-35 and JP-8+100, Military Specification MIL-DTL-83133F* (April 2008).
- Wheeler, C., A. Jhalani, E.J. Klein, S. Tummala, and L.D. Schmidt, "The Water-gas Shift Reaction at Short Contact Times", *Journal of Catalysis* 223 (2004) 191–199.

## Appendix A: Non-catalytic reforming of butanol and Jet-A

The first objective of this ARO-funded project was to demonstrate that Jet-A and butanol could be converted to syngas through non-catalytic means. This work is described below and was published in *C.H. Smith, D.I. Pineda, C.D. Zak, and J.L. Ellzey, J. Hydrogen Energy 38 (2013) 879-889*.

In a filtration reactor, which was used in this study, a reaction zone may propagate upstream or downstream relative to the porous solid at relatively low speed (~1-10 cm/min). This type of reactor differs substantially from other types of porous media and heat recirculating reactors in which the front is stabilized because there are no theoretical flammability limits in filtration reactors [13]. Filtration reactors and other types of heat recirculating reactors have been used to convert various hydrocarbons to syngas, particularly gaseous hydrocarbons [14-21]. Conversion to syngas has been successfully accomplished with liquid fuels including ethanol [22] and heptane [23] in a filtration reactor. In other types of heat-recirculating reactors, diesel [11, 24], octane [25], heptane [26] and kerosene (jet fuel) [27] have been converted to syngas.

Both butanol and jet fuel have been studied extensively at moderate equivalence ratios ( $\phi$ ). Studies on butanol include basic investigations on flames [28], kinetic modeling [29, 30], combustion in engines [31], and catalytic combustion [32]. At rich conditions where the interest is on the production of syngas, butanol research has focused on equilibrium thermodynamic analysis [33-36], and conversion by catalytic methods [37-39].

At moderate  $\phi$ , there has been significant work on jet fuel and other high molecular weight fuels over the last two decades. Fundamental work on diffusion flames [40, 41] and kinetic modeling [42, 43] has significantly advanced our understanding of these complex fuels, as has work on cracking [44] and fuel stability [45]. Equilibrium analyses and computational studies [46] have shown the potential for syngas production from jet fuel using various methods including catalysts [4, 47-54] and plasmas [55]. Investigations of noncatalytic reforming in porous media have generally focused on reactors with stationary reaction zones [25, 27].

Soot formation is often a consideration when using these high molecular weight fuels, and their propensity to soot has been studied in various experimental configurations including diffusion flames [42, 56, 57], pool fires [58, 59], and engine conditions [60-62]. Soot production in premixed flames has also been investigated at moderately rich  $\phi$  [63, 64], though, as noted in the literature [65], very high equivalence ratios are difficult to study because of flame instability. In filtration combustion soot production from heptane [23] has been investigated. In other porous media reactors soot production from iso-octane and petrol [25] was investigated for  $\phi$  up to 4.25 and heptane, diesel oil, kerosene (jet fuel) and bio-diesel [27] for  $\phi$  up to 3.

As a demonstration and initial investigation of the principle of noncatalytic conversion of jet fuel and butanol to syngas by transient filtration combustion, we performed experiments over a range of rich equivalence ratios and inlet velocities (cold gas). Both fuels are compared for syngas production potential and soot production, and a comparison to other fuels is performed based on data found in the literature.

### **A.1 Principle of Operation of Filtration Reactors**

In filtration combustion, a gaseous mixture flows through a porous solid and a reaction front is established within the pores. The fuel may be either the solid or the gas, and in the case presented here, the solid is inert and the combustible gas mixture flows through the porous matrix. Heat is transferred upstream from the hot products to the reactants through the porous solid by conduction and radiation. Depending on the operating conditions, the reaction front may propagate upstream or downstream relative to the solid. This propagation speed is typically much less than the inlet velocity ( $V$ ) of the fuel/air mixture and is dependent upon the properties of the solid, the properties of the fuel and the operating conditions [66].

When the front is propagating upstream, it is moving into a relatively cool solid resulting in subadiabatic temperatures, i.e, temperatures lower than those predicted by equilibrium. Conversely, when the front is propagating downstream it is moving into a preheated solid, resulting in additional heat gain to the reactants and local superadiabatic temperatures, which are above those predicted by equilibrium. Figure A.1, which is a computational model solution for ethanol/air [67], describes these phenomena by showing the gas temperature as a function of axial position for four different times. The equilibrium temperature is  $\sim 1700$  K, and the superadiabatic temperature spikes can be clearly seen in each curve. The figure also shows that the preheat region expands as the front propagates downstream.

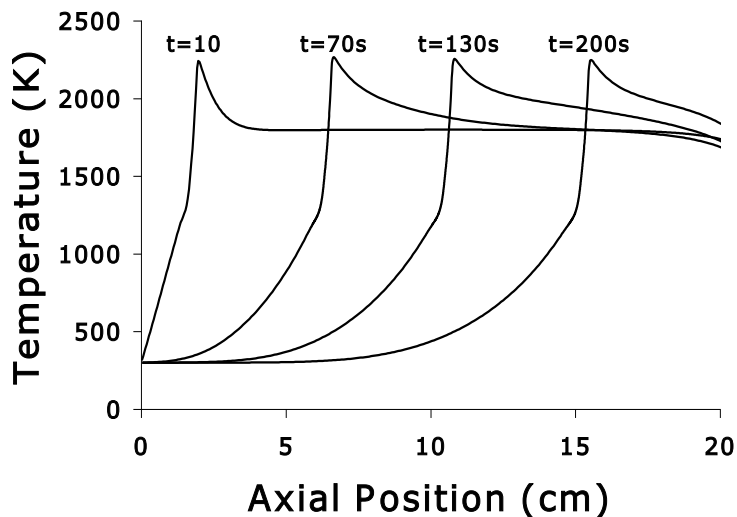


**Figure A.1. Representative temperature vs. axial position for a reaction zone propagating downstream in a filtration reactor [67]**

The strongly superadiabatic temperatures created in filtration reactors make possible the combustion of mixtures far outside the conventional flammability limits [68]. Theoretical analysis predicted no flammability limit for filtration combustion [13], and experimental observations have confirmed that self-sustaining combustion is achieved at both very rich and very lean conditions [69]. Under conditions when the reaction zone propagates upstream or downstream, the reactor cannot be run continuously because the reaction zone eventually either blows off or flashes back. This has prompted the design and development of reactors with stationary reaction zones [9, 70]. In contrast to reactors with propagating reaction zones, reactors with stationary reaction zones have narrower operating ranges, only producing peak temperatures that are slightly superadiabatic. Another design, called a reciprocal flow burner, retains the advantage of strongly superadiabatic temperatures but can be run continuously because the reaction zone is constrained to a fixed volume in a porous medium by reversing the flow of the reactants periodically. Filtration combustion has been the topic of multiple review papers [11, 71-73], and the detailed principles of operation can be found in the literature [66, 74, 75].

## **A.2 Experimental Method**

### **Experimental Apparatus**

The experimental apparatus (Figure ) consists of the reactor, the fuel vaporization system, the reactant delivery system, and the data acquisition system. A quartz cylinder 5 cm in diameter and 30 cm in length includes both the reactor and vaporization chamber. The reactor section of the quartz cylinder is filled with 99.5% pure alumina (AL<sub>2</sub>O<sub>3</sub>) spheres of 5 mm in diameter (Union Process) and insulated on the outside with 2 cm thick alumina. The alumina insulation has holes

every 2 cm along the length to allow visual observation of the reaction zone location and soot deposition.

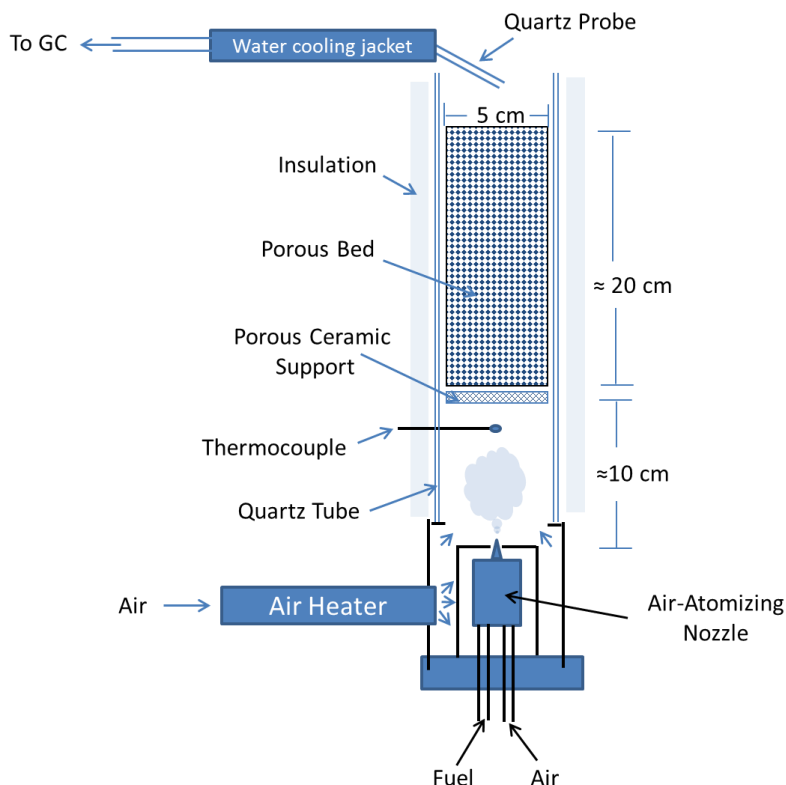


**Figure A.2: Diagram of experimental apparatus**

The vaporization system consists of an air-atomizing nozzle and the quartz chamber for mixing. The atomized fuel droplets, approximately 20 microns in size, are vaporized in a separate heated air stream in the quartz chamber. The base of the chamber, which holds the nozzle and air heater, is machined and welded stainless steel. The outer surface of the quartz chamber is wrapped with resistance band heaters and insulation to prevent condensation of the fuel. Portions of the band heaters and insulation are removable so that any potential condensation of the jet fuel can be observed. Some operating conditions were not tested (high  $V$  with high  $\phi$ ) because the vaporization system was unable to produce a gaseous stream of reactants. Data are reported under conditions when accumulation of liquid fuel was not observed, and when the reactant stream was always transparent (ie: no observable droplets of liquid fuel) before entry into the porous media. The temperature of the inlet mixture was always between 150°C and 200°C as measured by the thermocouple placed before entry to the reactor.

The fuel delivery system includes a fuel tank, a pump and rotameters for fuel regulation. The stream of dry laboratory air entering the nozzle was unheated, but an inline air heater heated the

other stream of air. The air entering the nozzle and the air entering the inline air heater were controlled with separate mass flow controllers.

For these experiments, jet fuel from Berry Aviation at the San Marcos Municipal Airport was used. AVFuel Corporation supplies the fuel to Berry Aviation. Since jet fuel can have a varying composition, an average chemical formula must be assumed. In this work, a chemical formula of  $C_{11}H_{21}$  was used [76]. The density, as measured by a laboratory scale, was  $797 \text{ kg/m}^3$ , and the lower heating value was  $43.2 \text{ MJ/kg}$  as given by [77]. The butanol that was used in this study was obtained from Superior Solvents and Chemicals. The density was measured as  $810 \text{ kg/m}^3$  and the lower heating value was  $33.1 \text{ MJ/kg}$  [77].

### **Experimental Procedure**

When a specific operating condition ( $\phi$ ,  $V$ ) was to be tested, the reaction front was first positioned 5-10 cm from the bottom of the porous medium part of the reactor by igniting a slightly lean flame at the exit of the porous medium and allowing it to propagate upstream. This procedure ensured that any soot that was deposited within the reactor during operation at the previous condition was completely burned off before the start of the next condition to be tested. Then the flows of fuel and air were set to the desired values, and sampling of the exhaust gases by a Varian, Inc. gas chromatograph (GC) began. Each GC sample required 160 seconds, so samples were taken when the reaction zone was at different positions along the length of the reactor if the reaction zone was propagating. The first sample, which was discarded along with the second sample to clear the line between the reactor and the GC, was taken when the reaction zone was between 5 and 10 cm from the bottom of the porous media. The location of the reaction zone was monitored visually through the holes in the insulation surrounding the reactor, and no samples were taken when the reaction zone was less than  $\sim 5$  cm from the exit of the reactor. At least 4 samples and most often 5 were taken for each operating condition, and the data reported in this paper are averages of the last 2 or 3 samples. Given this procedure all reported measurements were taken when the reaction zone was between 10 and 15 cm from the bottom of the reactor.

The GC was calibrated to measure the following species: hydrogen, oxygen, nitrogen, methane, carbon dioxide, carbon monoxide, ethylene, ethane, acetylene and select higher hydrocarbons. The GC sampled the exhaust gas for measurement through a water-cooled quartz probe. Measurement uncertainty was calculated using a Student-t distribution. The contributions to the uncertainty were uncertainty in the GC calibration gases, uncertainty in the GC calibration, and uncertainty in the flow rates of air and fuel. Uncertainties for all calculations were based on sequential perturbation. For calculations of yield and carbon balance, the molar flow rates of species in the exhaust were required. These molar flow rates were calculated by assuming the flow rate of nitrogen into the reactor equaled the flow rate of nitrogen out of the reactor.

For every tested condition, the first two measurements were discarded and the rest of the measurements were averaged.

### A.3 Results and Discussion

In the experiments for each fuel, we obtained one set of data by varying  $\phi$  and holding  $V$  constant and another by varying  $V$  while holding  $\phi$  constant. The experimental operating conditions are described in Table A.1.

Fuel	Equivalence Ratio ( $\phi$ )	Inlet Velocity (V) [cm/s]
Butanol	1-5	30
Butanol	3	30-60
Jet A	1-3.15	34
Jet A	2.7	34-46

**Table A.1: Experimental operating conditions**

The tested ranges for  $\phi$  and  $V$  were determined by multiple factors. For both fuels, maximum  $V$  was limited by the rate of downstream reaction zone propagation. Species data are reported from conditions when the GC could sample the exhaust gases at least 4 times, and this was possible only when the downstream propagation rate was less than  $\sim 2.5$  cm/min. For butanol and jet fuel, the reaction zone remained nearly stationary (the reaction zone remained within 5-10 cm from the bottom of the reactor in the time that 5 samples were taken) relative to the porous media when the operating conditions were  $\phi \approx 2$ ,  $V \approx 32$  so the GC could sample the exhaust gases many times. When  $\phi$  or  $V$  increased from these values, the reaction zone propagated downstream up to  $\sim 3$  cm/min, and the speed of propagation was higher for jet fuel than for butanol under the near-overlapping tested conditions. The  $\sim 2.5$  cm/min limit on the propagation speed determined the limiting  $V$  for both fuels and the limiting  $\phi$  for butanol, however soot formation limited the maximum testable  $\phi$  for jet fuel. The minimum testable  $V$  was determined by the minimum flow rates required for safe operation of the inline air heater.

Important metrics for syngas production are the hydrogen yield and the carbon monoxide yield. These metrics, defined below, describe how effectively the reactor converts hydrogen and carbon bound in the fuel to diatomic hydrogen and carbon monoxide, respectively.

$$\text{hydrogen yield} = 100 \times \frac{2 \times \dot{N}_{H_2}}{N_H \times \dot{N}_{Fuel}} \quad (\text{A.1})$$

$$\text{carbon monoxide yield} = 100 \times \frac{\dot{N}_{CO}}{N_C \times \dot{N}_{Fuel}} \quad (\text{A.2})$$

where the units of  $\dot{N}_{Fuel}$ ,  $\dot{N}_{H_2}$  and  $\dot{N}_{CO}$  are moles per second.  $N_H = 10$  and  $N_C = 4$  for butanol,  $N_H = 21$  and  $N_C = 11$  for jet fuel [76].

We also calculated values for the chemical energy conversion efficiency. This metric describes the percentage of chemical energy in the original fuel that was contained in particular exhaust species. The energy conversion efficiencies were calculated using the LHV of the individual species as described by the following representative equation for hydrogen:

$$\text{hydrogen energy conversion efficiency} = 100 \times \frac{\dot{N}_{H_2} \times LHV_{H_2}}{LHV_{Fuel} \times \dot{N}_{Fuel}} \quad (\text{A.3})$$

where LHV values are in units of kJ per mole.

Similarly, we calculated the total energy conversion efficiency, the percentage of chemical energy in the original fuel contained in all fuel exhaust species. If all species are at ambient temperature and no energy is lost through heat transfer, then this quantity should be 100%. Values lower than 100% indicated how much energy is associated with heat losses and the sensible energy of the products. The total energy conversion efficiency was calculated as follows:

$$\text{total energy conversion efficiency} = 100 \times \frac{\sum_i \dot{N}_i \times LHV_i}{LHV_{Fuel} \times \dot{N}_{Fuel}} \quad (\text{A.4})$$

The summation is performed over all gaseous species in the exhaust with positive LHV and with non-negligible concentration (concentration > 0.1%). LHV values were taken from [78].

For comparison with experimental results, equilibrium values are also presented. We calculated these values for a constant pressure/enthalpy process using the Cantera software suite [79]. In heat-recirculating reactors peak temperatures can significantly exceed the adiabatic flame temperature. However, there is no external energy input so under ideal conditions the products exit at the adiabatic flame temperature; for this reason it is appropriate to compare the experimental results to equilibrium calculations for a constant enthalpy process. Previous work [23, 80] has shown that equilibrium calculations predict trends in exhaust species as a function of reactant composition and can provide insight into the thermodynamic character of the conversion process. All equilibrium calculations included the formation of solid carbon.

## Soot Observations

One of the challenges of investigating butanol and jet fuel at rich conditions was the propensity of these fuels to produce soot. For both fuels, when  $\phi$  was greater than approximately 1.5, soot was observed in the reactor through the holes in the insulation surrounding the reactor and at the exit of the reactor. When the reaction zone propagated downstream soot was observed both upstream and downstream of the reaction zone. The highest  $\phi$  tested with jet fuel was 3.58 because soot laydown at this equivalence ratio and higher was so great that it clogged the pores of the reactor, and the porous media was ejected from the reactor. With butanol the reactor was not clogged at any tested equivalence ratio, although significant soot was observed. The quantities of soot increased, based on qualitative observation, with increasing  $\phi$ .

In order to investigate further the magnitude of soot deposition, a carbon-flow balance was performed from the experimental measurements and equilibrium calculations. Figure A.2 shows this carbon balance in terms of the ratio:

$$\frac{\text{carbon out}}{\text{carbon in}} = \frac{\text{measured flow rate carbon atoms in gaseous exhaust}}{\text{flow rate of carbon atoms in fuel}} \quad (\text{A.5})$$

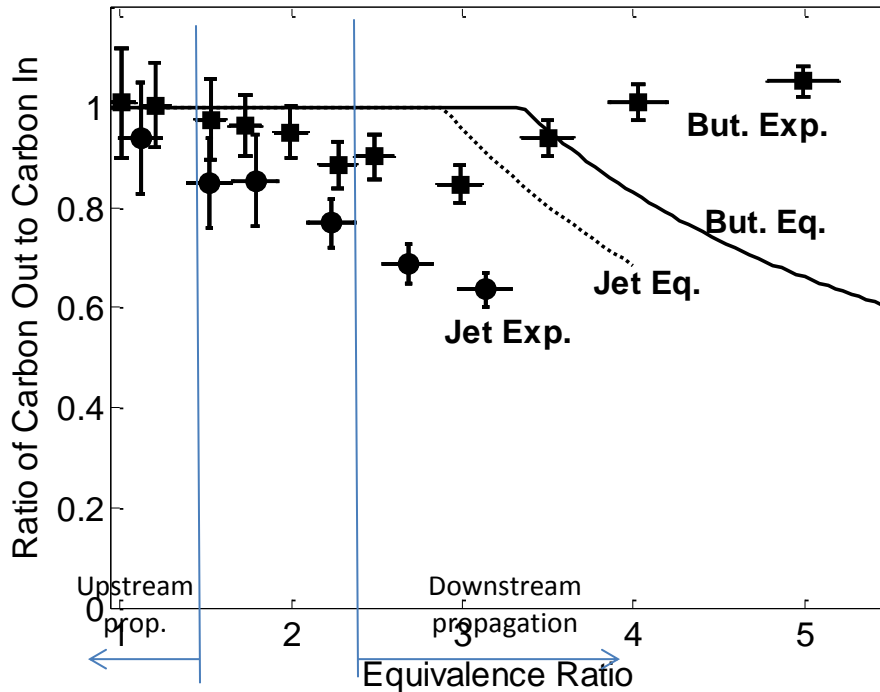


**Figure A.2: Ratio of carbon out to carbon in vs. equivalence ratio with inlet velocity =  $32 \pm 2$  cm/s. Lines on the figure indicate approximate equivalence ratios at which upstream and downstream propagation occurred.**

As shown in the figure, equilibrium predicts that all carbon is in gaseous species until  $\phi \sim 3$ , above which significant solid carbon formation occurs. This carbon formation results in the relatively sharp decreases in CO yield and total energy conversion efficiency seen in Figures A.4, A.5, A.7, A.8, A.10 and A.11. In the experiments near stoichiometric conditions, carbon is in gaseous compounds for both butanol and jet fuel. As  $\phi$  increases, however, the ratio of carbon leaving to carbon entering decreases steadily for jet fuel until the maximum  $\phi$  tested (3.15) is reached. This indicates that carbon is being converted to forms not measured by the GC, including large hydrocarbons, hydrocarbons condensed on the porous media and solid carbon deposited on the porous media. For jet fuel at  $\phi = 3.15$ , about 40% of the carbon entering the system is not measured by the GC. These data are consistent with the qualitative observation of heavy soot deposition and reactor reactor clogging in the experiments with jet fuel. For butanol the ratio decreases until  $\phi = 3$ , and then rises again to exceed 1 at  $\phi = 5$ .

The carbon ratio greater than 1 is counter-intuitive and initially suggests that carbon is being “created.” On closer inspection, however, this is a consequence of the transient nature of filtration combustion. As shown in Figure A.1, when the front propagates downstream three important parameters change with time: the residence time of the gas upstream of the reaction increases, the residence time of the gas downstream of the reaction zone decreases, and the preheat region expands. These effects, coupled with the soot deposition and potential large hydrocarbon condensation complicate the analysis of the experimental results for downstream-propagating reaction zones. As indicated in Figure A.2, the reaction zone propagated downstream when  $\phi$  exceeded 2.5, and this downstream propagation rate increased with equivalence ratio.

Soot is complex, containing a variety of chemical species and structures, including adsorbed hydrocarbons [81]. Since soot is composed mainly of carbon and hydrogen, it, along with adsorbed hydrocarbons, can be oxidized to other species that are measured in the exhaust [64, 82]. One would expect this effect to be particularly pronounced when O<sub>2</sub> is in proximity to surfaces coated with soot at high temperature, and this occurs significantly when the reaction zone propagates downstream as soot was observed upstream of the reaction zone. Soot particles can grow on timescales similar to the residence times in the reactor [83, 84]. Therefore an additional effect of downstream propagation is that hydrocarbon species, particularly acetylene, that contribute to soot growth have less time to do so because their residence time between the reaction zone and the sampling point decreases with downstream propagation. The carbon balance exceeding 1 at the highest  $\phi$  is suspected to be the result of the soot consumption/oxidation rate exceeding the soot deposition rate at the time those samples were taken.

The data that were taken when the reaction zone was nearly stationary ( $\phi \sim 2$ ) or upstream propagating ( $\phi < 1.5$ ) are considered as appropriate representations of the conversion potential of

these fuels. In these cases, soot is not observed upstream of the reaction zone, and therefore there is no potential for additional fuel species to be added to the gaseous stream. Results in the following sections are presented in terms of yield and energy conversion efficiency, which are defined relative to the known fuel input at the time of sample. The data shown in Figure A.2 imply that the yields and energy conversion efficiencies must be interpreted with the carbon flow balance in mind. If there is a net deposition of soot at the time a given sample is taken, this will be reflected in lower yields and energy conversion efficiencies. If the rate of oxidation/consumption exceeds the deposition rate at the time a sample is taken the yields and energy conversion efficiencies will be artificially high.

Not only do the results shown in Figure A.2 and our qualitative observation of soot (including complete pore blockage in the jet fuel experiments) have implications for the work presented here, but these data also have important implications for any experimental work with butanol and jet fuel at high  $\phi$  in premixed combustion. Burning the soot out of the reactor at all conditions was accomplished by burning a lean mixture that propagated upstream through the reactor. For a filtration reactor to be operated in any practical application this procedure would be required. In addition, such a cleaning procedure would likely be required for other reactors that operate with these fuels at  $\phi$  greater than about 2.

### Conversion of Jet Fuel

Ideal fuel conversion results in the complete conversion of carbon and hydrogen in the reactants to CO and H<sub>2</sub> in the products, respectively. The yields of these species, then, describe reactor performance relative to the ideal case. The effect of  $\phi$  on syngas production in terms of H<sub>2</sub> and CO yields is shown in Figure A.3.

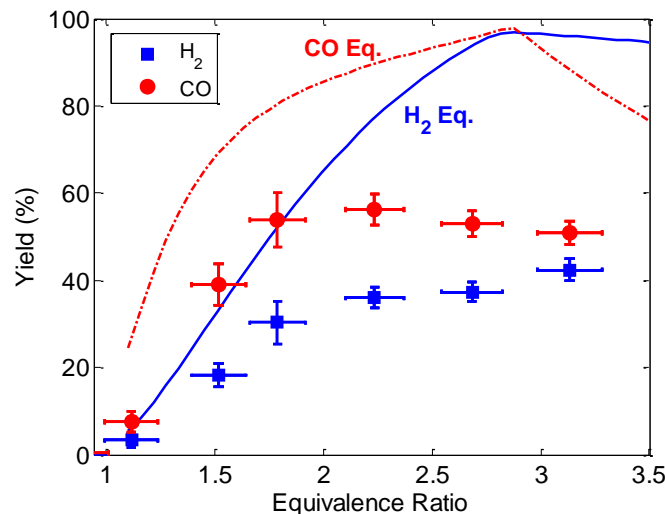


**Figure A.3: Yield vs. equivalence ratio for jet fuel with inlet velocity = 34 cm/s.  
Downstream propagation observed for equivalence ratio > 2.5**

The yields for CO and H<sub>2</sub> are zero at stoichiometric, and very small for  $\phi = 1.25$ . At higher  $\phi$  the equilibrium values are all higher than the corresponding experimental measurements. The CO yield increases rapidly with  $\phi$  until  $\phi = 2.25$  while the H<sub>2</sub> yield continues to increase over the entire tested range. The maximum yields for H<sub>2</sub> and CO occur at different  $\phi$  and are 42% at  $\phi = 3.15$  and 56% at  $\phi = 2.25$ , respectively. In contrast, equilibrium calculations predict that the peaks in conversion of H<sub>2</sub> and CO occur at the same  $\phi$  ( $\phi \sim 2.9$ ).

As mentioned previously, the energy conversion efficiency is the percentage of chemical energy in the fuel that is contained in specific species in the exhaust. The total energy conversion efficiency is the percent of the chemical energy in the fuel that is contained in the exhaust. Figure A.4 and

Figure A.5 show the total energy conversion efficiency and species energy conversion efficiency as a function of  $\phi$  and V for jet fuel.

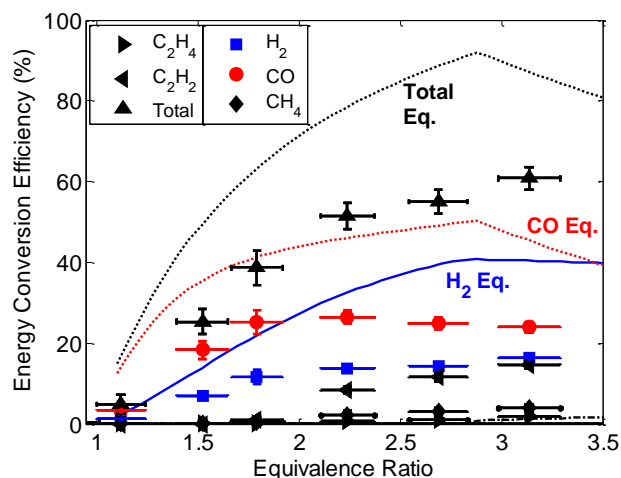


**Figure A.4: Energy conversion efficiency vs. equivalence ratio for jet fuel with inlet velocity = 34 cm/s. Downstream propagation observed for equivalence ratio > 2.5**

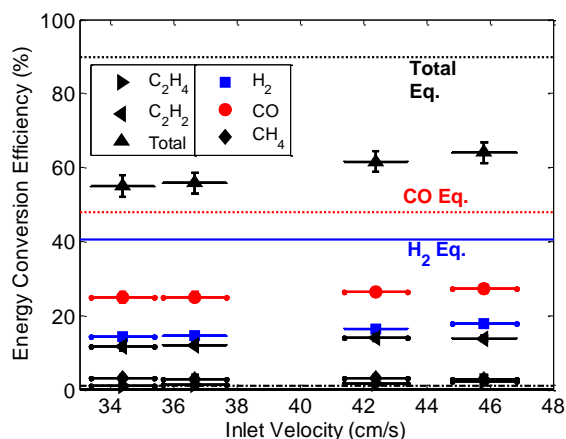


**Figure A.5: Energy conversion efficiency vs. inlet velocity for jet fuel with equivalence ratio = 2.7. Downstream propagation observed for all conditions**

Similar to the trend observed in Figure A.3, the experimental energy conversion efficiencies for CO, H<sub>2</sub> and the total are significantly lower than equilibrium (Figure A.4). The total energy conversion efficiency increases with  $\phi$  up to a maximum of 61% at  $\phi = 3.15$ , meaning that 39% of the energy in the original fuel is lost to heat. Besides H<sub>2</sub> and CO, acetylene, and to a lesser degree methane, are the only energy-containing species that contributes substantially to the total energy conversion efficiency. This is in contrast to equilibrium which predicts almost no hydrocarbons in the products.

Figure A.5 shows equilibrium and experimental energy conversion efficiency as a function of V for  $\phi = 2.7$ . The experimental data show that V does not affect the energy conversion efficiencies (species specific or total) to a large degree over the tested range. Previous studies have shown that the energy conversion efficiency can depend strongly on inlet velocity; however, the tested range in this study was not as large as the tested ranges reported in previous studies.

### Conversion of Butanol

The potential of butanol for conversion to syngas was investigated through a similar set of experiments to those performed with jet fuel. Butanol differs substantially from jet fuel because it has a smaller molecular weight and is an alcohol, containing an oxygen atom in the molecule. In Figure A.6, the yields of H<sub>2</sub> and CO are presented as a function of  $\phi$  with V held constant at 30 cm/s.

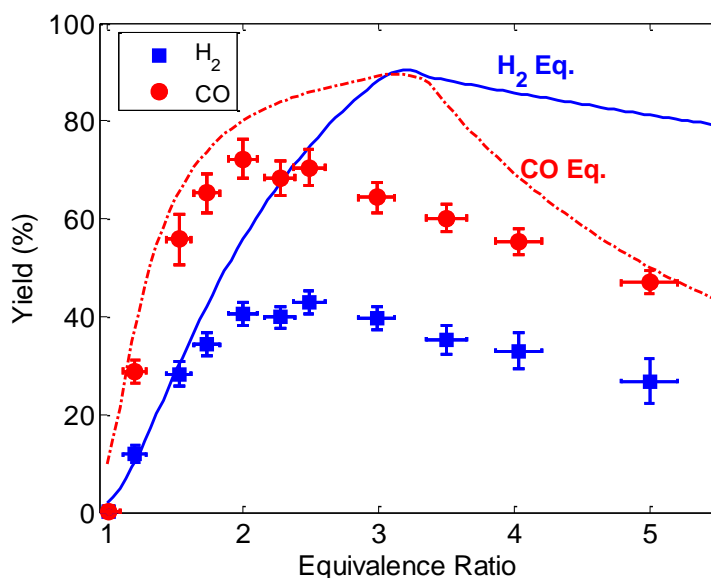


**Figure A.6: Hydrogen and carbon monoxide vs. equivalence ratio for butanol with inlet velocity = 30 cm/s. Downstream propagation observed for equivalence ratio > 2.5**

The yields for H<sub>2</sub> and CO increase rapidly as  $\phi$  is increased from stoichiometric. The peak CO yield (72 %) occurs at  $\phi = 2$ , and the peak H<sub>2</sub> yield (43 %) occurs at  $\phi = 2.5$ . As  $\phi$  increases from these values, the yields for CO and H<sub>2</sub> decrease slowly. For both CO and H<sub>2</sub>, the yields are very similar to the yields predicted by equilibrium until  $\phi \approx 2$ . At higher  $\phi$ , the equilibrium yields are higher than the experimentally measured yields, though at  $\phi = 5$ , the experimental value and equilibrium values for CO yield are nearly identical.

Figure A.7 and Figure A.8 shows the energy conversion efficiency for the measured species and the total energy conversion efficiency as a function of  $\phi$  and V, respectively. Both experimental data and equilibrium results are shown. In Figure A.7 the total energy conversion efficiency determined experimentally follows the equilibrium value until  $\phi > 3$  (where relatively fast downstream propagation was observed). As  $\phi$  increases beyond 3, the experimental value for the total energy conversion efficiency increases until it slightly exceeds 100%. As explained above, it is suspected that an imbalance in soot deposition and consumption at the time of exhaust gas sampling is the reason for the unrealistically high energy conversion efficiencies observed at  $\phi > 3.5$ .

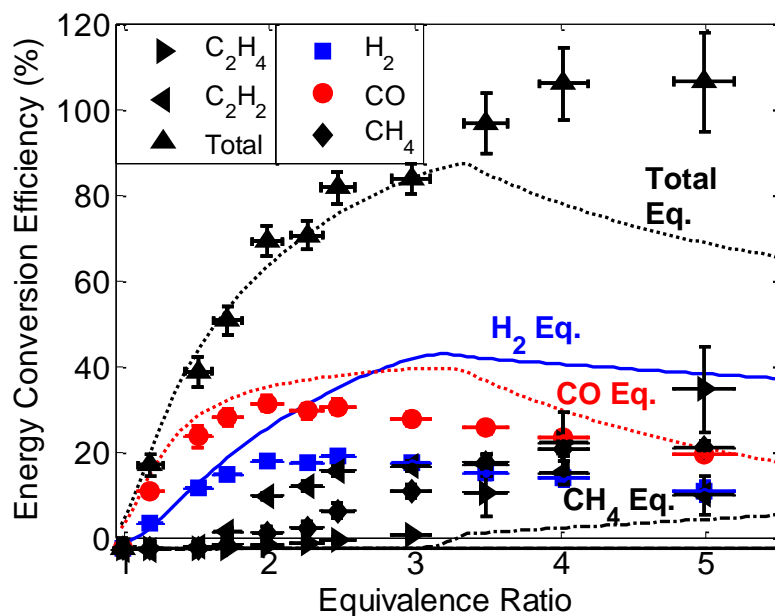


**Figure A.7: Energy conversion efficiency vs. equivalence ratio for butanol with inlet velocity = 30 cm/s. Downstream propagation observed for equivalence ratio > 2**

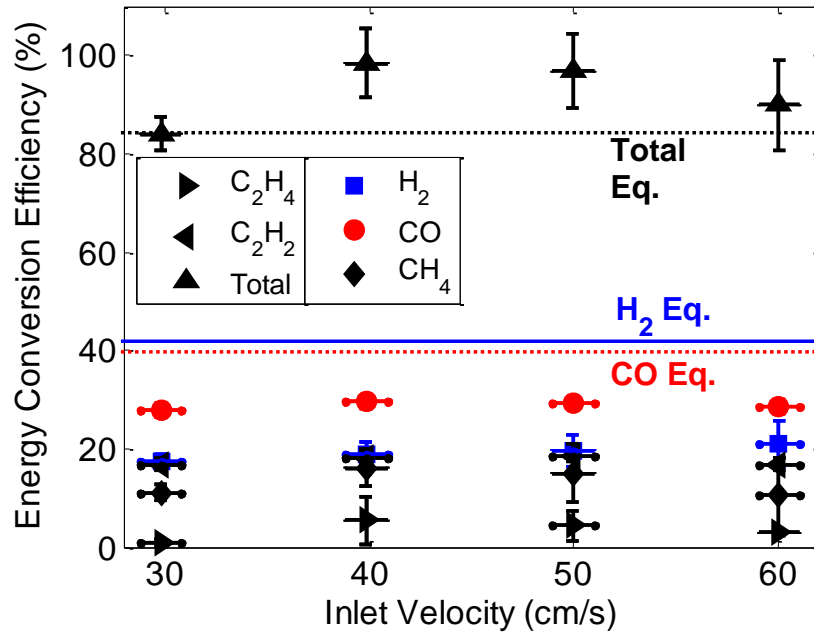


**Figure A.8: Energy conversion efficiency vs. inlet velocity for butanol with equivalence ratio = 3, with downstream flame front propagation observed for all conditions**

For conversion of butanol to H<sub>2</sub> and CO, lower  $\phi$  are optimal since the conversion of energy from butanol to H<sub>2</sub> and CO peaks at  $\phi \approx 2$ . At  $\phi \approx 2$ , a significant amount (10%) of the chemical energy is in acetylene, and the contribution of acetylene to the chemical energy outflow increases to a maximum of 20% at  $\phi = 3.25$  and then decreases as  $\phi$  increases. Methane and ethylene also contributed significantly to the chemical energy outflow as  $\phi$  exceeded 2. The energy in methane peaks at  $\phi = 4$  with a maximum of 23%, while the energy in ethylene is nonzero at  $\phi = 3$  and rises steadily with  $\phi$  up to a maximum of 36% at  $\phi = 5$ . These results contrast with those for jet fuel (Fig. A.5) which shows significantly less contribution from hydrocarbons to the energy content of the exhaust.

Figure A.8 shows the energy conversion efficiencies as a function of  $V$  for butanol with  $\phi = 3$ . Similar to the results for jet fuel, the energy conversion efficiencies for H<sub>2</sub> and CO do not change significantly as  $V$  is increased, but the total energy conversion efficiency does increase somewhat as  $V$  exceeds 30 cm/s. Exceeding the equilibrium value for total energy conversion efficiency and having near 100% conversion when the  $V$  was 40 cm/s and 50 cm/s is, again, likely the result of soot deposition/consumption imbalance and reaction zone propagation (discussed below).

## Fuels Comparison

Thermodynamic analysis is often used to investigate fuel conversion to syngas [34, 70, 85]. In order to provide insight into the relative syngas production efficiencies of a variety of fuels, equilibrium calculations were completed for a set of seven fuels with a range of molecular weights. The computed hydrogen yield and carbon monoxide yield as a function of  $\phi$  for these fuels is shown in Figure A.9 and Figure A.10, respectively.

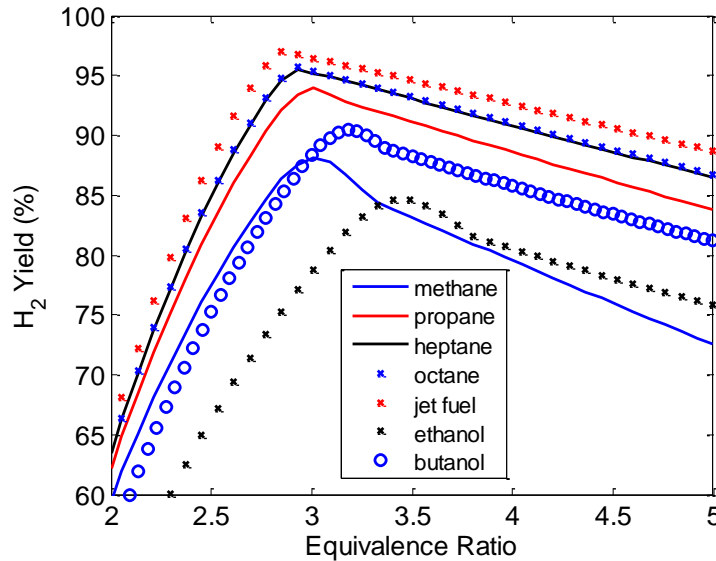


**Figure A.9: Hydrogen yield vs. equivalence ratio (equilibrium values)**

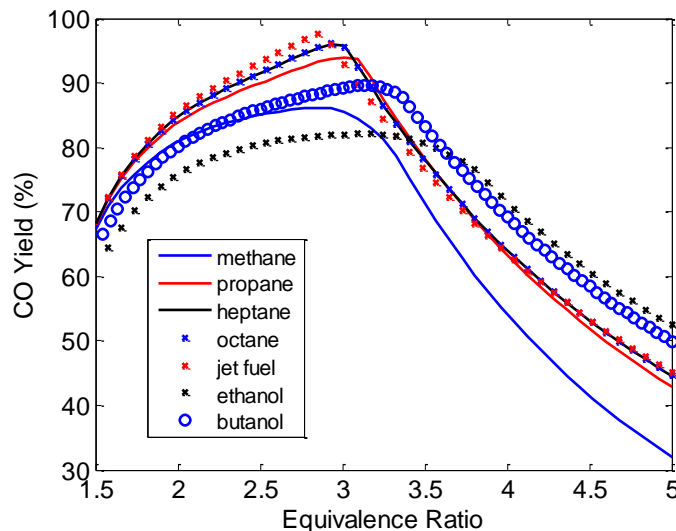


**Figure A.10: Carbon monoxide yield vs. equivalence ratio (equilibrium values)**

The equilibrium data show a trend of increasing H<sub>2</sub> yield with increasing fuel molecular weight. The trend is the same for CO yield excluding the behavior of the oxygenated fuels at  $\phi > 3$ .

Based on equilibrium, jet fuel is expected to produce the highest yields of H<sub>2</sub> and CO, while ethanol should produce the lowest yields. Amongst the non-oxygenated fuels, methane should produce the lowest yields.

In earlier publications, the authors' group reported results of experiments converting methane [86], heptane [23], and ethanol [22] to syngas by filtration combustion. The filtration reactors that were used in these studies were similar to that used in the current study, except that for methane where the reactor consisted of ceramic foam rather than a bed of alumina spheres. For each fuel, the operating conditions were different, so direct comparison across a range of  $V$  and  $\phi$  is not possible. However, there are  $\phi$ ,  $V$  pairs that overlapped or near-overlapped between each of the fuels studied, so a limited comparison can be made amongst the fuels in terms of hydrogen and carbon monoxide yields. These data can be used to determine the accuracy of using equilibrium data to predict relative fuel performance. The hydrogen and carbon monoxide yields for given  $\phi$ ,  $V$  pairs are listed in Table A.2.

Eq. Ratio	Vel (cm/s)	Meth H2 %	Eth H2 %	But H2 %	Hept H2 %	Jet H2 %	Eth CO %	But CO %	Hept CO %	Jet CO %
2.5	55	73			65					
2	55	68	57							
3	55	73		45				66		
2.5	32±2	63		43	55	37		71	72	54
2	60		56		55		82		81	
3	60			47	77			66	85	
2	32±2		45	41		33	75	72		55
3	32±2			40		41		64		52

**Table A.2: Comparison of hydrogen and carbon monoxide yields for various fuels (Representative uncertainty in yield values: ±5%, representative uncertainty in equivalence ratio: 0.1, representative uncertainty in inlet velocity: ±2 cm/s. Data for ethanol from [22], data for methane from [86], and data for heptane from [23])**

CO yield was not reported in the experiments with methane. However, H<sub>2</sub> yield can be compared with the various fuels. As the tables show, the H<sub>2</sub> yield for methane exceeded the H<sub>2</sub> yield that was observed with each of the other fuels. In terms of H<sub>2</sub> and CO yield, ethanol is next best, having a slightly higher yield of both H<sub>2</sub> and CO than butanol and heptane under the same operating conditions. Heptane has the next highest conversion with yields higher than butanol. Jet fuel is, by far, the least efficient producer of syngas with both H<sub>2</sub> and CO yields less than those of all the other fuels except for the H<sub>2</sub> yield compared with butanol. Ten binary comparisons can be made amongst the fuels in terms of H<sub>2</sub> yield, and six can be made in terms of CO yield with these data. Among the ten H<sub>2</sub> yield comparisons and six CO yield comparisons

only in two cases does a fuel with a larger molecular weight have a greater hydrogen yield than one with lower molecular weight (heptane vs butanol for both H<sub>2</sub> and CO). These data, then, suggest that syngas production efficiency generally decreases with molecular weight. Interestingly, this is the opposite of what is predicted by thermodynamic equilibrium (Figure A.9 and Figure A.10).

Experimental investigations of conversion of rich hydrocarbon mixtures have been conducted by other groups in the last few years, and these data allow a further comparison of the relative potential of fuels to be converted to syngas. Pedersen-Mjaanes, Chan, and Mastorakos [87] investigated the conversion of methanol, methane, octane and petrol to syngas in a 2-section heat recirculating reactor. They found methanol to have the highest maximum yield followed by methane and then octane and petrol [87]. Pastore and Mastorakos performed experiments with heptane and diesel in a 2-section reactor [24], and, in contrast to the trends observed in the work of the authors' group, they reported diesel to have a significantly higher rate of conversion than heptane in terms of the conversion of energy in fuel to energy in both H<sub>2</sub> and CO. Kennedy and coworkers at the University of Illinois at Chicago performed experiments with methane, ethane, and propane in a filtration reactor very similar to the one used in the present experiments [16]. Their experiments showed nearly identical CO yields for each of the three fuels, but maximum H<sub>2</sub> yields increased in order of decreasing molecular weight. In a recent paper, the relative conversion efficiencies for experiments with methane, propane and heptane in a counterflow reactor were compared [26]. In those experiments, propane had the highest efficiency of conversion to H<sub>2</sub>, followed by methane and then heptane. With these data from the literature ten binary comparisons can be made in terms of H<sub>2</sub> and CO yield. Of these ten comparisons, three are in agreement with equilibrium prediction (yield increase with molecular weight), five suggest that yield decreases with molecular weight, and two support neither trend. As with the filtration combustion experiments, these data suggest that the trend in syngas production efficiency as a function of fuel size is not predicted by equilibrium.

Based on the data reported in all of these studies, including the present study, the potential of fuels to be converted to syngas roughly decreases with increasing molecular weight. Currently, the available literature does not provide enough data to draw strong conclusions about fuel optimization for conversion to syngas, and there are multiple exceptions to this general trend indicating that there is a need for a comprehensive study of the effect of fuel on conversion where fuels are tested under identical conditions. The major conclusion of this fuels comparison is that equilibrium predictions of syngas production as a function of fuel size are inaccurate under most conditions. Since equilibrium is often used to predict general trends in syngas production, these data suggest that care must be taken when interpreting the results of equilibrium computations.

## A.4 Conclusions

Results of the conversion of butanol and jet fuel to syngas via non-catalytic transient filtration combustion are presented. At maximum, about 42% of the hydrogen in jet fuel was converted to H<sub>2</sub> and 56% of carbon was converted to CO. The H<sub>2</sub> yield continued to increase with  $\phi$  in the jet fuel experiments whereas in the butanol experiments the yields for H<sub>2</sub> and CO both reached peaks within the tested operating range. The peak CO yield for experiments with butanol was 72% and the peak H<sub>2</sub> yield was 43%. Most of the chemical energy exiting the reactor was bound in H<sub>2</sub> and CO, but CH<sub>4</sub>, C<sub>2</sub>H<sub>2</sub> and C<sub>2</sub>H<sub>4</sub> were observed in substantial amounts in experiments with both fuels, especially in experiments with butanol at high  $\phi$ . In contrast, equilibrium predicted nearly negligible amounts of energy-containing compounds besides H<sub>2</sub>, CO and solid carbon.

Soot production proved to be substantial in experiments with both fuels, with the qualitative observation of soot from both fuels exceeding the soot production observed in similar experiments with methane, heptane, and ethanol. Soot production limited the maximum testable  $\phi$  for jet fuel experiments to  $\phi = 3.15$  since soot clogged the reactor when  $\phi$  exceeded this value. An analysis of the carbon balance for jet fuel experiments showed that up to 40% of the carbon entering the system was deposited on the porous medium. Similarly for butanol, the carbon balance showed significant loss up to  $\phi \sim 3$ . At the most extreme  $\phi$ , the reaction zone propagates downstream oxidizing some of the soot that has been deposited previously, resulting in an exhaust stream with more carbon atoms than are contained in the inlet fuel at the time of sample.

Equilibrium calculations and experimental results were analyzed to determine trends in fuel conversion efficiency as a function of fuel type. The equilibrium calculations predicted that larger fuel molecules would, generally, produce higher syngas yields, but the experimental results disagreed with this trend. Generally, experimental results show that smaller hydrocarbons produce higher syngas yields with jet fuel having the lowest hydrogen and carbon monoxide yields. The comparison of these equilibrium data with the experimental data available in the literature suggests that kinetic effects are very important in fuel conversion to syngas and equilibrium results should be interpreted carefully when predicting syngas production from the combustion of very rich mixtures of fuel and air. Lastly, the demonstration of the conversion of jet fuel and butanol, along with previous demonstrations with methane, ethanol and heptane show the robustness of the non-catalytic filtration reactor.

## A.5 References

1. Nigam, P.S. and A. Singh, *Production of liquid biofuels from renewable resources*. Progress in Energy and Combustion Science. **37**(1): p. 52-68.
2. Moon, D.J., et al., *Ni-based catalyst for partial oxidation reforming of iso-octane*. Applied Catalysis A: General, 2004. **272**: p. 53-60.

3. Velu, S., et al., *Desulfurization of JP-8 Jet Fuel by Selective Adsorption over a Ni-based Adsorbent for Micro Solid Oxide Fuel Cells*. Energy & Fuels, 2005. **19**(3): p. 1116-1125.
4. Lakhapatri, S.L. and M.A. Abraham, *Analysis of catalyst deactivation during steam reforming of jet fuel on Ni-(PdRh)/ $\gamma$ -Al<sub>2</sub>O<sub>3</sub> catalyst*. Applied Catalysis A: General. **405**(1&2): p. 149-159.
5. Wood, S. and A.T. Harris, *Porous burners for lean-burn applications*. Progress in Energy and Combustion Science, 2008. **34**(5): p. 667-684.
6. Weinberg, F.J., *Combustion Temperatures: The Future?* Nature, 1971. **233**: p. 239.
7. Takeno, T., K. Sato, and K. Hase, *A Theoretical Study on an Excess Enthalpy Flame*. Proc. Combust. Inst., 1981. **18**: p. 465.
8. Ronney, P.D., *Analysis of Non-Adiabatic Heat-Recirculating Combustors*. Combust. Flame, 2003. **135**: p. 421-439.
9. Schoegl, I. and J.L. Ellzey, *Superadiabatic Combustion in Conducting Tubes and Heat Exchangers of Finite Length*. Combust. Flame, 2007. **151**: p. 142-159.
10. Zhdanok, S., L.A. Kennedy, and G. Koester, *Superadiabatic Combustion of Methane Air Mixtures under Filtration in a Packed Bed*. Combust. Flame, 1995. **100**: p. 221-231.
11. Al-Hamamre, Z. and A. Al-Zoubi, *The use of inert porous media based reactors for hydrogen production*. International Journal of Hydrogen Energy. **35**(5): p. 1971-1986.
12. Hardesty, D.R. and F.J. Weinberg, *Burners Producing Large Excess Enthalpies*. Combust. Sci. Tech., 1974. **8**: p. 201-214.
13. Takeno, T. and K. Sato, *An Excess Enthalpy Flame Theory*. Combust. Sci. Tech., 1979. **20**: p. 73-84.
14. Bingue, J.P., A.V. Saveliev, and L.A. Kennedy, *Optimization of hydrogen production by filtration combustion of methane by oxygen enrichment and depletion*. Int. J. Hydrogen Energy, 2004. **29**(13): p. 1365-1370.
15. Bingue, J.P., et al., *Hydrogen production in ultra-rich filtration combustion of methane and hydrogen sulfide*. Int. J. Hydrogen Energy, 2002. **27**: p. 643-649.
16. Toledo, M., et al., *Hydrogen production in ultrarich combustion of hydrocarbon fuels in porous media*. International Journal of Hydrogen Energy, 2009. **34**(4): p. 1818-1827.
17. Drayton, M.K., et al., *Syngas Production Using Superadiabatic Combustion of Ultra-Rich Methane-Air Mixtures*. Proc. Combust. Inst., 1998. **27**: p. 1361-1367.
18. Kennedy, L.A., et al., *Chemical structures of methane-air filtration combustion waves for fuel-lean and fuel-rich conditions*. Proceedings of the Combustion Institute, 2000. **28**(1): p. 1431-1438.
19. Schoegl, I., S.R. Newcomb, and J.L. Ellzey, *Ultra-rich combustion in parallel channels to produce hydrogen-rich syngas from propane*. International Journal of Hydrogen Energy, 2009.
20. Schoegl, I. and J.L. Ellzey, *A mesoscale fuel reformer to produce syngas in portable power systems*. Proceedings of the Combustion Institute, 2009. **32**(2): p. 3223-3230.

21. Al-Hamamre, Z., S. VoÅÿ, and D. Trimis, *Hydrogen production by thermal partial oxidation of hydrocarbon fuels in porous media based reformer*. International Journal of Hydrogen Energy, 2009. **34**(2): p. 827-832.
22. Smith, C.H., et al., *Conversion of wet ethanol to syngas via filtration combustion: An experimental and computational investigation*. Proceedings of the Combustion Institute, 2010. **33**(2): p. 3317-3324.
23. Dixon, M.J., et al., *Experimental and numerical conversion of liquid heptane to syngas through combustion in porous media*. Combustion and Flame, 2008. **154**(1-2): p. 217-231.
24. Pastore, A. and E. Mastorakos, *Rich n-heptane and diesel combustion in porous media*. Experimental Thermal and Fluid Science, 2010. **34**(3): p. 359-365.
25. Pedersen-Mjaanes, H., L. Chan, and E. Mastorakos, *Hydrogen production from rich combustion in porous media*. International Journal of Hydrogen Energy, 2005. **30**(6): p. 579-592.
26. Belmont, E.L., S.M. Solomon, and J.L. Ellzey, *Syngas production from heptane in a non-catalytic counterflow reactor*. Combustion and Flame, 2012. 159: p. 3624-3631.
27. Pastore, A. and E. Mastorakos, *Syngas production from liquid fuels in a non-catalytic porous burner*. Fuel. **90**(1): p. 64-76.
28. Veloo, P.S., et al., *A comparative experimental and computational study of methanol, ethanol, and n-butanol flames*. Combustion and Flame. **157**(10): p. 1989-2004.
29. Black, G., et al., *Bio-butanol: Combustion properties and detailed chemical kinetic model*. Combustion and Flame. **157**(2): p. 363-373.
30. Dagaut, P., S.M. Sarathy, and M.J. Thomson, *A chemical kinetic study of n-butanol oxidation at elevated pressure in a jet stirred reactor*. Proceedings of the Combustion Institute, 2009. **32**(1): p. 229-237.
31. Szwaja, S. and J.D. Naber, *Combustion of n-butanol in a spark-ignition IC engine*. Fuel. **89**(7): p. 1573-1582.
32. Behrens, D.A., I.C. Lee, and C.M. Waits, *Catalytic combustion of alcohols for microburner applications*. Journal of Power Sources. **195**(7): p. 2008-2013.
33. Nahar, G.A. and S.S. Madhani, *Thermodynamics of hydrogen production by the steam reforming of butanol: Analysis of inorganic gases and light hydrocarbons*. International Journal of Hydrogen Energy. **In Press, Corrected Proof**.
34. Wang, W. and Y. Cao, *Hydrogen production via sorption enhanced steam reforming of butanol: Thermodynamic analysis*. International Journal of Hydrogen Energy. **36**(4): p. 2887-2895.
35. Wang, W. and Y. Cao, *Hydrogen-rich gas production for solid oxide fuel cell (SOFC) via partial oxidation of butanol: Thermodynamic analysis*. International Journal of Hydrogen Energy. **35**(24): p. 13280-13289.
36. Lima da Silva, A. and I.L. Muller, *Hydrogen production by sorption enhanced steam reforming of oxygenated hydrocarbons (ethanol, glycerol, n-butanol and methanol):*

- Thermodynamic modelling*. International Journal of Hydrogen Energy. **36**(3): p. 2057-2075.
37. Rass-Hansen, J., et al., *Steam reforming of technical bioethanol for hydrogen production*. International Journal of Hydrogen Energy, 2008. **33**(17): p. 4547-4554.
  38. Lee, I.C., J.G. St. Clair, and A.S. Gamson, *Catalytic partial oxidation of isobutanol for the production of hydrogen*. International Journal of Hydrogen Energy. **37**(2): p. 1399-1408.
  39. Cai, W., P.R.d.l. Piscina, and N. Homs, *Hydrogen production from the steam reforming of bio-butanol over novel supported Co-based bimetallic catalysts*. Bioresource Technology. **107**(0): p. 482-486.
  40. Humer, S., et al., *Experimental and kinetic modeling study of combustion of JP-8, its surrogates and reference components in laminar nonpremixed flows*. Proceedings of the Combustion Institute, 2007. **31**(1): p. 393-400.
  41. Cooke, J.A., et al., *Computational and experimental study of JP-8, a surrogate, and its components in counterflow diffusion flames*. Proceedings of the Combustion Institute, 2005. **30**(1): p. 439-446.
  42. Honnet, S., et al., *A surrogate fuel for kerosene*. Proceedings of the Combustion Institute, 2009. **32**(1): p. 485-492.
  43. Dagaut, P., *Kinetics of jet fuel combustion over extended conditions: Experimental and modeling*. Journal of Engineering for Gas Turbines and Power-Transactions of the Asme, 2007. **129**(2): p. 394-403.
  44. Edwards, T.I.M., *Cracking and deposition behavior of supercritical hydrocarbon aviation fuels*. Combustion Science and Technology, 2006. **178**(1-3): p. 307-334.
  45. Corporan, E., et al., *Chemical, Thermal Stability, Seal Swell, and Emissions Studies of Alternative Jet Fuels*. Energy & Fuels. **25**(3): p. 955-966.
  46. Ibarreta, A.F. and C.-J. Sung, *Optimization of Jet-A fuel reforming for aerospace applications*. International Journal of Hydrogen Energy, 2006. **31**(8): p. 1066-1078.
  47. Campbell, T.J., et al., *JP-8 catalytic cracking for compact fuel processors*. Journal of Power Sources, 2004. **129**(1): p. 81-89.
  48. Krummenacher, J.J., K.N. West, and L.D. Schmidt, *Catalytic partial oxidation of higher hydrocarbons at millisecond contact times: decane, hexadecane, and diesel fuel*. Journal of Catalysis, 2003. **215**(2): p. 332-343.
  49. Shekhawat, D., et al., *Fuel constituent effects on fuel reforming properties for fuel cell applications*. Fuel, 2009. **88**(5): p. 817-825.
  50. Liu, D.-J., et al., *Characterization of kilowatt-scale autothermal reformer for production of hydrogen from heavy hydrocarbons*. International Journal of Hydrogen Energy, 2004. **29**(10): p. 1035-1046.
  51. Dreyer, B.J., et al., *Autothermal steam reforming of higher hydrocarbons: n-Decane, n-hexadecane, and JP-8*. Applied Catalysis A: General, 2006. **307**(2): p. 184-194.

52. Resini, C., et al., *Pt-Sn/ $\gamma$ -Al<sub>2</sub>O<sub>3</sub> and Pt-Sn-Na/ $\gamma$ -Al<sub>2</sub>O<sub>3</sub> catalysts for hydrogen production by dehydrogenation of Jet A-1 fuel: Characterisation and preliminary activity tests*. International Journal of Hydrogen Energy. **36**(10): p. 5972-5982.
53. Pasel, J., et al., *Autothermal reforming of commercial Jet A-1 on a scale*. International Journal of Hydrogen Energy, 2007. **32**(18): p. 4847-4858.
54. Goud, S.K., et al., *Steam reforming of -hexadecane using a catalyst: Kinetics of catalyst deactivation*. International Journal of Hydrogen Energy, 2007. **32**(14): p. 2868-2874.
55. Gallagher, M.J., et al., *On-board plasma-assisted conversion of heavy hydrocarbons into synthesis gas*. Fuel. **89**(6): p. 1187-1192.
56. Schmieder, R.W., *Radiotracer studies of soot formation in diffusion flames*. Symposium (International) on Combustion, 1985. **20**(1): p. 1025-1033.
57. Saffaripour, M., et al., *An Experimental Comparison of the Sooting Behavior of Synthetic Jet Fuels*. Energy & Fuels. **25**(12): p. 5584-5593.
58. Shaddix, C.R., et al., *Soot graphitic order in laminar diffusion flames and a large-scale JP-8 pool fire*. International Journal of Heat and Mass Transfer, 2005. **48**(17): p. 3604-3614.
59. Jensen, K.A., J.M. Suo-Anttila, and L.G. Blevins, *Measurement of soot morphology, chemistry, and optical properties in the visible and near-infrared spectrum in the flame zone and overfire region of large JP-8 pool fires*. Combustion Science and Technology, 2007. **179**(12): p. 2453-2487.
60. Yao, M., et al., *Experimental study of n-butanol additive and multi-injection on HD diesel engine performance and emission, 2010*. Fuel. **89**(9): p. 2191-2201.
61. Rakopoulos, D.C., et al., *Effects of butanol-diesel fuel blends on the performance and emissions of a high-speed DI diesel engine*. Energy Conversion and Management, 2010 **51**(10): p. 1989-1997.
62. Liu, H., et al., *Combustion Characteristics and Soot Distributions of Neat Butanol and Neat Soybean Biodiesel*. Energy & Fuels, 2011. **25**(7): p. 3192-3203.
63. Camacho, J., S. Lieb, and H. Wang, *Evolution of size distribution of nascent soot in n- and i-butanol flames*. Proceedings of the Combustion Institute, 2013 (34): p. 1853-1860.
64. Echavarria, C.A., et al., *Burnout of soot particles in a two-stage burner with a JP-8 surrogate fuel*. Combustion and Flame, 2012. **159**(7): p. 2441-2448.
65. Roesler, J.F., et al., *Investigating the role of methane on the growth of aromatic hydrocarbons and soot in fundamental combustion processes*. Combustion and Flame, 2003. **134**(3): p. 249-260.
66. Babkin, V.S., *Filtrational Combustion of Gases. Present State of Affairs and Prospects*. Pure & Appl. Chem., 1993. **65**(2): p. 335-344.
67. Leahey, D.M., *Computational Modeling of Fuel Reforming from Dry and Wet Ethanol-air Mixtures to Hydrogen in a Filtration Reactor*, M.S. Thesis. 2008, University of Texas at Austin: Austin, TX.

68. P. Bingue, J., et al., *Hydrogen production in ultra-rich filtration combustion of methane and hydrogen sulfide*. International Journal of Hydrogen Energy, 2002. **27**(6): p. 643-649.
69. Kennedy, L.A., et al., *Chemical Structures of Methane-Air Filtration Combustion Waves for Fuel-Lean and Fuel-Rich Conditions*. Proc. Combust. Inst., 2000. **28**: p. 1431-1438.
70. Al-Hamamre, Z., S. Voß, and D. Trimis, *Hydrogen production by thermal partial oxidation of hydrocarbon fuels in porous media based reformer*. International Journal of Hydrogen Energy, 2009. **34**(2): p. 827-832.
71. Mujeebu, M.A., et al., *A review of investigations on liquid fuel combustion in porous inert media*. Progress in Energy and Combustion Science, 2009. **35**(2): p. 216-230.
72. Howell, J.R., M.J. Hall, and J.L. Ellzey, *Combustion of Hydrocarbon Fuels within Porous Inert Media*. Prog. Energy Combust. Sci., 1996. **22**: p. 121-145.
73. Mujeebu, M.A., et al., *Trends in modeling of porous media combustion*. Progress in Energy and Combustion Science. **36**(6): p. 627-650.
74. Futko, S.I., *Effect of Kinetic Properties of a Mixture on Wave Macrocharacteristics of Filtration Combustion of Gases*. Combustion, Explosion, and Shock Waves, 2003. **39**(1): p. 11-22.
75. Foutko, S.I., et al., *Superadiabatic Combustion Wave in a Diluted Methane-Air Mixture under Filtration in a Packed Bed*. Proc. Combust. Inst., 1996. **26**: p. 3377-3382.
76. Vasu, S.S., D.F. Davidson, and R.K. Hanson, *Jet fuel ignition delay times: Shock tube experiments over wide conditions and surrogate model predictions*. Combustion and Flame, 2008. **152**(1-2): p. 125-143.
77. Hileman, et al., *Energy Content and Alternative Jet Fuel Viability*, American Institute of Aeronautics and Astronautics: Reston, VA, ETATS-UNIS. p. 12.
78. Babrauskas, V., *Ignition handbook : principles and applications to fire safety engineering, fire investigation, risk management and forensic science*. 2003, Issaquah, WA : [Bethesda, Md.] :: Fire Science Publishers ; Society of Fire Protection Engineers. viii, 1116 p. .:
79. Goodwin, D.G. *Cantera*. 2002-2007.
80. Smith, C.H., et al., *Conversion of Wet Ethanol to Syngas via Filtration Combustion: an Experimental and Computational Investigation*, in *6th U.S. National Combustion Meeting*, T.C. Institute, Editor. 2009, The Combustion Institute: Ann Arbor, MI.
81. Stanmore, B.R., J.F. Brilhac, and P. Gilot, *The oxidation of soot: a review of experiments, mechanisms and models*. Carbon, 2001. **39**(15): p. 2247-2268.
82. Warnatz, J., *Combustion : physical and chemical fundamentals, modeling and simulation, experiments, pollutant formation*. 4th ed. ed. 2006, Berlin ; New York :: Springer. xii, 378 p. .:
83. Dasch, C.J., *The decay of soot surface growth reactivity and its importance in total soot formation*. Combustion and Flame, 1985. **61**(3): p. 219-225.

84. Tsurikov, M.S., et al., *Laser-based investigation of soot formation in laminar premixed flames at atmospheric and elevated pressures*. Combustion Science and Technology, 2005. **177**(10): p. 1835-1862.
85. Al-Hamamre, Z. and M.A. Hararah, *Hydrogen production by thermal partial oxidation of ethanol: Thermodynamics and kinetics study*. International Journal of Hydrogen Energy. **35**(11): p. 5367-5377.
86. Dhamrat, R.S. and J.L. Ellzey, *Numerical and Experimental Study of the Conversion of Methane to Hydrogen in a Porous Media Reactor*. Combustion and Flame, 2006. **144**: p. 698-709.
87. Pedersen-Mjaanes, H., L. Chan, and E. Mastorakos, *Hydrogen Production from Rich Combustion in Porous Media*. Int. J. Hydrogen Energy, 2005. **30**: p. 579-592.

## Appendix B: Reforming of heptane in counterflow reactor

The second objective of this ARO-funded project was to demonstrate liquid fuel reforming capability in the counterflow reactor. This work is described below, and was published as *E.L. Belmont, S.M. Solomon, J.L. Ellzey, Combust. Flame 159 (2012) 3624-3631*.

One of the largest impediments to the implementation of hydrogen-based portable power technologies, such as fuel cells, is the lack of infrastructure for the production and distribution of hydrogen. [1]. Distribution of hydrogen entails significant challenges, many of which can be overcome if hydrogen is produced at the site of use from fuels that are more readily transported. These include natural gas and liquid hydrocarbon fuels, the latter of which have high volumetric energy density [2,3]. The ability to reform liquid fuels on a small scale and at the site of use therefore has the potential to replace or supplement batteries for energy storage.

Various reactors have employed the concept of heat recirculation through a solid matrix, with some designs having a means of stabilizing the reaction front. A two section porous media reactor can support a stationary combustion zone and this design has been used to reform rich mixtures of methanol, methane, octane and automotive-grade petrol [4]. Alternatively, a diverging section of porous media permits stabilized reaction zones for fuel reforming in porous media and has been used successfully in several studies [5,6,7]. In some heat recirculating reactors, the reaction front is not stabilized and propagates through the solid matrix. When the front propagates downstream, it passes over preheated solid and the gas gains additional energy, resulting in superadiabatic temperatures. These higher temperatures increase reaction rates and potentially result in high conversion efficiencies [8,9]. A disadvantage of this design is that the wave ultimately reaches the end of the reactor requiring periodic restarting or reversal of the flow [10].

The advantage of superadiabatic temperatures has been realized in other reactor designs as well. A Swiss roll reactor [11,12,13] has been used for both reforming and thermal oxidation [14]. In this reactor, heat from the exhaust is transferred through the walls to the incoming reactants. This basic principle was applied in the study of the counterflow reactor consisting of straight channels which simplify the geometry and permit a wide range of stable operating conditions. Figure B.1 is a schematic of the reactor. The flow direction alternates in adjacent channels so that energy from hot combustion products is transferred to cold incoming reactants. The preheated reactants may reach temperatures in the combustion zone that are superadiabatic. The counterflow reactor design has been proposed analytically [15,16,17] and validated in two experimental studies on the reforming of methane [18] and propane [19].

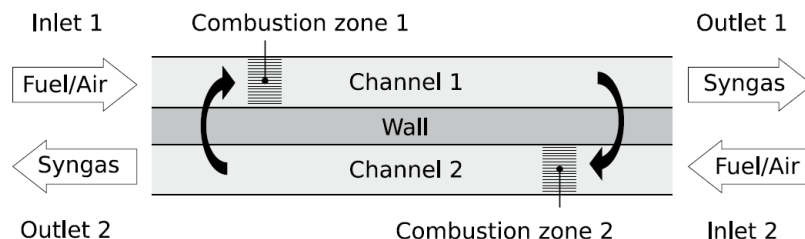


**Figure B.1: Counterflow reactor utilizes heat transfer from hot combustion products through channel walls to preheat incoming reactants**

One of the compelling characteristics of non-catalytic reactors is their ability to operate on various fuels. There have been numerous studies on the production of syngas from gaseous fuels [4,6,20,21,22], but fewer have done so from liquid fuels. In this study we established the first liquid fuel reforming, using heptane fuel, in the counterflow reactor. The results augment those obtained on an identical reactor using methane [18] and propane [19]. Heptane is a particularly interesting liquid fuel as a surrogate for commercial fuels. Dixon et al. [23] presented experimental and numerical analyses of syngas production from heptane in a porous media reactor. Equivalence ratio ( $\phi$ ) and inlet velocity ( $u$ ) were varied, and exhaust gas hydrogen concentrations were found to increase with both of these parameters. These trends are similar to those found in previous filtration combustion studies [4,21]. Pastore and Mastorakos [24] reformed heptane to syngas in a two-section porous burner and obtained comparable results to Dixon et al. [23] at some operating conditions but with a more limited stable burner range.

The earlier study of the porous media reactor operating on heptane provided guidance for this work. In that study [20], the reactor operated near the conventional flammability limits of heptane without prohibitive soot formation causing any observed degradation in performance. At more extreme conditions, soot buildup did pose a challenge, and Dixon et al. [23] developed a regeneration procedure that is utilized in this study as well. The non-catalytic surfaces of the counterflow reactor imply that small amounts of deposits should not degrade the performance as long as the channel dimensions and wall properties are not significantly changed due to buildup, thus opening the possibility of using fuels that may produce more soot.

In this work, we focused on conversion of heptane to syngas in the counterflow reactor. The operating limits and conversion efficiencies were determined, and these quantities were compared to those for the same reactor operating on methane and propane.

## **B.1 Experimental method**

### ***Experimental apparatus***

Figure B.2 shows the counterflow reactor, which is the same design used in previous studies on reforming of methane and propane [18,19]. It consists of four 4 mm high parallel channels

constructed of 1 mm thick silicon carbide (SiC) walls. The reactor is 17.3 cm long, with a 91.5 mm long main section and two 40.8 mm long reactor heads where inlets and outlets are located. Also located in the reactor heads are end plugs, which prevent the mixing of combustion products and unreacted fuel/air mixture, and two 6.4 mm wide sections of SiC porous foam (17.7 pores/cm, 9% density) which act as flow straighteners and flame arresters. Two alumina walls spaced 33.6 mm apart enclose the SiC channels. Fine wire B-type thermocouples are inserted into the channels through the alumina insulation 10 mm apart. They sit flush with the channel wall in order to prevent flame holding. The whole reactor is shrouded in alumina insulation to minimize heat losses. Further details about the reactor construction can be found in Schoegl and Ellzey [18].

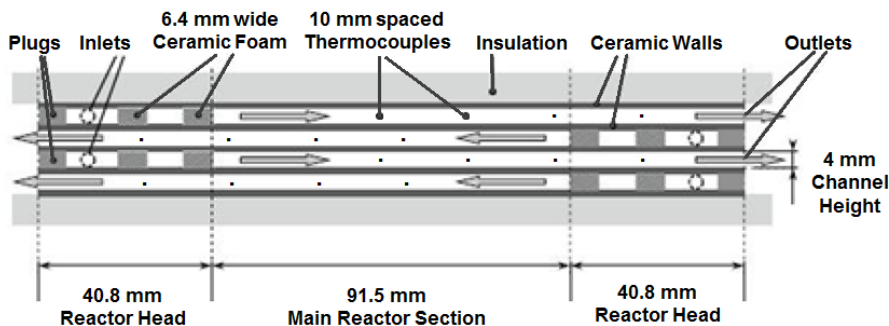


**Figure B.2: Counterflow reactor**

*n*-Heptane (Fisher Scientific, HPLC grade) is pumped to an atomizing nozzle mounted inside a mixing chamber. Air is fed to the mixing chamber using a Hastings mass flow controller. Downstream of the controller the total air is split between the atomizing nozzle and heater air by a control valve. The heated air is introduced into the annular space surrounding the nozzle in order to vaporize the atomized heptane and prevent condensation of heptane on the mixing chamber walls. The vaporized fuel/air mixture is fed into a manifold that splits the flow among the four channels. The delivery system, from the mixing chamber to the inlet ports, is wrapped in heat tape and monitored using K-type thermocouples to maintain the system above 150 °C.

Exhaust gas composition is analyzed using a Varian CP 4900 gas chromatograph (GC) with three columns: a molecular sieve (Molsieve) measures diatomic hydrogen (H<sub>2</sub>), nitrogen (N<sub>2</sub>), oxygen (O<sub>2</sub>), carbon monoxide (CO) and methane (CH<sub>4</sub>); a porous polymer unit (PPU) gives concentrations of carbon dioxide (CO<sub>2</sub>), ethylene (C<sub>2</sub>H<sub>4</sub>), ethane (C<sub>2</sub>H<sub>6</sub>), acetylene (C<sub>2</sub>H<sub>2</sub>) and propane (C<sub>3</sub>H<sub>8</sub>); and a CP-SIL column detects larger hydrocarbons (*i*-,*n*-) butane, (*i*-,*n*-) pentane, *n*-hexane and *n*-heptane. In order to quench reactions outside of the reactor and prevent moisture accumulation in the GC, exhaust samples are drawn from the reactor exhaust through a quartz probe. The sample then passes through inert Silco Steel tubing and a filter before entering the GC. Previous findings [19] showed slightly lower H<sub>2</sub> and CO product concentrations from outside channels and minimal variation of composition with position within a single channel

except near the alumina walls. Exhaust samples in this study were taken from the center channels, which are expected to be most representative of interior channels in scaled up reactors, and the sample probe was placed at the middle of the channel exit.

### **Experimental method**

The start-up procedure began with warming the system to above 150 °C using both heating tape and heated air flowing through the reactant delivery system and the reactor. A slightly rich, vaporized premixed heptane/air mixture was then introduced to the system and ignited at the channel outlets at an inlet velocity of 50 cm/s. Flame fronts propagated upstream in the reactor channels until they stabilized downstream of the porous SiC flow straighteners. Operating conditions were gradually adjusted to  $\phi = 3.0$  and  $u = 125$  cm/s, where the reactor was operated until temperatures stabilized. The initial warm-up phase took approximately 30-45 minutes.

Experiments included determination of stable operating conditions, and studying the effect of inlet velocity and equivalence ratio variation on exhaust gas composition. Test conditions were considered stable if combustion could be sustained in the main reactor section for ten minutes. Alumina reactor wall temperatures in each of the four channels were monitored throughout the experiments. Gas temperatures were not directly measured due to the tendency of thermocouples inserted into the channels to act as flame holders; however, an analytical model of the counterflow reactor predicts peak gas temperatures significantly above the maximum wall temperatures [20]. Peak temperatures were recorded after the reactor stabilized at a given set point, and showed less than  $\pm 5$  °C variation during the time of continuous operation at that set point and while exhaust gas samples were taken. All data presented in this study were taken at operating points that met the above criterion for stability, and no directional drift in measured temperatures or species concentrations was observed with repeated sampling.

Inlet velocity and equivalence ratio were changed in steps of  $\Delta u = 15$  cm/s and  $\Delta\phi = 0.1$ , respectively, and the inlet velocity was specified at standard conditions of 25 °C and 1 atm. Results were obtained for variation of inlet velocity from 50-200 cm/s with equivalence ratio held constant at 3.0, and variation of equivalence ratio from 2.9-3.8 with inlet velocity held constant at 125 cm/s. The inlet velocity range was restricted at the upper limit in order to avoid damage to the reactor due to wall temperatures approaching 1300 °C, while the lower limit was determined by flame instability and extinction. The equivalence ratio range was limited by flashback on the lean end of the tested range, in which the flame propagated upstream into the porous SiC foam, and blowoff on the rich end, where the flame front propagated out the end of the reactor. Significant deposits of soot and pyrolytic graphite [25] were observed during extended periods of operation at the highest tested equivalence ratios and inlet velocities. For all experimental conditions reported in this paper, the soot build-up was prevented by briefly interrupting the fuel and purging the reactor with air for 10-20 seconds before continuing the

experiments. At high equivalence ratio and inlet velocity operating points, where soot buildup was most likely, the reactor was purged approximately every 20 minutes.

At each operating point, five consecutive GC measurements were taken and the first two were discarded to ensure that any residual gases in the sample line had been eliminated. Each operating point was tested twice, giving a total of six data points. Total uncertainty was calculated at each operating point as the root-sum-square of the contributing uncertainties. Therefore the uncertainty of GC results is due to repeatability of measurements, calculated using a student-t distribution, calibration gases, with specified uncertainties of 1-5%, and the GC itself with uncertainty of 1% of the maximum calibrated value for each species. The error bars shown in plotted results represent average uncertainties for each set of operating conditions. Inlet velocity uncertainty is due to uncertainties of 1% of the air flow controller maximum flow rate and 2% of the rotameter maximum flow rate, as well as an estimated 5% tolerance of the channel cross-sectional area. Equivalence ratio uncertainty is due to contributions from the air flow controller and rotameter. Inlet velocity uncertainty increases with increasing  $u$ , where  $\delta u = \pm 4.0$  cm/s at  $u = 50$  cm/s and  $\delta u = \pm 10.3$  cm/s at  $u = 200$  cm/s. Equivalence ratio uncertainty increases slightly with increasing  $\phi$  but more significantly with decreasing  $u$ , with  $\delta\phi = \pm 0.05$  at  $u = 200$  cm/s and  $\delta\phi = \pm 0.20$  at  $u = 50$  cm/s.

## B.2 Results and discussion

### Operating Range

One of the critical aspects of the counterflow reactor is the ability to recirculate heat from the hot products to the incoming reactants in the neighboring channel. The preheating increases the burning rate for a reactant mixture compared to standard conditions. The combustion zone stabilizes at a position in the reactor where the burning rate is balanced by the inlet velocity. For example, increasing the equivalence ratio from 3.2 to 3.6 at a fixed velocity results in lower heat release and the stable position for the flame is further downstream in the channel where the heat recirculation is more significant. Ultimately as the equivalence ratio is increased further, heat release and recirculation are insufficient compared to heat losses and the flame blows off. If instead heat release is increased compared to heat losses, for example by lowering the equivalence ratio from 3.2 to 2.8 at a constant inlet velocity, then the combustion zone will migrate upstream to a stable position where heat recirculation is reduced. With further reduction in equivalence ratio the flame will propagate into the porous flow straighteners and flash back.

Figure B.3 shows the stable operating conditions for premixed heptane/air reactants. As the velocity increases, flashback occurs at leaner conditions. For example, flashback occurs at  $\phi = 2.9$  at an inlet velocity of 50 cm/s. At  $u = 200$  cm/s, where heat release and the burning rate are greater, flashback occurs at the leaner condition of  $\phi = 2.7$ . Similarly, blowoff occurs at  $\phi = 4.0$  when the inlet velocity is 50 cm/s and  $\phi = 3.6$  when the inlet velocity is 200 cm/s. Extinction

occurs at inlet velocities below 50 cm/s due to excessive heat losses relative to heat release rates. The two sets of test conditions at which exhaust gas composition were evaluated,  $\phi = 3.0$  with inlet velocity varied from 50-200 cm/s and  $u = 125$  cm/s with equivalence ratio varied from 2.9-3.8, are highlighted in the figure. These values were selected because the reactor operating range is relatively large and equilibrium predicts that the conversion of heptane to hydrogen is maximum at an equivalence ratio of 2.9.

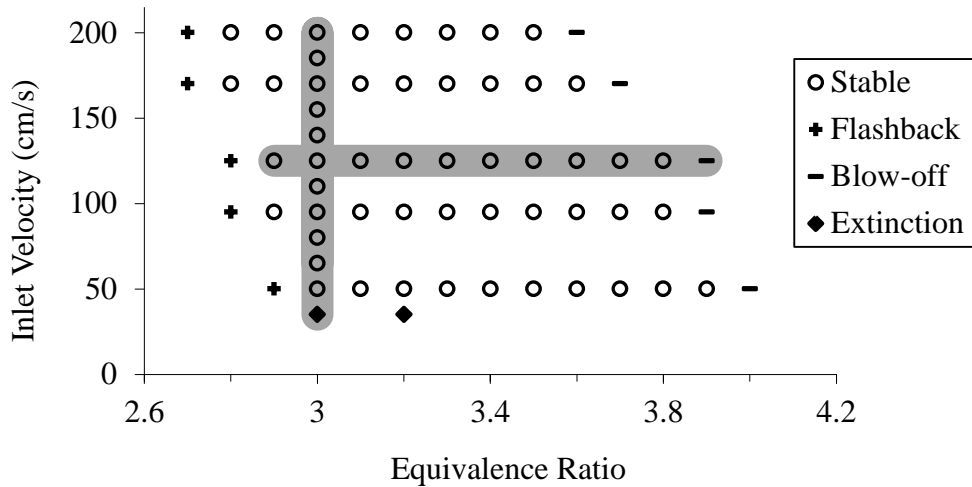


**Figure B.3: Stable and unstable operating conditions, with highlighted operating points where exhaust gas composition was analyzed**

**Combustion temperature and exhaust gas composition**

Although equilibrium calculations should not necessarily predict the products of the reactor, they do form a standard for comparison of trends as well as degree of reaction progression. In Table B.1, equilibrium values are determined for a constant pressure, adiabatic system. Wet and dry equilibrium values are tabulated for  $\phi = 3.0$  and  $\phi = 3.5$ , where dry values do not include water in the equilibrium composition and will be used for comparison against experimental results. Oxygen, heptane, and most other hydrocarbons including  $C_2H_2$ ,  $C_2H_6$  and  $C_3H_8$  are not present in significant amounts in the equilibrium composition. Methane is the only unburned hydrocarbon present in non-negligible amounts, and its concentration increases with increasing equivalence ratio. Another compositional change that correlates to an increasing  $\phi$  is the appearance of solid carbon. The adiabatic equilibrium temperature is predicted to decrease from 808.9 °C to 774.6 °C as equivalence ratio increases from  $\phi = 3.0$  to  $\phi = 3.5$ .

$\phi$	<b>3.0</b>	<b>3.0</b>	<b>3.5</b>	<b>3.5</b>
	<b>WET</b>	<b>DRY</b>	<b>WET</b>	<b>DRY</b>
<b>T (°C)</b>	808.9	808.9	774.6	774.6
<b>H2 [%]</b>	26.61	26.82	28.00	28.33
<b>H2O</b>	0.75	--	1.15	--
<b>CO</b>	23.46	23.64	20.51	20.75
<b>CH4</b>	0.29	0.29	0.49	0.49
<b>C2H2</b>	<1E-5	<1E-5	<1E-5	<1E-5
<b>C2H6</b>	<1E-5	<1E-5	<1E-5	<1E-5
<b>C3H8</b>	<1E-5	<1E-5	<1E-5	<1E-5
<b>N2</b>	48.17	48.54	44.50	45.01
<b>C(s)</b>	0.00	0.00	4.35	4.40

**Table B.1: Equilibrium values of adiabatic equilibrium temperature and product composition for premixed heptane/air reactant mixtures of  $\phi = 3.0$  and  $\phi = 3.5$**

Figures B.4-B.5 and B.6-B.7 show experimental measurements of exhaust gas composition and peak reactor wall temperatures as functions of equivalence ratio and inlet velocity, respectively. A key feature of heat recirculating reactors is their ability to produce superadiabatic temperatures, which are necessary to increase reaction rates and achieve high conversion efficiency [23,26]. Figures B.4 and B.6 illustrate that the peak wall temperature for all cases is superadiabatic. Temperatures follow the trend of equilibrium and exceed the adiabatic equilibrium temperature by 190-460 °C in constant equivalence ratio tests, and 290-380 °C in constant inlet velocity tests.

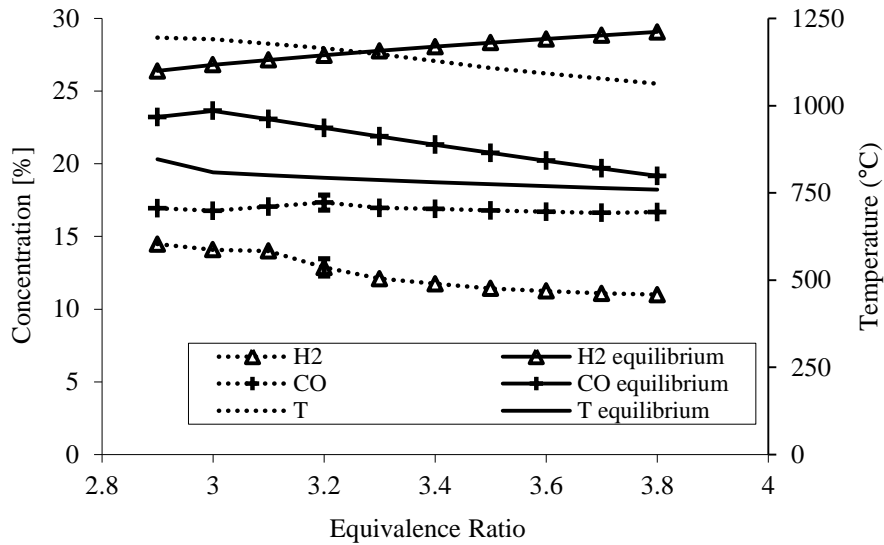
Figure B.4 also shows the impact of varying equivalence ratio on major exhaust components H2 and CO. Experimental measurements of CO concentration show little change over the range of tested equivalence ratios, and results are within the average uncertainty. In contrast to equilibrium values, experimental values of H2 concentrations decrease with increasing equivalence ratio. Despite peak reactor temperatures in excess of theoretical adiabatic temperatures, both H2 and CO concentrations are below equilibrium values. This is attributed to a significant amount of unconverted hydrocarbons and is indicative that the reactions did not proceed to equilibrium within the residence time of the reactor. Such results have been suggested in calculations done previously by Al-Hamamre et al. [6] for methane, in which an initial sharp increase in product concentration is observed followed by a more gradual increase towards equilibrium over time scales that are significantly longer than those that exist in the present experiments.

Figure B.5 shows experimental values of intermediate hydrocarbons in the reactor. Total unburned hydrocarbons (UHC) increase monotonically from 5.2% to 9.8% with increasing equivalence ratio. Methane and ethylene, with H/C ratios of 4 and 2 respectively, both increase with equivalence ratio while acetylene, with an H/C ratio of 1, decreases. This shows that hydrogen is increasingly bound in hydrocarbons rather than in diatomic hydrogen. Ethane,

propane and *i*-butane concentrations increase with increasing equivalence ratio, but are at all points present in amounts less than 0.2% and are not shown. At high equivalence ratios, the results show carbon monoxide near equilibrium and measured UHC in excess of equilibrium. The amount of carbon in exhaust species that are not measured by GC can be estimated using a carbon balance. Based on the species that are measured by GC, with carbon numbers up to C7, it is expected that the unmeasured species are larger hydrocarbons and possibly soot. At the highest equivalence ratio of 3.8, the experimental carbon balance shows that ~11% of incoming carbon is contained in species not measured by the GC. In contrast, equilibrium predicts that ~25% of incoming carbon goes to form solid carbon product. Therefore, in experiments there are higher values of measured UHC than equilibrium predicts but lower values of higher hydrocarbons and soot.

Combustion chemistry literature provides insight into oxidation of rich hydrocarbon mixtures and aids in interpretation of these trends. *n*-Heptane oxidation is initiated via H abstraction by H, O or OH radicals. The resultant heptyl radical is then susceptible to breakdown by  $\beta$ -scission to produce ethylene and pentyl radical. The latter undergoes repeated further  $\beta$ -scission to produce ethylene and a methyl radical. Ethylene may react with an O radical to form a methyl radical and HCO, or in fuel rich mixtures ethylene undergoes further H abstraction by H and OH radicals to produce a vinyl radical, which quickly reacts to form acetylene. Therefore acetylene appears as a product further along in the progression of the complex hydrocarbon breakdown process. Methane can form through multiple pathways, both as an early and a late breakdown product [27]. Constant inlet velocity results show via the correlation of methane with ethylene trends that its formation is not predominantly due to further reduction of acetylene.

Although hydrocarbons larger than C7 were not measured, soot formation was observed at high equivalence ratios and inlet velocities. The data are too limited to draw conclusions about the pathway of polycyclic aromatic hydrocarbons (PAH) formation, but it is interesting to note that acetylene, which is present at all operating points in excess of equilibrium concentrations, participates in the chemistry of formation of PAH, a precursor to soot [27].



**Figure B.4: Exhaust gas and equilibrium concentrations of H<sub>2</sub> and CO, and peak wall and adiabatic equilibrium temperatures for  $u = 125$  cm/s and varying  $\phi$**

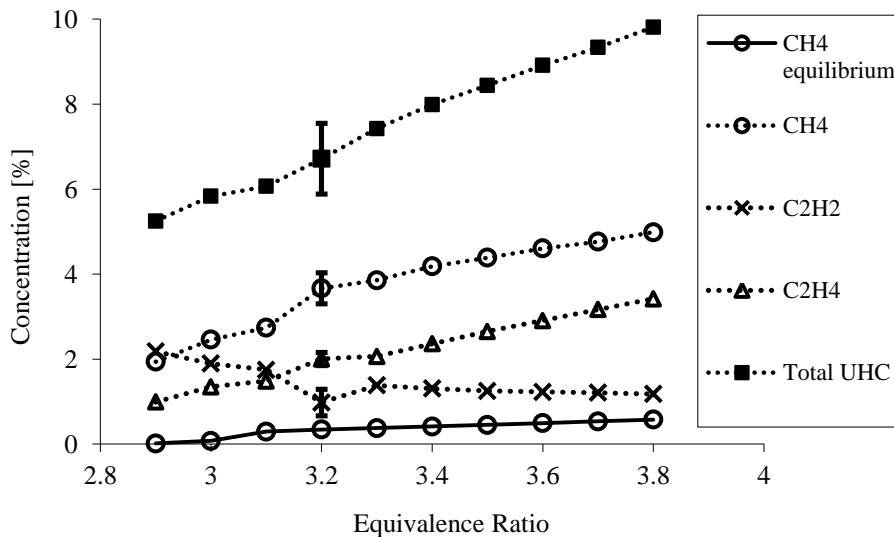


**Figure B.5: Exhaust gas concentrations of CH<sub>4</sub>, C<sub>2</sub>H<sub>2</sub>, C<sub>2</sub>H<sub>4</sub> and total UHC, and equilibrium concentrations of CH<sub>4</sub> (equilibrium concentrations of C<sub>2</sub>H<sub>2</sub> and C<sub>2</sub>H<sub>4</sub> are negligible and not shown) for  $u = 125$  cm/s and varying  $\phi$**

Figure B.6 shows the impact of inlet velocity on peak reactor wall temperature and on the concentrations of H<sub>2</sub> and CO. Equilibrium values are shown for comparison. In experiments with increasing velocity, the volumetric heat release rate increases resulting in higher peak temperatures. The H<sub>2</sub> concentration is influenced by two competing effects in this system. Higher temperatures increase the reaction rate and result in faster fuel conversion [18,23], however, increased velocities imply shorter residence times which may counteract the influence

of the higher temperatures [19]. These competing effects are reflected in experimental values of H<sub>2</sub> concentrations, which increase initially at velocities up to 80 cm/s and then remain nearly constant. CO concentrations show minimal change with inlet velocity. The increase in H<sub>2</sub> and UHC (Fig. B.7) with no corresponding increase in carbon monoxide at lower inlet velocities suggests that larger intermediate hydrocarbons not measured by the GC may be present at the lowest  $u$ . Molecular hydrogen is released as those species are further broken down, while carbon remains bound in the smaller intermediate hydrocarbon species.

Figure B.7 shows exhaust gas concentrations of CH<sub>4</sub>, C<sub>2</sub>H<sub>2</sub> and C<sub>2</sub>H<sub>4</sub>, as well as total UHC, for  $\phi = 3.0$  and varying  $u$ . All other measured hydrocarbons are present in levels less than 0.1%. Total unburned hydrocarbons remain constant within the margin of uncertainty at an average value of 5.5% up to an inlet velocity of 155 cm/s, above which the total decreases monotonically to 4.4% at 200 cm/s. Acetylene, which is a species formed late in hydrocarbon breakdown, initially increases in concentration with increasing inlet velocity up to 80 cm/s and subsequently decreases at higher inlet velocities. Methane and ethylene increase with inlet velocity up to  $u = 155$  cm/s, above which concentrations decrease with further increase in velocity. Ethylene is less reduced than acetylene and forms earlier in hydrocarbon breakdown. The existence of a peak acetylene value followed by ethylene and methane maxima at higher inlet velocities suggests that fuel breakdown is diminished by decreased residence time. At the highest inlet velocities, ethylene and methane concentrations as well as total measured unburned hydrocarbons decrease. In conjunction with no increase in H<sub>2</sub> levels and visual observation of significant soot formation, the results suggest that fuel breakdown is promoted by high temperatures but intermediate species may form larger soot precursors instead of further reduction at the highest inlet velocities.

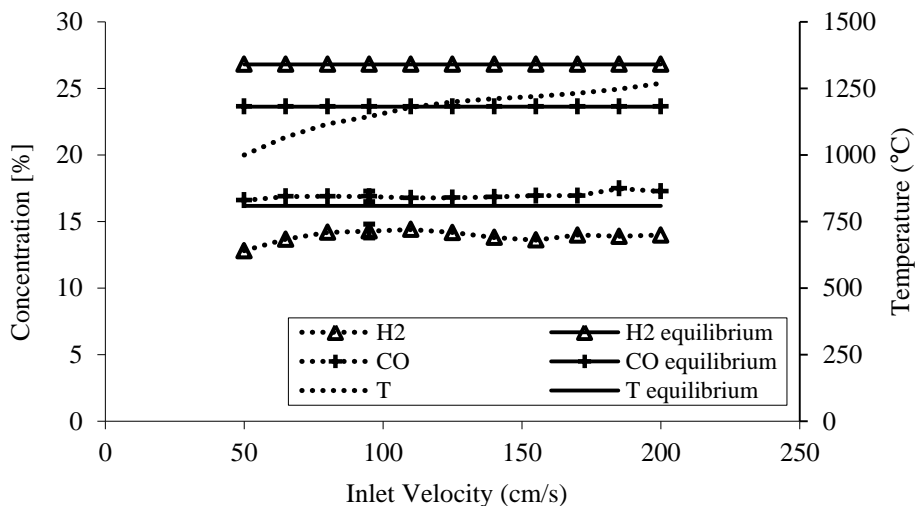


**Figure B.6: Exhaust gas and equilibrium concentrations of H<sub>2</sub> and CO, and peak wall and adiabatic equilibrium temperatures for  $\phi = 3.0$  and varying  $u$**

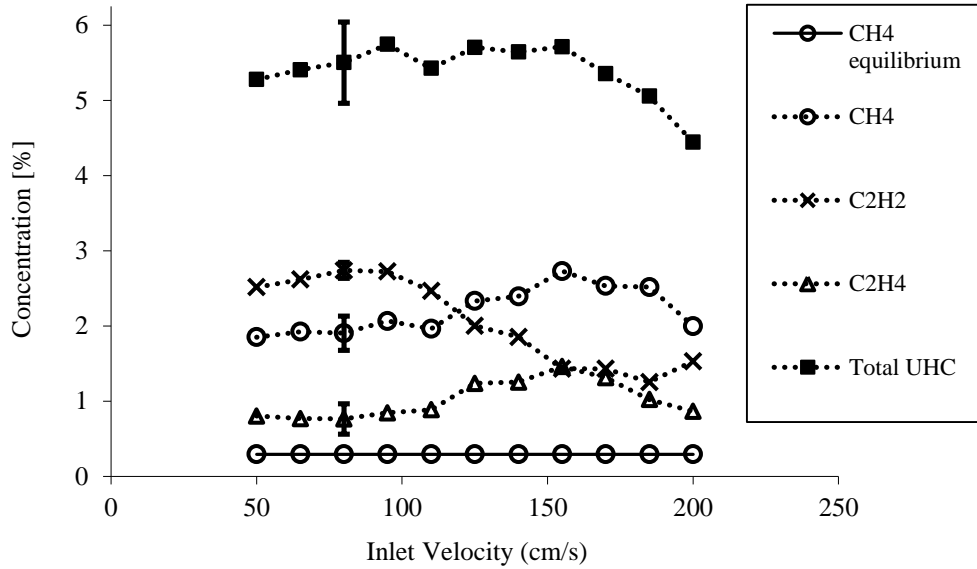


**Figure B.7: Exhaust gas concentrations of CH<sub>4</sub>, C<sub>2</sub>H<sub>2</sub>, C<sub>2</sub>H<sub>4</sub> and UHC, and equilibrium concentrations of CH<sub>4</sub> (equilibrium concentrations of C<sub>2</sub>H<sub>2</sub> and C<sub>2</sub>H<sub>4</sub> are negligible and not shown) for  $\phi = 3.0$  and varying  $u$**

### Fuels comparisons

The conversions of methane [18] and propane [19] to syngas were investigated in earlier studies using the counterflow reactor design. We compared results for heptane to those from the previous publications using three metrics: species conversion efficiency, and species and total energy conversion efficiencies.

Species conversion efficiency, also called species yield, compares actual species production to the theoretical maximum based on the amount of that species' components bound in the reactant fuel stream. Equation B.1 gives H<sub>2</sub> conversion efficiency, which is the number of moles generated compared to the number of moles of hydrogen bound in the heptane feedstock.

$$\eta_{H_2} = \frac{\dot{N}_{H_2}}{\dot{N}_{H_2, \max}} = \frac{\dot{N}_{H_2}}{8\dot{N}_{C_7H_{16}}} \quad (\text{B.1})$$

Species energy conversion efficiency represents the amount of chemical energy bound in a product species compared to the total chemical energy in the reactant fuel. Chemical energy is represented by the lower heating value (LHV) in kJ/kmol at standard conditions. Equation B.2 gives H<sub>2</sub> energy conversion efficiency.

$$\eta_{Energy,H_2} = \frac{\dot{N}_{H_2} LHV_{H_2}}{\dot{N}_{C_7H_{16},in} LHV_{C_7H_{16}}} \quad (B.2)$$

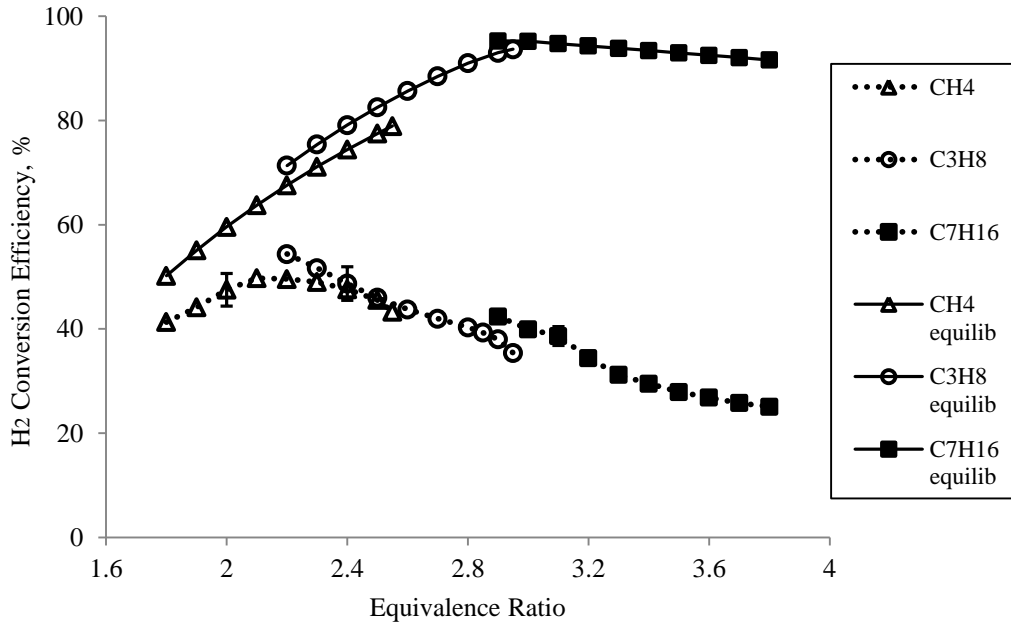
Total energy conversion efficiency compares the chemical energy bound in all of the energy containing product species to the initial chemical energy of the reactant fuel. The difference between the two is the sum of energy lost to surroundings and sensible enthalpy of the product gas. Equation B.3 gives total energy conversion efficiency.

$$\eta_{Energy,total} = \frac{\sum_{out} \dot{N}_i LHV_i}{\dot{N}_{C_7H_{16},in} LHV_{C_7H_{16}}} \quad (B.3)$$

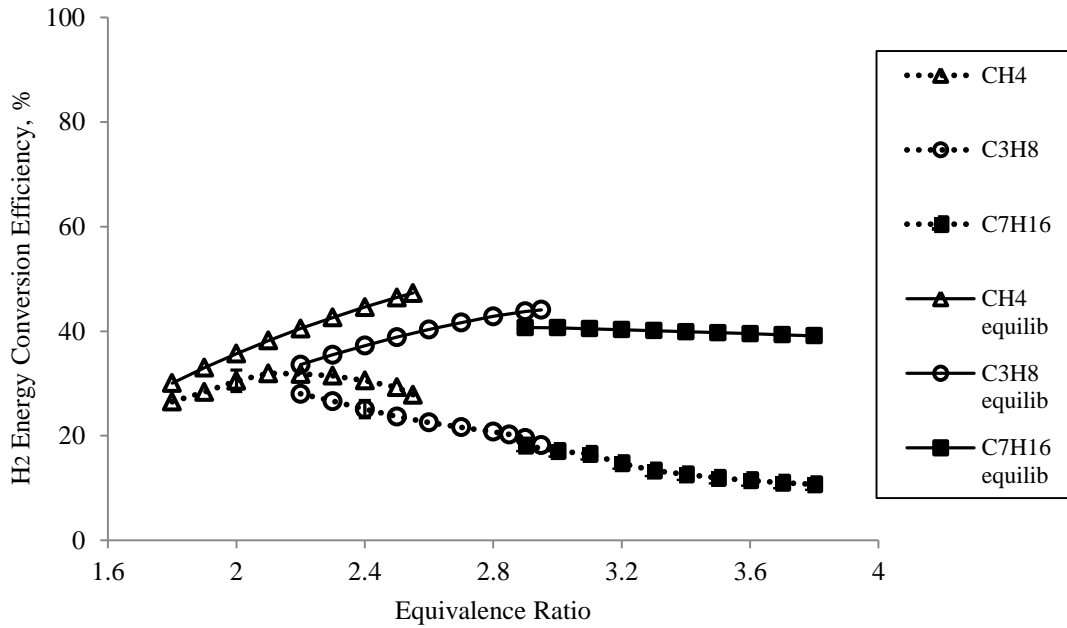
Figures B.8-B.10 show experimental and equilibrium results of methane, propane and heptane reforming in terms of the above three metrics for experiments in which inlet velocity was held constant at 125 cm/s and equivalence ratio was varied. Experiments were conducted over different equivalence ratio ranges because of differences in stability when operating the reactor with the three fuels. As previously discussed, the combustion zone is stable within the reactor when the inlet velocity equals the burning rate, which is a function of temperature. Variation in temperature between the three studies is due to differences in the adiabatic equilibrium temperatures of different reactant species, equivalence ratios, and levels of preheat. Heptane and propane have higher adiabatic equilibrium temperatures than methane. In addition, heptane is preheated to maintain the vapor phase; therefore preheated heptane has a higher adiabatic equilibrium temperature than propane. For example, the adiabatic equilibrium temperatures of propane and heptane at 25 °C for  $\phi = 2.9$  are 850 °C and 847 °C, whereas the equilibrium temperature of heptane increases to 934 °C when the reactants are preheated to 150 °C. Due to these differences, an equivalence ratio and velocity combination that is in the stable range but near the flashback limit for methane will be outside the stable range for propane. The same is true for propane and heptane. A comparison of burner maps for the three studies [18,19] further illustrates these stability differences.

Methane is the only one of the three fuels that shows a maximum value in the experimental results of hydrogen species (Fig. B.8) and energy (Fig. B.9) conversion efficiencies under the tested conditions. Methane, propane and heptane efficiencies decrease with increasing equivalence ratio above  $\phi = 2.2$ , and experimental conversion efficiencies are significantly less than predicted by equilibrium at these points, despite a peak hydrogen conversion efficiency for heptane predicted at  $\phi = 2.9$  by equilibrium. The occurrence of peak conversion efficiency at equivalence ratios below those predicted by equilibrium is consistent with the results of Al-

Hamamre et al. [6] for methane, in which incomplete conversion occurs on counterflow reactor timescales. This suggests that propane and heptane might also produce peak H<sub>2</sub> at a leaner operating point if such stable operation were possible but, as discussed above, leaner operation is limited by flashback and therefore these points could not be tested. The results also indicate that the current reactor design does not permit complete fuel conversion at high equivalence ratios.

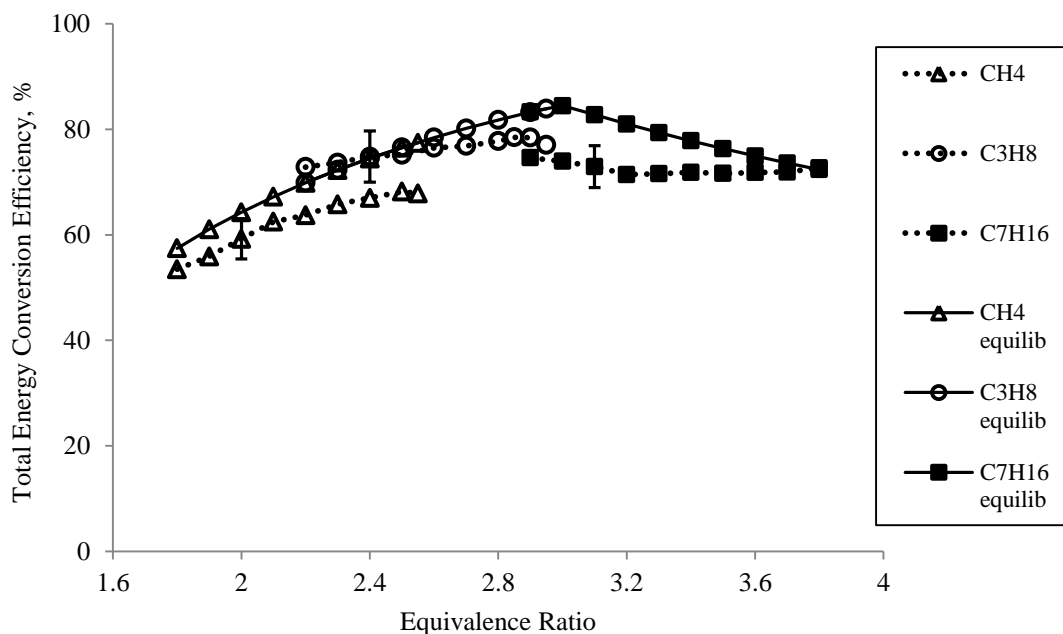


**Figure B.8: Experimental and equilibrium values of H<sub>2</sub> conversion efficiencies of methane [21], propane [22] and heptane reforming with constant  $u = 125$  cm/s and varying equivalence ratio**



**Figure B.9: Experimental and equilibrium H<sub>2</sub> energy conversion efficiencies of methane [21], propane [22] and heptane reforming with constant  $u = 125$  cm/s and varying equivalence ratio**

Experimental values of total energy conversion efficiencies show trends and values similar to equilibrium (Fig. B.10) for the three data sets. In each case unburned hydrocarbon concentrations increase with increasing equivalence ratio [18,19], and the chemical energy bound in those hydrocarbons contributes significantly to the total. Peak reactor temperatures decrease with increasing equivalence ratio for all three fuels [18,19]. This lessens convective and radiative losses to the environment as well as energy required to increase product gas enthalpy.



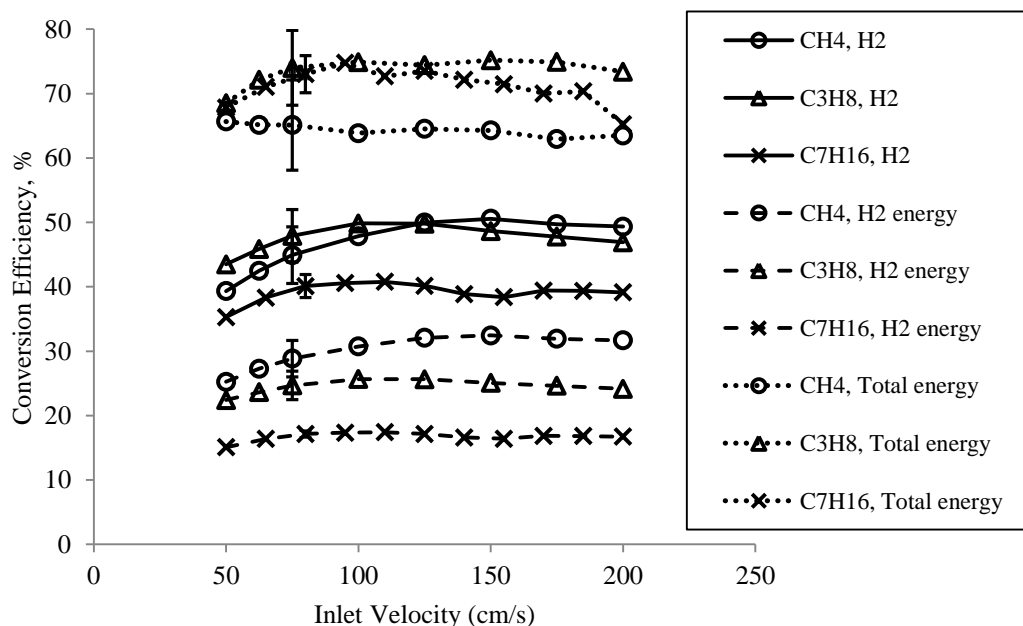
**Figure B.10: Experimental and equilibrium total energy conversion efficiencies of methane [21], propane [22] and heptane reforming with constant  $u = 125$  cm/s and varying equivalence ratio**

Figure B.11 shows the results of methane, propane and heptane reforming in terms of species and energy conversion efficiencies for experiments in which inlet velocity was varied from 50-200 cm/s and equivalence ratio was held constant at  $\phi = 2.2$  for methane,  $\phi = 2.4$  for propane and  $\phi = 3.0$  for heptane. All conversion efficiencies, with the exception of methane total energy conversion efficiency, increase initially with inlet velocity and show little change at higher  $u$ . The initial increase supports the discussion above for heptane that conversion improves with increased energy release rates and resultant higher peak temperatures. The marginal change over the remainder of the tested inlet velocity range suggests that product composition is affected by competing effects of increased temperature, which promotes conversion, and reduced residence time, which inhibits conversion. The decrease in total energy conversion efficiency of heptane at the highest  $u$  is attributed to the formation of soot, which consists of high chemical energy species that are not accounted for by GC measurements.

Heptane conversion has also been studied in filtration reactors consisting of a column of porous media which showed a broader operating range of 1.4-3.8 in comparison to the stable range of 2.8-3.9 in the counterflow reactor [23]; however both reactors were tested at or near an equivalence ratio of 2.9, where peak hydrogen conversion efficiency is estimated from equilibrium calculations to occur. The tested range in the current study also partially overlaps the equivalence ratio range of 2.5-3.5 that was estimated by Dixon et al. [23] to be favorable conditions for heptane reforming in a filtration reactor. Pastore and Mastorakos [24] reported

that the peak conversion efficiencies for heptane occurred at equivalence ratios of 1.8- 2.5 depending on the reactor. These differing values of the optimum equivalence ratio indicate that conversion is sensitive to the details of the reactor and operating conditions.

Peak H<sub>2</sub> conversion efficiencies from the counterflow reactor were less than those obtained in porous media, from which efficiencies of greater than 80% were obtained. Hydrocarbon product concentrations in the porous reactor were significantly lower than those measured in the counterflow reactor, at less than 1% compared to 5.8%, indicating more complete fuel breakdown. Peak temperatures in porous media were in excess of 1400 °C at  $\phi = 3.0$  and  $u = 60$  cm/s, compared to 1190 °C at  $\phi = 3.0$  and  $u = 125$  cm/s in the counterflow reactor. Residence times for the porous media and counterflow reactors were approximately the same at these operating conditions, with both on the order of 100 ms. The difference in conversion efficiency is attributed to higher peak temperatures in the porous media reactor [19,28].



**Figure B.11: H<sub>2</sub>, H<sub>2</sub> energy and total energy conversion efficiencies of methane ( $\phi = 2.2$ ) [21], propane ( $\phi = 2.4$ ) [22] and heptane ( $\phi = 3.0$ ) with varying inlet velocity**

### B.3 Conclusions

Experimental results of non-catalytic reforming of heptane to produce hydrogen-rich syngas in a counterflow reactor were presented. A key advantage of this reactor is that the reaction zones are stationary, which permits continuous operation and practical applications. Stable operation of the reactor with premixed heptane/air reactants was established for equivalence ratios between 2.8 and 3.9 and inlet velocities between 50 cm/s and 200 cm/s. Peak wall temperatures were

monitored throughout reactor operation and were at all points in excess of the adiabatic equilibrium temperature, thus excess-enthalpy flames were achieved through internal heat recirculation.

Exhaust gas composition was measured using gas chromatography for two sets of tests: equivalence ratio was varied from 2.9-3.8 with inlet velocity held constant at 125 cm/s, and equivalence ratio was held constant at 3.0 with inlet velocity varied from 50-200 cm/s. H<sub>2</sub> concentration decreased with increasing equivalence ratio from a maximum of 14.5% to a minimum of 10.6%, while CO concentration remained nearly constant around 17.0%. Both H<sub>2</sub> and CO concentrations showed little dependence overall on inlet velocity, with the former varying from 12.8-14.4% and the latter varying between 16.6-17.5%. The largest effect of inlet velocity was found at the lower end of the tested range where rates of heat release and temperatures are lower.

In all cases, unburned hydrocarbons were measured in excess of concentrations predicted by equilibrium composition. Total unburned hydrocarbon levels increased with increasing equivalence ratio. Soot was noted with significant formation observed at higher equivalence ratios and inlet velocities. These results and observations strongly suggested that the extent of fuel breakdown is reduced by insufficient reaction rate and residence time.

The results of this study showed trends similar to previously published studies on syngas production from methane and propane using the counterflow reactor [18,19]. Each fuel had H<sub>2</sub> species and energy conversion efficiencies below equilibrium values, but total conversion efficiencies were comparable to equilibrium. In addition, energy-dense unburned hydrocarbon concentrations were in excess of equilibrium with concentrations an order of magnitude higher than predicted by equilibrium at the highest tested equivalence ratios in this study. The comparison between the different fuels indicates that, although the stable operating range for heptane does include the theoretically optimal value as predicted by hydrogen conversion efficiencies calculated from equilibrium, the current reactor design does not permit complete fuel conversion at high equivalence ratios. In addition, the formation of soot at some conditions suggests the importance of operating at more moderate conditions for optimal performance.

This study demonstrated the fuel flexibility of the counterflow reactor by reforming a liquid fuel, and results supplemented previous reforming studies on the counterflow reactor. Peak H<sub>2</sub> conversion efficiency was significantly lower than that attained via filtration combustion in porous media, an alternate method of non-catalytic reforming. Differences were attributed to higher peak temperatures in the porous media reactor, which has higher specific surface area for heat transfer as compared to the counterflow reactor under investigation. Furthermore, although the tested equivalence ratio range in this study does include  $\phi = 2.9$ , where peak conversion efficiency is predicted to occur by equilibrium, previous studies predict peak conversion

efficiencies over a range of  $\phi = 1.8$  to  $\phi = 3.5$ . The results of hydrogen conversion in this study indicate that the optimum equivalence ratio might be outside the operating range of the counterflow reactor.

#### B.4 References

1. M. Krumpelt, T.R. Krause, J.D. Carter, J.P. Kopasz, S. Ahmed, *Catal. Today* 77 (2002) 3–16.
2. W.C. Lattin, V.P. Utgikar, *Int. J. Hydrogen Energy* 32 (2007) 3230 – 3237.
3. J.J. Romm, *The hype about hydrogen*, Island Press, 2004.
4. H. Pedersen-Mjaanes, L. Chan, E. Mastorakos, *Int. J. Hydrogen Energy* 30 (2005) 579–592.
5. G. Vourliotakis, G. Skevis, M.A. Founti, Z. Al-Hamamre, D. Trimis, *Int. J. Hydrogen Energy* 33 (2008) 2816-2825.
6. Z. Al-Hamamre, S. Voß, D. Trimis, *Int. J. Hydrogen Energy* 34 (2009) 827-832.
7. J.M.C. Pereira, M.A.A. Mendes, D. Trimis, J.C.F. Pereira, *Fuel* 89 (2010) 1928-1935.
8. J.P. Bingué, A.V. Saveliev, L.A. Kennedy, *Int. J. Hydrogen Energy* 29 (2004) 1365-1370.
9. V.S. Babkin, I. Wierzba, G.A. Karim, *Chem. Eng. J.* 91 (2003) 279–285.
10. M.K. Drayton, A.V. Saveliev, L.A. Kennedy, A.A. Fridman, Y-E. Li, *Proc. Comb. Inst.* 27 (1998) 1361–1367.
11. S.A. Lloyd, F.J. Weinberg, *Nature* 251 (1974) 47–49.
12. S.A. Lloyd, F.J. Weinberg, *Nature* 257 (1975) 367–370.
13. C.-H. Chen, P. D. Ronney, *Proc. Comb. Inst.* 33 (2011) 3285–3291.
14. J. Ahn, C. Eastwood, L. Sitzki, P.D. Ronney, *Proc. Combust. Inst.* 30 (2005) 2463–2472.
15. R.V. Fursenko, S.S. Minaev, and V.S. Babkin, *Combust. Explos. Shock Waves* 37(5) (2001) 493- 500.
16. Y. Ju, C.W. Choi, *Combust. Flame* 133 (2003) 483-493.
17. I. Schoegl, J.L. Ellzey, *Combust. Flame* 151(1-2) (2007) 142-159.
18. I. Schoegl, J.L. Ellzey, *Proc. Comb. Inst.* 32(2) (2009) 3223-3230.
19. I. Schoegl, S.R. Newcomb, J.L. Ellzey, *Int. J. Hydrogen Energy* 34 (2009) 5152-5163.
20. S. Zhdanok, L.A. Kennedy, G. Koester, *Combust. Flame* 100 (2) (1995) 221-231.
21. R.S. Dhamrat, J.L. Ellzey, *Combust. Flame* 144 (2006) 698-709.
22. M. Fay, R. Dhamrat, J.L. Ellzey, *Combust. Sci. Technol.* 177 (11) (2005) 2171-2189.
23. M.J. Dixon, I. Schoegl, C.B. Hull, J.L. Ellzey, *Combust. Flame* 154 (2008) 217-231.
24. A. Pastore, E. Mastorakos, *Fuel* 90 (2011) 64-76.
25. S. Yajima, T. Satow, T. Hirai, *J. Nucl. Mater.* 17 (1965) 116–26.
26. C.B. Hull, Master's thesis, The University of Texas at Austin, 2007.
27. C.K. Law, *Combustion Physics*, Cambridge University Press, 2006.
28. M.R. Henneke, J.L. Ellzey, *Combust. Flame* 117 (1999) 832-840.

## **Appendix C: Critical design parameters for counterflow reactor**

The third objective of this ARO-funded project was to computationally investigate the critical design parameters for reforming in the counterflow reactor. This work is described below, and is in preparation for publication.

The counterflow reactor design was proposed analytically [1,2,3] and validated in experimental studies on the reforming of methane [4], propane [5] and heptane [6] to produce syngas. A computational model of the counterflow reactor was developed to study the reaction zone characteristics of rich methane combustion, in which the reactor channels were modeled in two dimensions, and the detailed GRI 2.11 kinetics mechanism was used. The model was validated against experimental results, where the impact of inlet velocity and equivalence ratio operating conditions on combustion zone characteristics was successfully modeled [7].

This study utilized the previously developed computational model to study the impact of geometric scaling on rich methane reforming in the counterflow reactor. Scalability is an important consideration for portable power applications, as well as for large-scale, stationary applications. In either case, reactor scaling may be achieved by changing the geometry of the individual channels or by altering the number of parallel channels [8]. This study focused on geometry at the individual channel scale.

Several studies have examined the effects of geometric scaling on the stability and performance of meso-scale, heat-recirculating combustors [9]. The parameters that have been examined include channel wall thickness and material in Swiss-roll and parallel-channel reactors [10,11,12,13], as well as channel length [14] and channel width [12,15,16,17,18,19]. Kaisare and Vlachos [20] numerically studied the effect of reactor length, wall thickness and reactor opening size on flame stability in micro- and meso-scale channel reactors.

The effect of scaling the counterflow reactor on non-catalytic fuel reforming was the focus of this computational study, where reactor channel length or height were varied from the original dimensions examined in previous experimental [4-6,21] and analytical investigations [3,21]. The impact of scaling on methane reforming was quantified in a number of ways: combustion stability, efficiency of reactant conversion to hydrogen, efficiency of heat recirculation from hot combustion products to incoming cold reactants, and degree of superadiabicity, defined as the ratio of peak to equilibrium temperatures, achieved in the reactor. Computational investigation of reactor operating range and hydrogen conversion provided an efficient means of testing numerous reactor geometries. Quantification of heat recirculation efficiency and degree of superadiabicity provided insights into reactor operation that are not readily measured during experimentation. Heat recirculation efficiency in the counterflow reactor was also compared to that achieved in a porous reactor [22].

## C.1 Numerical method

### Numerical model

The data presented in this study were obtained from simulations performed using the computational fluid dynamics (CFD) code Fluent 14.5. The CFD code solves conservation of mass, energy and species equations and the incompressible Navier-Stokes equations. The conservation of mass is given by

$$\frac{\partial \rho_f}{\partial t} + \nabla \cdot (\rho_f \mathbf{v}) = 0 \quad (\text{C.1})$$

and the conservation of momentum is given by

$$\frac{\partial(\rho_f \mathbf{v})}{\partial t} + \nabla \cdot (\rho_f \mathbf{v} \mathbf{v}) = -\nabla p + \nabla \cdot \bar{\boldsymbol{\tau}} + \mathbf{F} \quad (\text{C.2})$$

where  $\rho_f$  is fluid density,  $\mathbf{v}$  is the velocity vector, and  $p$  is the static pressure. The stress tensor,  $\bar{\boldsymbol{\tau}}$ , and  $\mathbf{F}$  represent volumetric forces including viscous forces. The fluid is approximated by the ideal gas law, thus fluid density is given by  $\rho_f = p/(RT/M_w)$  where  $R$  is the ideal gas constant,  $T$  is temperature and  $M_w$  is the molecular weight of the gas.

Conservation of energy for the fluid phase is given by

$$\frac{\partial(\rho_f E)}{\partial t} + \nabla \cdot (\mathbf{v}(\rho_f E + p)) = \nabla \cdot (k_f \nabla T - \sum_i h_i \mathbf{J}_i) + S_{h,f} \quad (\text{C.3})$$

where  $E = h - p/\rho_f + v^2$  and  $h$  is sensible enthalpy, defined for incompressible fluid as  $h = \sum_i Y_i h_i$  with  $Y_i$  as the mass fraction of species  $i$ . Thermal conductivity is given by  $k$ ,  $\mathbf{J}$  represents Fickian species diffusive flux, and  $S_{h,f}$  is a volumetric source term that includes the heat of chemical reactions.

Conservation of energy for the solid phase is given by

$$\frac{\partial(\rho_s h_s)}{\partial t} = \nabla \cdot (k_s \nabla T) + S_{h,s} \quad (\text{C.4})$$

where  $S_{h,s}$  represents user-defined volumetric heat sources.

Conservation of species is given by

$$\frac{\partial(\rho_f Y_i)}{\partial t} + \nabla \cdot (\rho_f \mathbf{v} Y_i) = -\nabla \cdot \mathbf{J}_i + R_i \quad (\text{C.5})$$

where the net rate of production of species  $i$ ,  $R_i$ , is the sum of Arrhenius reaction rates for  $N$  reactions. Combustion chemistry is modeled using detailed reaction chemistry mechanism GRI 2.11. Further details about the numerical model can be found in [7].

### Model Geometry

Figure C.1a is a schematic of the four-channel reactor used in previous experimental investigations [4-6,21]. Figure C.1b is a schematic of the computational domain of the original reactor geometry, with dimensions of the counterflow reactor used in previous experimental reforming and thermal oxidation studies. The domain is reduced to one half-channel, which lessens the computational load significantly, through the use of symmetry and a user-defined function (UDF). Symmetry in the  $y$ -direction is imposed at the channel center line, and temperature symmetry is imposed by a UDF at the wall center line. External losses are accounted for by radiative wall ends and convective losses from the wall. Therefore, the computational model approximates the reactor as an infinite number of parallel channels.

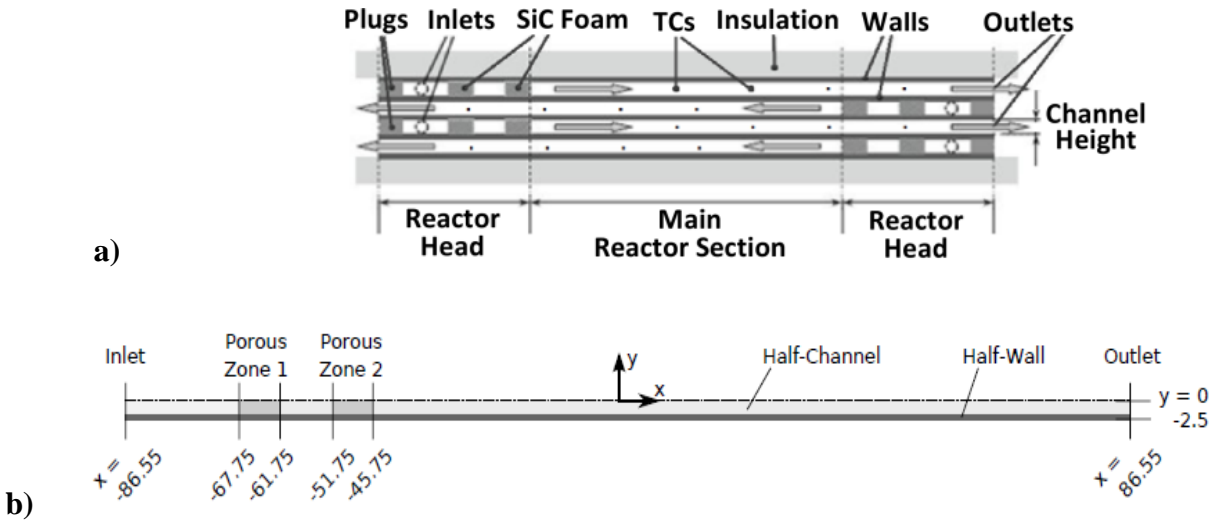


**Figure C.1: (a) A schematic of the four-channel reactor and (b) the computational domain of the original reactor geometry (VR 1.0)**

The reactors modeled in this study are scaled relative to the volume of the original reactor (122 cm<sup>3</sup>) by a volume ratio, defined as

$$\text{Volume Ratio}(VR) = \frac{\text{Volume of scaled reactor}}{\text{Volume of original reactor}} \quad (\text{C.6})$$

where the scaled reactor volume is achieved by varying either channel height or main reactor section length, while maintaining the other dimension at the reference, original reactor value. In addition, geometry is limited by maintaining the original reactor head dimensions, except as channel height is varied, and channel wall thickness is maintained at the original value of 1 mm. Volume ratios of 0.75, 1.0 and 1.25 are investigated, where volume ratio 1.0 (VR 1.0) corresponds to the original reactor design and dimensions. Table C.1 shows the dimensions of each scaled reactor.

**Table C.1: Counterflow reactor dimensions for volume ratios (VR) 0.75, 1.0 and 1.25, obtained by varying channel height or channel length with the other held constant at its reference value**

Volume Ratio (VR)	Reactor ID	Channel height (mm)	Total channel length (mm)
1.0	VR 1.0	4.0	173.1
0.75	VR(h) 0.75	2.7	173.1
1.25	VR(h) 1.25	5.3	173.1
0.75	VR(L) 0.75	4.0	129.8
1.25	VR(L) 1.25	4.0	216.4

### **Solution Approach**

Scaled reactors were modeled in ANSYS ICEM CFD. The initial model grids had axial and transverse spacing equal to that used in Schoegl et al [7]. A base case of each reactor model was run for 20k time steps of size  $2e-5$  seconds at inlet conditions of  $\phi=2.2$  and  $u=125$  cm/s in order to achieve ignition and initial stabilization of the flame front in the main reactor section of the channel. The solution of the base case was then used as an initial solution for each tested equivalence ratio and inlet velocity operating point. Solutions were continued until near-steady state was achieved, where steady state was determined to occur when the flame front velocity within the main section of the reactor model was less than 0.5 mm/s. Flame front location was determined by the location of peak H radical concentration.

After near-steady state was achieved, the mesh for each case was refined in a three phase process. Each mesh was locally refined in regions of high concentrations of specific chemical species, following [7]. This process effectively increased the mesh resolution up to 64-fold around the combustion zone by partitioning quadrilateral elements into four sub-elements. Following each stage of mesh refinement, simulations were continued for a total of 5k additional time steps of size  $1e-5$  seconds. After the third refinement, the spatial discretization solution technique was changed from first-order upwind to second-order upwind, and the final result was

obtained after an additional 3k time steps of size  $1e-5$  s. The Semi-Implicit Method for Pressure Linked Equations (SIMPLE) algorithm was used for pressure-velocity coupling during the transient calculations.

## C.2 Results and Discussion

Results are presented below for each of the five scaled reactors over the range of tested inlet velocities and equivalence ratios. Data include operating conditions where steady state combustion was achieved in the main section of the reactor, as well as heat recirculation efficiency, gas and wall temperature ratios, and hydrogen conversion efficiencies at those steady state points.

### Steady State Combustion

Each of the five reactor geometries were tested over a range of inlet velocities and equivalence ratios to determine which operating points produce a steady state flame front solution in the main section of the reactor channel, which corresponds to stable reactor operating points in experimental studies. Inlet velocity was varied from 50-200 cm/s in increments of 25 cm/s at  $\phi=2.2$ , and equivalence ratio was varied from  $\phi=1.4$ -2.6 in increments of 0.2 at  $u=125$  cm/s. Figure C.2 shows the operating limits within these ranges for the three reactor geometries that were scaled by channel height. Beyond these limits, the steady state flame front solution is either upstream of the main reactor section at the porous media flow straightener, which corresponds to flashback in experimental investigations, or the flame front propagated out of the channel exit, which corresponds to blow-off in experimentation.

In the case of equivalence ratio variation, the computations indicate flashback and blow-off at equivalence ratios below and above the lowest and highest points, respectively, for which steady state solutions are obtained in the main reactor section. When the volume ratio is increased by increasing channel height, the equivalence ratio at which flashback occurs decreases. For VR(h) 0.75, flashback occurred at  $\phi=1.8$ . For VR 1.0 and VR(h) 1.25, flashback occurred at  $\phi=1.6$  and  $\phi=1.4$ , respectively. The results show a shift in stable equivalence ratio range towards stoichiometric as channel height is increased. Nearly all of the tested equivalence ratios are above the flammability limit of  $\phi=1.67$  for methane at inlet conditions, and preheating of reactants is required to achieve the observed extension of flammability limits [23]. Therefore, the operating range results suggest that preheating becomes more effective with decreasing channel height. As channel height increases, axial convection begins to dominate over transverse heat and mass diffusion, where the latter are required for conversion of fuel at the channel centerline.

In the case of inlet velocity variation, the two lower volume ratio reactors (VR(h) 0.75 and VR 1.0) produced steady state flame fronts in the main reactor section over the entire tested inlet

velocity range, while VR(h) 1.25 became unsteady due to blow-off at  $u=150$  cm/s. Therefore the largest volume ratio reactor, VR(h) 1.25, is the only one of the three reactors scaled by height that is limited over the tested inlet velocity range. Blow-off occurred at  $u=150$  cm/s because the reactants were insufficiently preheated to raise the burning velocity to equal the inlet velocity, which is the criterion for steady state operation in the counterflow reactor. Similar results were observed in Oh et al [10] and Norton et al [12], where larger channel widths resulted in lower reaction rates due to slow heat transfer from the wall where ignition starts [7] towards the reactants at the channel centerline. In contrast, smaller separation distances between channel walls produce more localized reaction zones with steeper temperature and composition gradients.

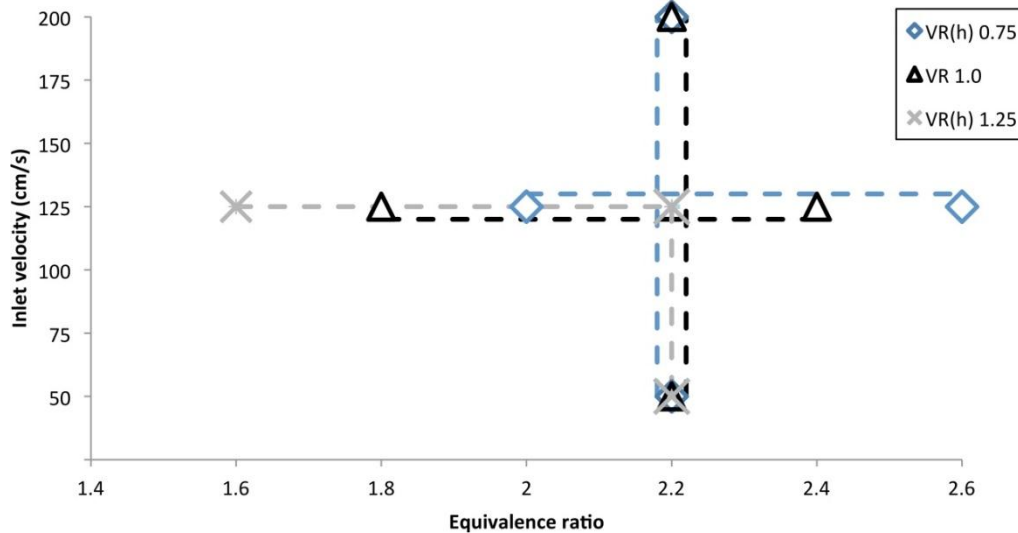


**Figure C.2: Steady state operating limits for counterflow reactors scaled to smaller and larger volume ratios by varying channel height (VR(h) 0.75 and VR(h) 1.25) and original reactor geometry (VR 1.0) over the tested range of inlet velocities,  $u=50-200$  cm/s at  $\phi=2.2$ , and the tested range of equivalence ratios,  $\phi=1.4-2.6$  at  $u=125$  cm/s.**

Figure C.3 shows the steady state operating limits within the ranges of tested inlet velocities and equivalence ratios for the three reactor geometries scaled by channel length. In the case of equivalence ratio variation, flashback occurred at decreasing equivalence ratios as volume ratio increased:  $\phi=1.8$  for VR(L) 0.75,  $\phi=1.6$  for VR 1.0 and  $\phi=1.4$  for VR(L) 1.25. Blow-off occurred at  $\phi=2.4$  for the reactor with the shortest length, VR(L) 0.75, whereas steady state operation was achieved at the upper end of the tested equivalence ratio range for the longer reactors VR 1.0 and VR(L) 1.25. In the case of inlet velocity variation, the two longer reactors, VR(L) 1.25 and VR 1.0, produced steady state solutions throughout the tested range of 50-200 cm/s. The lowest volume ratio reactor with shortest channel length, VR(L) 0.75, had a steady state range of 100-150 cm/s, due to flashback at 75 cm/s and blow-off at 175 cm/s.

The results suggest that steady state range increases with channel length, however VR(L) 0.75 and VR 1.0 produced steady state results throughout the tested inlet velocity range and therefore

the extents of inlet velocity range were not tested. The observed steady state solutions are consistent with experimental observations of the stable operating range. It is likely that there is an optimal channel length for maximum stability range due to the competing effects of heat loss and stabilization space; as channel length increases, surface area and thus heat loss also increase, however there is also increased axial space for the reaction front to stabilize. Since there is no predetermined combustion zone location in the main section of the reactor, the flame front is free to stabilize at the point where the burning velocity equals the local inlet velocity. For example, increasing the equivalence ratio from  $\phi=2.0$  to  $\phi=2.2$  at a fixed inlet velocity results in lower heat release. The flame front will then stabilize further downstream, where the heat recirculation is more significant and the reactants can be further preheated prior to combustion. Likewise, the flame front location will adjust to changes in inlet velocity at a fixed equivalence ratio; the flame front will shift downstream in response to an increase in inlet velocity, where additional heat recirculation will provide sufficient preheating for the burning velocity to equal the inlet velocity. The reactor scaled down by channel length, VR(L) 0.75, has the most limited axial distance within the main section for the reaction front to adjust to changes in operating conditions before blow-off or flashback will occur, thus its stable range is significantly narrower than longer reactors VR 1.0 and VR(L) 1.25.

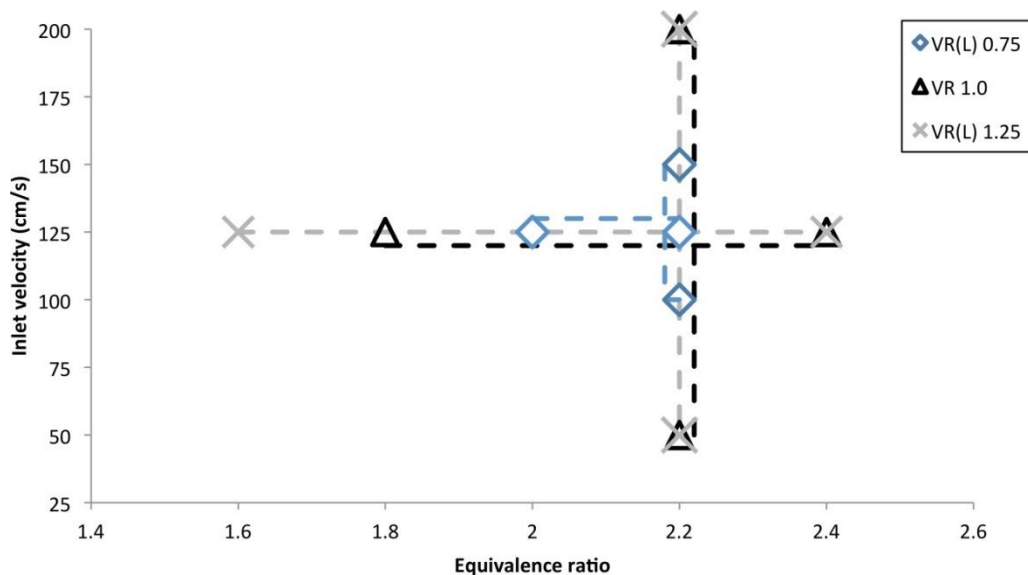


**Figure C.3: Steady state operating limits for counterflow reactors scaled to smaller and larger volume ratios by varying channel length, VR(L) 0.75 and VR(L) 1.25, and original reactor geometry, VR 1.0, over the tested range of inlet velocities,  $u=50-200$  cm/s at  $\phi=2.2$ , and the tested range of equivalence ratios,  $\phi=1.4-2.6$  at  $u=125$  cm/s.**

### Heat Recirculation Efficiency

The counterflow reactor transfers heat by conduction and radiation upstream from hot combustion products in the post-flame region to cold reactants in the preheat region. Heat is also

transferred through the channel walls to the unburned reactants counterflowing in the adjacent channels, thereby preheating the reactants. Figure C.4 shows temperature profiles for gas at the reactor channel centerline and the channel wall, obtained for the original reactor geometry (VR 1.0) at operating conditions of  $\phi=2.2$  and  $u=125$  cm/s. The preheat zone is identified as the region between the channel inlet and the point where wall and gas temperatures are equal. Upstream of this point, the wall temperature exceeds the gas temperature and heat is transferred to the gas. The two sections of porous media flow straighteners (PM) are identified, and the impact of these conductive inserts on increasing the gas temperature can be seen. Downstream of the preheat zone, the reaction zone occurs and gas temperatures exceed wall temperatures. Heat is then transferred from the gas to the wall, where it conducts and radiates upstream and preheats reactants in adjacent channels.

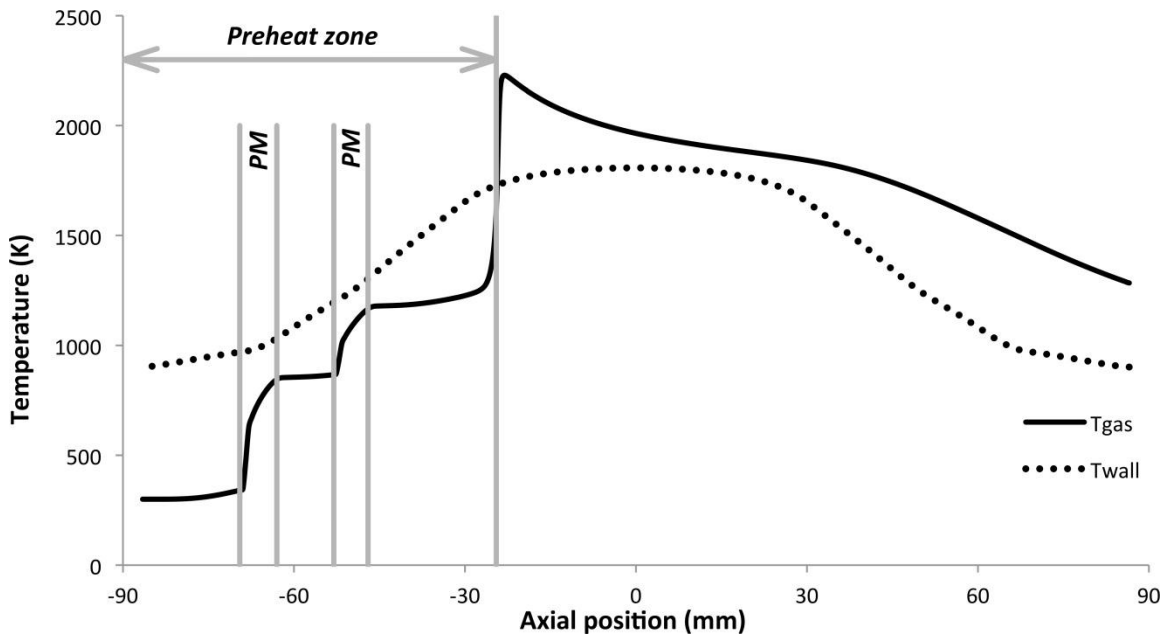


**Figure C.4: Gas ( $T_{\text{gas}}$ ) and wall ( $T_{\text{wall}}$ ) temperature profiles along the axial length of a counterflow reactor channel, obtained from the original reactor geometry (VR 1.0) with inlet conditions of  $\phi=2.2$  and  $u=125$  cm/s. The preheat zone is identified, as well as the locations of the two sections of porous media flow straighteners (PM), the high thermal conductivity of which contributes to preheating the reactants.**

The amount of heat transferred to the reactants in the preheat zone is obtained by integrating the heat flux into the channel upstream of the reaction zone, from the inlet to the point where the gas and solid temperatures are equal and the flux equals zero. Heat recirculation efficiency is a measure of this heat transfer and is defined as

$$\text{Heat recirculation efficiency} = \frac{\text{Heat transfer to reactants}}{\text{Firing rate}} \quad (\text{C.7})$$

where firing rate is calculated based upon the lower heating value of methane.

Figure C.5 shows the calculated heat recirculation efficiency for each of the five scaled reactors as a function of equivalence ratio. All reactors show a decrease in heat recirculation efficiency with increasing equivalence ratio. A significant increase in efficiency is found with decreasing channel height, where the smallest channel height VR(h) 0.75 shows approximately 30% and 26% heat recirculation efficiency at  $\phi=2.0$  and  $\phi=2.2$ , respectively, versus 19% and 18% efficiency produced by the largest channel height VR(h) 1.25. The increase in heat recirculation efficiency with decrease in volume ratio is attributed to the increase in wall surface area for heat transfer per unit of gas volume as channel height decreases. The shift of stable equivalence ratio range towards progressively richer equivalence ratios with decrease in channel height, shown in Figure C.3, is attributed to this increased heat recirculation efficiency; the more effective preheating provided by increased heat recirculation efficiency permits the combustion of progressively richer reactant mixtures.

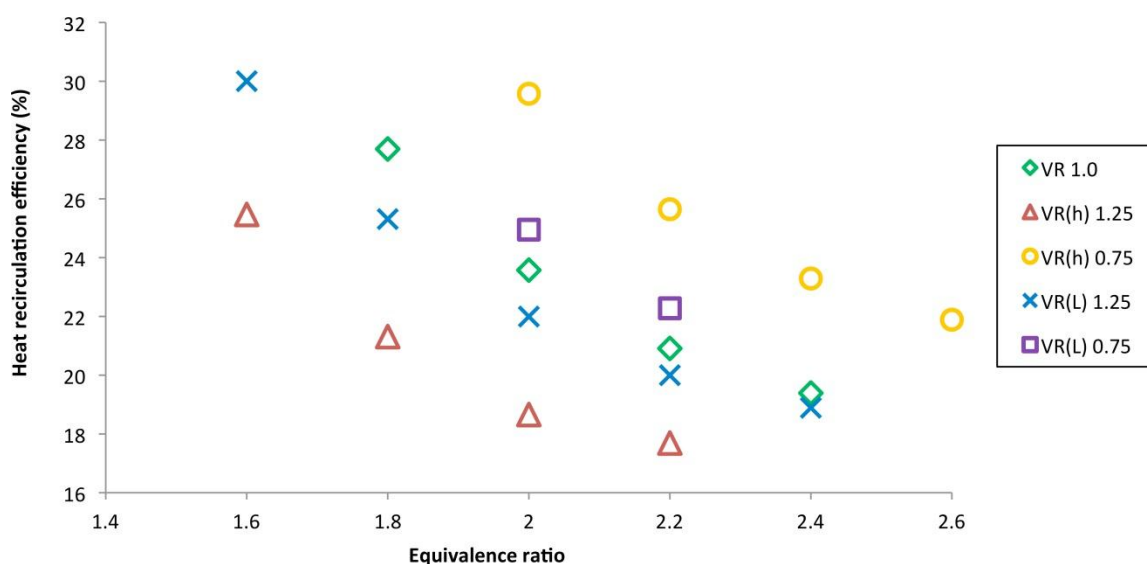


**Figure C.5: Heat recirculation efficiency is shown for each of the scaled reactors, including those scaled by channel height (VR(h) 0.75 and VR(h) 1.25) and those scaled by channel length (VR(L) 0.75 and VR(L) 1.25), as a function of equivalence ratio.**

Heat recirculation efficiency decreases slightly with increasing channel length, where the shortest reactor length VR(L) 0.75 produced efficiencies of 25% and 22% versus 22% and 20% observed for the longest reactor length VR(L) 1.25 at  $\phi=2.0$  and  $\phi=2.2$ . This trend is attributed to greater amounts of heat loss from longer reactors with larger external surface area. Additionally, flame fronts stabilize further downstream with increase in equivalence ratio. This brings the locations of peak gas temperatures in adjacent channels closer to the axial center, which

minimizes heat loss and temperature decrease of hot combustion gases prior to preheating reactants in adjacent channels. Thus the heat recirculation efficiency of the longest reactors, VR(L) 1.25 and VR 1.0, appear to converge with increasing equivalence ratios, where the flame fronts in both reactors are approaching the channel axial length centerlines. The shortest reactor channel length, VR(L) 0.75, has limited equivalence ratio stability range, but the peak reactor temperatures are in close proximity to the preheat zones of adjacent channels at the points where stability is attained.

Figure C.6 shows the calculated heat recirculation efficiency for each of the five scaled reactors as a function of inlet velocity. A decrease in efficiency is observed for all reactors except that with the smallest channel height, VR(h) 0.75, which shows a peak efficiency at  $u=150$  cm/s. The decrease in efficiency exhibited by most reactors is attributed to the decrease in residence time with increasing inlet velocity, which impacts fuel conversion and heat release. A similar trend was observed in Barra et al [22]. The different trend exhibited by VR(h) 0.75 is likewise attributed to fuel conversion efficiency and peak temperatures in this reactor.

As was observed in Figure C.5 for the variation of equivalence ratio, heat recirculation efficiency is observed to increase with decreasing channel height and channel length, with the largest difference observed between VR(h) 0.75 and VR(h) 1.25.

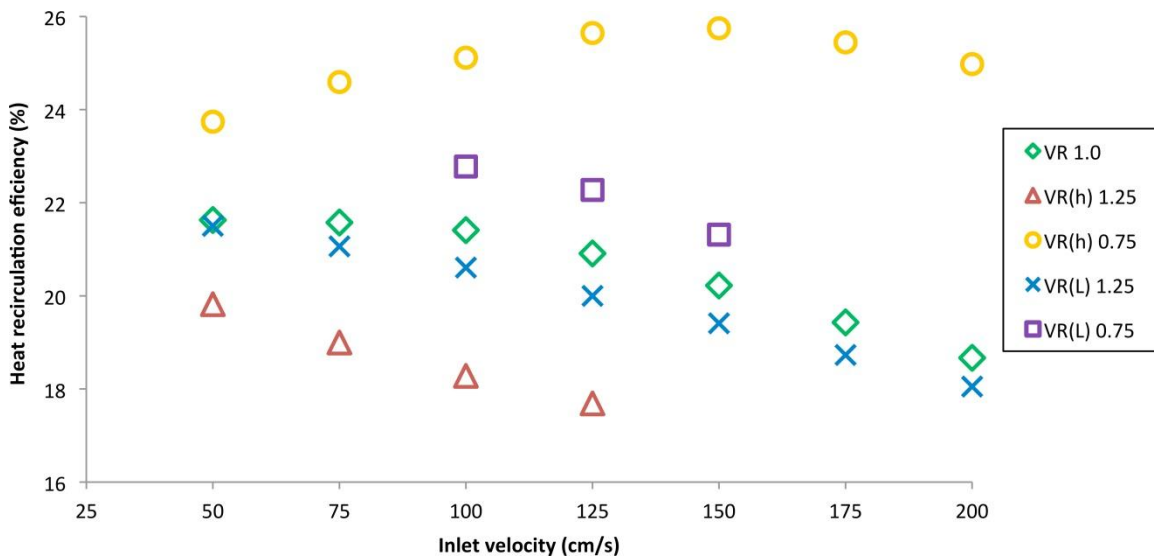


**Figure C.6: Heat recirculation efficiency is shown for each of the scaled reactors, including those scaled by height (VR(h) 0.75 and VR(h) 1.25) and those scaled by length (VR(L) 0.75 and VR(L) 1.25), as a function of inlet velocity.**

## Temperature Ratio

Excess enthalpy reactors recirculate energy to increase the enthalpy of the reaction zone, which permits the combustion of mixtures at equivalence ratios beyond the conventional limits of the inlet mixture. As a result, flame temperatures may exceed the adiabatic flame temperature predicted by equilibrium based upon initial reactant temperature. The extent to which temperatures become superadiabatic depends upon the preheat temperature achieved by the reactants, and therefore the amount of heat recirculated as well as the amount of heat loss from the reactor. Peak reactor temperatures are therefore reflective of the effectiveness of heat recirculation. A temperature ratio is defined as a measure of superadiabaticity, or extent of temperature increase above the adiabatic equilibrium temperature, as

$$\text{Temperature ratio} = \frac{\text{Peak gas or wall temperature}}{\text{Adiabatic equilibrium temperature}} \quad (\text{C.8})$$

Temperature ratio is defined in terms of both peak gas and peak wall temperatures, where the latter is more readily measured during experimentation.

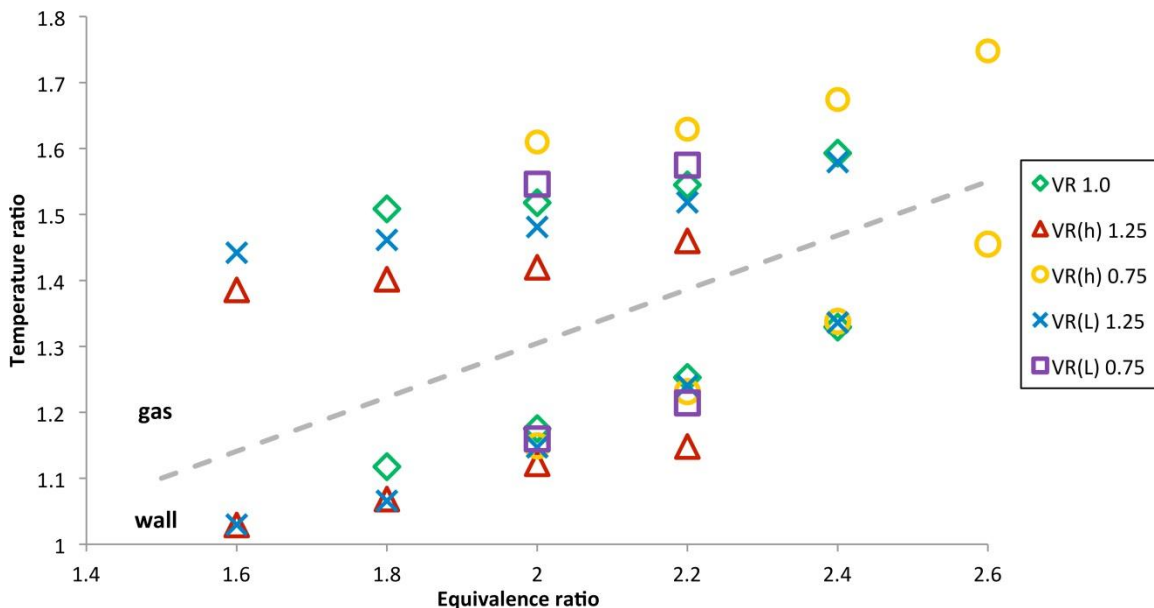


**Figure C.7:** Separated by a dashed line, gas (above) and wall (below) temperature ratios are shown for each of the scaled reactors, including those scaled by height (VR(h) 0.75 and VR(h) 1.25), those scaled by length (VR(L) 0.75 and VR(L) 1.25), and original reactor geometry (VR 1.0), as a function of equivalence ratio.

Figure C.7 shows gas and wall temperature ratios for each of the five scaled reactors as a function of equivalence ratio. All temperature ratios are above unity, indicating superadiabatic peak gas and wall temperatures at all equivalence ratios. Gas temperature ratios are also

significantly higher than wall temperature ratios at all points, where the latter are the temperatures typically measured during experimentation. Both gas and wall temperature ratios increase with equivalence ratio, suggesting that higher levels of preheat, and therefore increasingly superadiabatic conditions, are required to achieve reactor stability at equivalence ratios increasingly above the conventional flammability limit. Gas temperature ratios are highest in the reactors with decreased channel height and length, VR(h) 0.75 and VR(L) 0.75, and lowest in the reactors with increased channel height and length, VR(h) 1.25 and VR(L) 1.25.

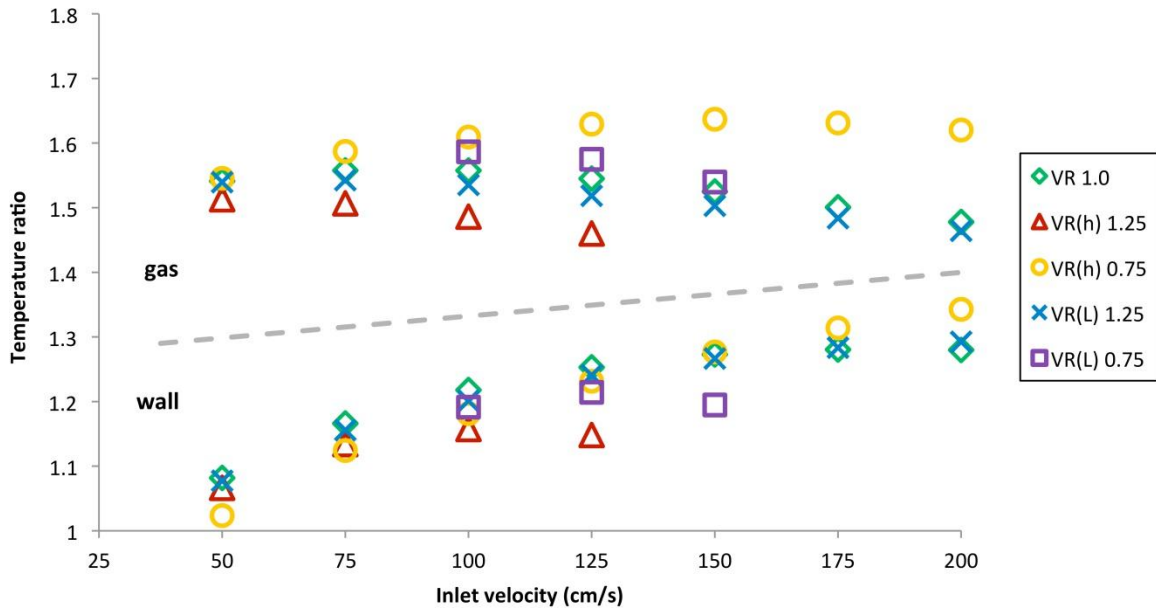


**Figure C.8: Separated by a dashed line, gas (above) and wall (below) temperature ratios are shown for each of the scaled reactors, including those scaled by height (VR(h) 0.75 and VR(h) 1.25), those scaled by length (VR(L) 0.75 and VR(L) 1.25), and original reactor geometry (VR 1.0), as a function of inlet velocity.**

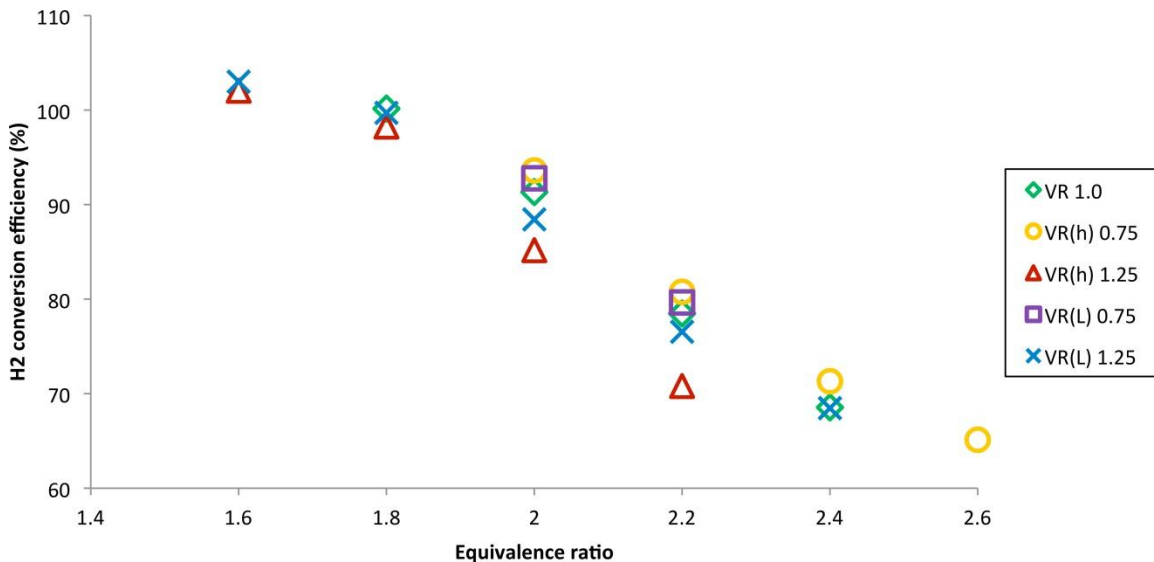
Figure C.8 shows gas and wall temperature ratios for each of the five scaled reactors as a function of inlet velocity. All temperature ratios are above unity, indicating superadiabatic peak gas and wall temperatures at all inlet velocities. Gas temperature ratios are also significantly higher than wall temperature ratios at all points. Gas temperature ratios are highest in the reactors with decreased channel height and length, VR(h) 0.75 and VR(L) 0.75, and lowest in the reactors with increased channel height and length, VR(h) 1.25 and VR(L) 1.25. This correlates with heat recirculation efficiency trends observed in Figure C.6. Gas temperature ratios generally show a slight increase with inlet velocity at the lowest tested inlet velocities, and a decrease with inlet velocity at the highest tested values. This is attributed to a low rate of heat release at the lowest firing rates, where heat losses may have a significant impact on reactor temperatures, and incomplete fuel conversion at the highest firing rates due to decreased residence time.

## Hydrogen Conversion Efficiency

The goal of hydrocarbon reforming is the production of syngas consisting primarily of carbon monoxide and hydrogen, of which hydrogen is often the higher valued product. Hydrocarbon reforming is carried out at rich conditions, where partial oxidation will occur due to oxidizer deficiency of the reactants. Equilibrium predicts an increase in hydrogen product concentration with increasing reactant equivalence ratio. The equilibrium yield is not necessarily achievable in a practical reactor, however, due to limited residence time for reaction. Hydrogen production in the counterflow reactor is defined in terms of hydrogen conversion efficiency as

$$H_2 \text{ conversion efficiency} = \frac{H_2 \text{ product concentration}}{H_2 \text{ equilibrium concentration}} \quad (\text{C.9})$$

where thermodynamic equilibrium provides a theoretical maximum concentration, and hydrogen conversion efficiency quantifies the actual hydrogen yield relative to this value.



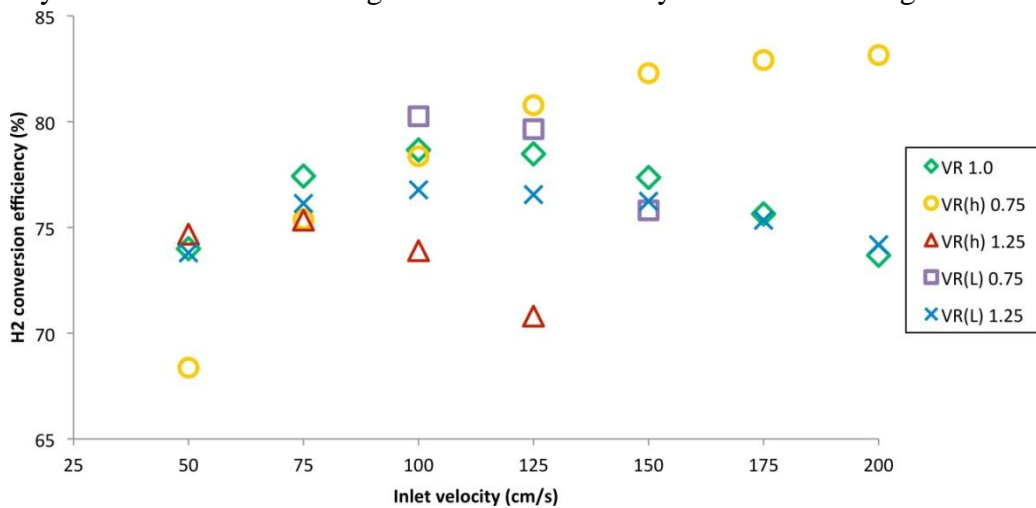
**Figure C.9: Hydrogen conversion efficiencies are shown for each of the scaled reactors, including those scaled by height (VR(h) 0.75 and VR(h) 1.25) and those scaled by length (VR(L) 0.75 and VR(L) 1.25), as a function of equivalence ratio.**

Figure C.9 shows hydrogen conversion efficiencies for each of the five scaled reactors as a function of equivalence ratio. All reactors show a decrease in conversion efficiency with increasing equivalence ratio. The results for the original reactor geometry, VR 1.0, are in agreement with experiment findings that hydrogen conversion efficiency, as defined above, decreases from approximately 95% to 75% as equivalence ratio is increased from  $\phi=1.8$  to  $\phi=2.4$  [4]. Computational reactor conversion efficiencies exceed 100% at the lowest tested equivalence ratios, where hydrogen product concentration exceeds the yield predicted by equilibrium for reactants at 300K. Equilibrium predicts a shift in primary hydrogen-containing products from

water towards diatomic hydrogen as reactant temperature is increased. Since reactants are preheated within the counterflow reactor, hydrogen production in excess of that predicted by equilibrium for 300K products, and therefore conversion efficiencies above 100%, are reasonable.

Trends observed in hydrogen conversion efficiencies are similar to those observed in temperature ratio and heat recirculation efficiency variation with height and length scaling: hydrogen conversion efficiencies are slightly higher in the reactors with decreased channel height and length, VR(h) 0.75 and VR(L) 0.75, as compared to original reactor geometry, VR 1.0, and lowest in the reactors with increased channel height and length, VR(h) 1.25 and VR(L) 1.25. Overall, however, there is little difference in hydrogen conversion efficiency between the reactors at most tested equivalence ratios. This suggests that heat recirculation and reactant preheating are necessary for flammability limit extension, but do not significantly impact product composition in many cases. This finding is in agreement with a study of burner-stabilized flames of preheated, premixed methane and air by Smith et al [23]. The lack of significant impact of reactor length on product composition is also suggested by the previous findings of Kaisare et al [20], who concluded that burner length is unlikely to impact reactor operation significantly because homogeneous combustion is largely localized.

Figure C.10 shows hydrogen conversion efficiencies for each of the five scaled reactors as a function of inlet velocity. All reactors except for VR(h) 0.75 show an increase in conversion efficiency with inlet velocity at low firing rates, and a decrease with inlet velocity at high firing rates. This suggests that optimal operation occurs around the middle of the tested inlet velocity range, where firing rate is sufficiently high to dominate over external losses but not high enough to limit conversion by decreased residence time. The results for VR(h) 0.75 suggest that this reactor may be able to stabilize at higher inlet velocities beyond the tested range.



**Figure C.10: Hydrogen conversion efficiencies are shown for each of the scaled reactors, including those scaled by height (VR(h) 0.75 and VR(h) 1.25) and those scaled by length (VR(L) 0.75 and VR(L) 1.25), as a function of inlet velocity.**

### C.3 Conclusions

A computational study was undertaken to determine the effect of geometric scale on fuel reforming in the meso-scale parallel-plate counterflow reactor. Length and height of the reactor channels were scaled relative to the original dimensions of the counterflow reactor that has been used in previous analytical and experimental investigations. Results were quantified in terms of steady state reactor operation, heat recirculation efficiency, temperature ratio, and hydrogen conversion efficiency.

Reactor operating range was found to be strongly impacted by channel scaling. Decreasing channel height resulted in a shift in stable operating range towards higher equivalence ratios. Decreasing channel length resulted in a significant narrowing of the stable equivalence ratio and inlet velocity ranges. Most stable operating points were above the conventional rich flammability limit and adiabatic flame speed of methane and air combustion based upon inlet conditions, which highlights the importance of heat recirculation in achieving operation of the counterflow reformer at these conditions.

Heat recirculation efficiency and temperature ratios were found to be significantly higher for reactors with decreased channel height. These findings indicate more effective heat recirculation with smaller channel height, where channel wall surface area-to-gas volume ratio is increased and the transverse distance for mass and heat diffusion is reduced. Channel length showed a less significant impact on heat recirculation, with shorter channel lengths producing slightly higher heat recirculation efficiencies and temperature ratios than longer lengths.

Hydrogen conversion efficiency decreased with increasing equivalence ratio for all reactors, with slightly higher conversion efficiencies found for smaller channel heights and lengths. Hydrogen conversion efficiency initially increased with inlet velocity at the lowest tested firing rates, and decreased at the highest tested inlet velocities, suggesting that an optimal firing rate exists.

Scaled down reactors were achieved by decreasing reactor channel height and length, although the latter resulted in a significantly narrowed stable range. The results of this study highlight the effectiveness of small scale reactor channels in achieving heat recirculation and significantly superadiabatic temperatures. These, in turn, permit the effective extension of flammability limits to stable operation at rich equivalence ratios. While increasing heat recirculation may be required to significantly extend the stable operating range, the results of this study suggest that superadiabatic temperatures serve to extend the flammable range of reactor operating points but otherwise do not strongly impact hydrogen conversion efficiencies.

## C.4 References

1. R.V. Fursenko, S.S. Minaev, and V.S. Babkin, *Combust. Explos. Shock Waves* 37(5) (2001) 493- 500.
2. Y. Ju, C.W. Choi, *Combust. Flame* 133 (2003) 483-493.
3. I. Schoegl, J.L. Ellzey, *Combust. Flame* 151(1-2) (2007) 142-159.
4. I. Schoegl, J.L. Ellzey, *Proc. Comb. Inst.* 32(2) (2009) 3223-3230.
5. I. Schoegl, S.R. Newcomb, J.L. Ellzey, *Int. J. Hydrogen Energy* 34 (2009) 5152-5163.
6. E.L. Belmont, S.M. Solomon, J.L. Ellzey, *Combust. Flame* 159 (2012) 3624–3631.
7. I.M. Schoegl, J.L. Ellzey, *Combust. Sci. Tech.* 182(10) (2010) 1413-1428.
8. M.S. Mettler, G.D. Stefanidis, D.G. Vlachos, *Ind. Eng. Chem. Res.* 49 (2010) 10942-10955.
9. V. Shirsat, A.K. Gupta, *Applied Energy* 88 (2001) 4294-4309.
10. H. Oh, H. Huh, J. Ahn, P. Ronney, 4th International energy conversion engineering conference and exhibit, San Diego, CA (2006).
11. M. Lee, S. Cho, B. Choi, N. Kim, *Appl. Therm. Eng.* 30 (2010) 2227–2235.
12. D.G. Norton, D.G. Vlachos, *Chem. Eng. Sci.* 58 (2003) 4871–4882.
13. D.G. Norton, D.G. Vlachos, *Combust. Flame* 138 (2004) 97–107.
14. V. Vijayan, A.K. Gupta, 46th AIAA/ASME/SAE/ASEE Conference, Nashville, TN (2010).
15. G. Pizza, C.E. Frouzakis, J. Mantzaras, A.G. Tomboulides, K. Boulouchos, *Combust. Flame* 152 (2008) 433–450.
16. G. Pizza, C.E. Frouzakis, J. Mantzaras, A.G. Tomboulides, K. Boulouchos, *Combust. Flame* 155 (2008) 2–20.
17. J. Daou, M. Matalon, *Combust. Flame* 128(4) (2002) 321-339.
18. J. Li, S.K. Chou, W.M. Yang, Z.W. Li, *Chem. Eng. Journal* 150 (2009) 213–222.
19. M.J. Lee, S.M. Cho, B.I. Choi, N.I. Kim, *Appl. Thermal Eng.* 30 (2010) 2227-2235.
20. N.S. Kaisare, D.G. Vlachos, *Catalysis Today* 120 (2007) 96–106.
21. E.L. Belmont, I. Schoegl, J.L. Ellzey, *Proc. Combust. Inst.* 34 (2013) 3361–3367.
22. A.J. Barra, J.L. Ellzey, *Combust. Flame* 137 (2004) 230–241.
23. C.H. Smith, D.I. Pineda, J.L. Ellzey, *Combust. Flame* 160(3) (2013) 557-564.

## Appendix D: Operation of the counterflow reactor at lean conditions

Although the focus of the ARO project was to investigate conversion of rich mixtures, additional funding was available to explore other aspects of the counterflow reactor. The work reported in this section establishes that the reactor may also be an effective lean combustor for gaseous and liquid fuels. Analytical modeling indicates the mode of stabilization of lean flames in the counterflow reactor. This work has been published as *E.L. Belmont, I. Schoegl, J.L. Ellzey, Proc. Combust. Inst. 34 (2013) 3361–3367*, and a second publication entitled “Lean heptane and propane combustion in a non-catalytic parallel-plate counterflow reactor” has been accepted for publication in *Combustion and Flame*.

The use of small scale combustors in conjunction with mechanical or electrical conversion devices, such as microturbines or thermoelectrics, has been proposed to address the increasing need for portable power [1-3]. Lean reactant mixtures are favorable because they can permit increased levels of fuel conversion and thermal efficiencies as compared to reactant mixtures nearer to stoichiometric. In order to achieve a given firing rate, however, increased volumetric throughput is required as reactants become progressively leaner. Therefore, the optimal equivalence ratio for combustor operation is dependent upon the application. In order for a combustor to be widely applicable, a broad operating range is desirable.

Heat recirculation can be used to extend conventional lean flammability limits and increase burning speed by increasing the enthalpy in the reaction zone above that of adiabatic conditions. Various heat-recirculating lean combustor designs have been proposed and studied, and all operate on the principal of transferring heat through a solid. In some cases, the combustor consists of a solid matrix, such as a reticulated foam or packed bed of spheres [4-8]. In others it consists of parallel channels [9], such as the counterflow reactor used in this study [10]. Theoretical analyses and experimental studies of channel reactors have shown that superadiabatic burning velocities and broadened flammability limits can be achieved [11-15].

Other studies of the counterflow reactor have demonstrated its ability to convert fuel-rich reactants of methane [16], propane [17] and heptane [18] to hydrogen-rich syngas. The studies presented here used the same counterflow reactor for the study of fuel-lean mixtures of methane, as well as increasingly complex fuels: propane and heptane. The latter, being a liquid fuel, has importance as a single component surrogate for logistical fuels [19]. Furthermore, the demonstration of fuel-lean liquid combustion in the counterflow reactor is an important demonstration of its fuel-flexibility for field applications because liquid fuels are generally safer and easier to transport than gaseous fuels.

Counterflow combustor stability and emissions measurements of carbon monoxide (CO), nitrogen oxides (NO<sub>x</sub>) and unburned hydrocarbons (UHCs) were analyzed in this study for lean

operation on propane and heptane. Stability was compared for reactor operation in the lean and rich regimes for both fuels. Reactor channel wall temperatures were compared to adiabatic equilibrium temperatures to determine superadiabaticity. The results of lean methane, propane and heptane combustion in the counterflow reactor were examined to understand the influence of superadiabatic operation on operating range and emissions.

### D.1 Analytical modeling of lean combustion in the counterflow reactor

An analytical model was developed by Schoegl and Ellzey [10] to investigate the operating principle of the counterflow reactor and obtain qualitative predictions of its behavior in response to changes in operating conditions. A complete description of the model can be found in [10] where it was developed for analysis of the counterflow reactor as a fuel reformer. A summary of the model and description of its recalibration for counterflow reactor operation on lean methane/air reactants is described below.

The purpose of the one-dimensional model is to provide insight into the general performance of the counterflow reactor. The model assumes constant thermophysical properties, and combustion is modeled using activation energy asymptotics. Radiative heat losses are included through a boundary condition in the wall temperature solution. The model solves for non-dimensional wall temperature ( $T_w$ ) and gas temperature ( $T_i$ ) along a normalized  $x$  coordinate. The location of the reaction zone is determined indirectly to be where the local reaction rate produces a burning speed that is equal to the inlet velocity, which is the condition for stability. Operating conditions are specified by equivalence ratio, inlet temperature  $To$ , and ambient temperature  $T_\infty$ . Properties of the reactor are specified using non-dimensional parameters which can be found in [10].

The gas temperatures in two adjacent channels are coupled by heat transfer through a common conducting wall. Equation D.1 gives the normalized steady-state energy conservation equations and includes conduction and convection, transport, external losses and chemical reactions, given by

$$\frac{d^2 T_w}{dx^2} = \frac{\mu}{\kappa \epsilon^2} \left[ (1 + \chi) T_w - \frac{1}{2} (T_1 + T_2) - \chi T_\infty \right] \quad (\text{D.1a})$$

$$\frac{d^2 T_i}{dx^2} = \pm \frac{\mu}{\epsilon} \frac{dT_i}{dx} + \frac{\mu}{\epsilon^2} (T_i - T_w) + \frac{T_{ad} - T_\infty}{\epsilon^2} w_i \quad (\text{D.1b})$$

where indices  $i = 1, 2$  denote individual channels and  $T_{ad}$  is the normalized adiabatic flame temperature. Equation D.2 is the species conservation equation which includes diffusion, transport and reactions, and gives the concentration of the limiting reactant species  $y_i$  as

$$\frac{1}{Le} \frac{d^2 y_i}{dx^2} = \pm \frac{u}{\epsilon} \frac{dy_i}{dx} - \frac{1}{\epsilon^2} w_i \quad (\text{D.2})$$

where  $Le$  is the Lewis number and  $u$  is the inlet velocity non-dimensionalized by the adiabatic flame speed of the reference case. Equation D.3 represents the reaction terms  $w_i$ , which are modeled as point sources using activation energy asymptotics [20] by

$$w_i \approx \epsilon \delta(x - x_{c,i}) \exp\left(\frac{\beta(T_i - T_{ad})}{2T_i/T_{ad}}\right) \quad (\text{D.3})$$

where  $\delta(x - x_{c,i})$  are Dirac delta functions at the combustion locations  $x_{c,i}$ . The normalized activation energy  $\beta$  is equal to  $Ze/\gamma$ , where the Zeldovich number  $Ze$  is given by  $E'_a \Delta T'_{ad} / R' T'^2_{ad}$ , the prime (') denotes a dimensional quantity,  $E'_a$  is the activation energy,  $\Delta T'_{ad}$  is the adiabatic temperature rise of a mixture over the unburned mixture  $T'_u$ , and  $R'$  is the universal gas constant. The scaling factor  $\gamma$  is equal to  $\Delta T'_{ad} / T'_{ref}$  where  $T'_{ref}$  is the adiabatic equilibrium temperature of the reference case.

Chemical reactions are modeled using single-step, first-order, irreversible Arrhenius kinetics. The activation energy is calibrated for lean methane/air mixtures using laminar flame speeds for various preheating levels at the equivalence ratios of interest calculated with Cantera [21] and GRI 3.0 [22]. Adiabatic flame temperature and flame speed at the reference condition  $\phi = 0.5$  and  $T'_o = 177.0$  °C are used for the non-dimensionalization of the model. Equation D.4 is utilized to obtain the activation energy by fitting  $\beta$  at each equivalence ratio

$$|u_i| = \exp\left(\frac{\beta(T_{c,i} - T_{ad})}{2T_{c,i}/T_{ad}}\right) \quad (\text{D.4})$$

where  $T_{c,i}$  are adiabatic flame temperatures normalized by the reference temperature. The normalized adiabatic flame temperature  $T_{ad}$  is equal to 1 at  $\phi = 0.50$ ; at other equivalence ratios, it is the adiabatic flame temperature resulting in a mass flux equal to the reference case in detailed simulations, which matches flame speeds within the context of the constant density approximation used for this model. Table D.1 gives the conditions resulting in constant mass flux and the resultant values for the calibrated activation energies.

Due to the simplifications used in the analytical model, its use is limited to qualitative predictions of reactor behavior. It is, however, able to illustrate the stabilization mechanism of the reactor and the trends of temperature and reaction zone location in response to variations in equivalence ratio and inlet velocity.

**Table D.1: Calibrated activation energies derived from calculated temperatures and flame speeds**

$\phi$	$T'_u$ (°C)	$T'_{ad}$ (°C)	$\Delta T'_{ad}$ (°C)	$u'$ (cm/s)	$E'_a$ (kJ/mol)
0.42	316	1285	696	20.2	249.7
0.44	281	1295	741	19.1	247.2
0.46	247	1305	786	17.9	244.2

## D.2 Experimental method

### Experimental Apparatus

Figure D.1 shows the counterflow reactor, which is the same design used in previous reforming studies [16-18]. It contains four 4 mm high parallel channels constructed of 1 mm thick silicon carbide (SiC) walls. The reactor is 17.3 cm long, with a 91.5 mm long main section and two 40.8 mm long reactor heads. Inlets, outlets, end plugs which prevent the mixing of combustion products and reactants, and two 6.4 mm wide sections of SiC porous foam which act as flow straighteners and flame arresters are located in the reactor heads. Two alumina walls spaced 33.6 mm apart enclose the channels. B-type thermocouples (TCs) are inserted into the channels and sit flush with the channel wall in order to prevent flame holding. Premixed fuel and air are provided to the reactor using mass flow controllers for methane, propane and air, and a pump for heptane. Heptane is vaporized prior to entering the reactor. A detailed description of the heptane vaporization system used in this study is available in Belmont et al. [18].

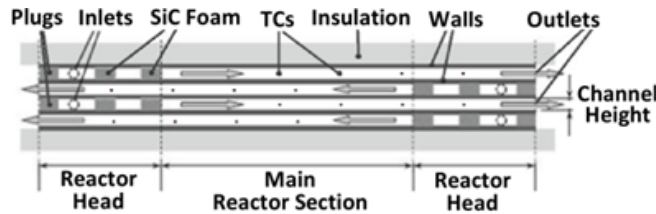


**Figure D.1: Four-channel counterflow reactor with dimensions and internal components indicated**

Concentrations of carbon monoxide (CO), nitrogen oxides (NO<sub>x</sub>), and unburned hydrocarbons (UHCs) were measured in the reactor exhaust using Rosemount Analytical analyzers. Samples were drawn through an uncooled quartz probe with a 2 mm inner diameter and inert tubing, and dried before analysis. A previous study [17] showed slightly lower product species concentrations from outside channels, and minimal variation of composition within a single channel except near the alumina walls. In consideration of these findings, exhaust samples in this study were taken from the center channels at the middle of the channel exit. Therefore, the data produced in this study is expected to be representative of interior channels in scaled up reactors.

## **Experimental Method**

The start-up procedure began by burning a near-stoichiometric mixture of the fuel of interest at the reactor outlets at an inlet velocity of 50 cm/s. The reaction fronts propagated upstream in the channels once the reactor heads had warmed sufficiently, and stabilized downstream of the porous SiC flow straighteners. Operating conditions were then gradually adjusted to the reference conditions for each fuel, and were maintained at those values until temperatures stabilized. Reference conditions for methane were  $\phi = 0.44$  and  $u = 125$  cm/s, and reference conditions for propane and heptane were  $\phi = 0.41$  and  $u = 125$  cm/s.

The warm-up phase took approximately 45 minutes. Experiments included the determination of stable operating conditions and the exhaust gas concentrations of CO, NO<sub>x</sub> and UHCs for each fuel over a range of inlet velocities and equivalence ratios. Test conditions were considered stable if combustion was sustained in the main reactor section for ten minutes at constant temperatures. Reactor wall temperatures were monitored in each of the four channels throughout the experiments. Gas temperatures were not measured directly due to the tendency of thermocouples inserted into the channel to act as flame holders. Peak wall temperatures were recorded at stable reactor conditions and showed less than  $\pm 5^\circ\text{C}$  variation during that time and while exhaust gas samples were taken. Reactor temperatures were limited to less than  $1300^\circ\text{C}$  in order to avoid damage to the reactor.

Following the warm-up phase, equivalence ratio or inlet velocity was adjusted to the desired test values. Inlet velocity was specified at standard conditions of  $25^\circ\text{C}$  and 1 atm. Emissions results were obtained over a range of inlet velocities with equivalence ratio held constant at  $\phi = 0.44$  for methane and  $\phi = 0.41$  for propane and heptane, and over a range of equivalence ratios with inlet velocity held constant at 125 cm/s. Emissions concentrations in parts per million (ppm) are reported as measured on a dry basis.

Each operating point was tested twice. Total uncertainty was calculated at each point as the root-sum-square of the contributing uncertainties. The uncertainty of emissions results is due to repeatability of measurements as calculated using a student-t distribution, the calibration gases and the analyzers. Average uncertainties of CO, NO<sub>x</sub> and UHC measurements for methane, propane and heptane are  $\pm 10$ , 2 and 16,  $\pm 13$ , 2 and 16 ppm and  $\pm 28$ , 2 and 1 ppm, respectively. Inlet velocity uncertainty is due to uncertainties of the mass flow controllers for air, methane and propane, the pump for heptane, and the channel cross-sectional area. Equivalence ratio uncertainty is due to contributions from the flow controllers and pump. Average uncertainties of inlet velocity and equivalence ratio are  $\pm 10$  cm/s and  $\pm 0.03$  for methane and propane, and are  $\pm 10$  cm/s and  $\pm 0.04$  for heptane. Temperature uncertainty is attributed to contributions from repeatability of measurements, the thermocouples, and the data acquisition system. Average

temperature uncertainties for methane, propane and heptane are estimated to be  $\pm 12^\circ\text{C}$ ,  $\pm 16^\circ\text{C}$  and  $\pm 20^\circ\text{C}$ , respectively.

### D.3 Results and Discussion

#### D.3.1 Analytical model results

Equivalence ratio and inlet velocity can be changed independently while stability is maintained within the reactor. There are no predetermined flame stabilization points within the channel; therefore the combustion zone freely adjusts to a new position within the channel following a change in equivalence ratio or inlet velocity. The combustion zone moves to a position where sufficient heat is gained from the adjacent channel and reactants are preheated to the point where the burning velocity equals the inlet velocity, and stability is maintained.

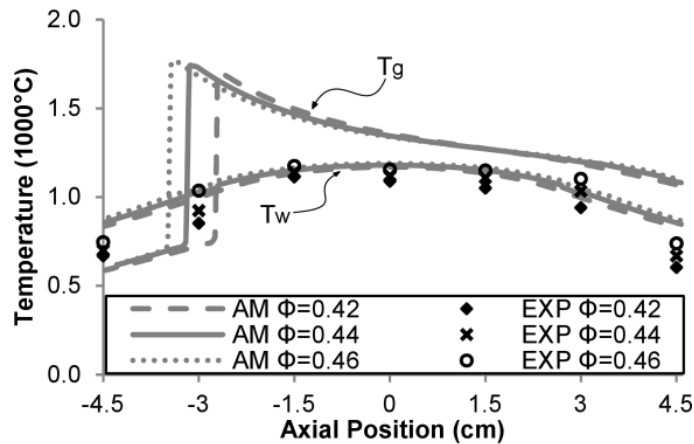


**Figure D.2: Analytical model (AM) gas ( $T_g$ ) and wall ( $T_w$ ) temperatures and experimental (EXP) temperatures measured along axial position in channel for varying  $\phi$  and  $u = 125$  cm/s**

Figure D.2 shows the results of the analytical model for gas and wall temperature profiles for varying equivalence ratio from 0.42 to 0.46 with inlet velocity held constant at 125 cm/s, as well as experimental temperature measurements taken along the axial length of a reactor channel while operating at these conditions, normalized by axial position and overlaid onto the analytical domain. Figure D.3 shows the results of the model and experimental measurements for varying inlet velocity from 75 to 175 cm/s with equivalence ratio held constant at 0.44.

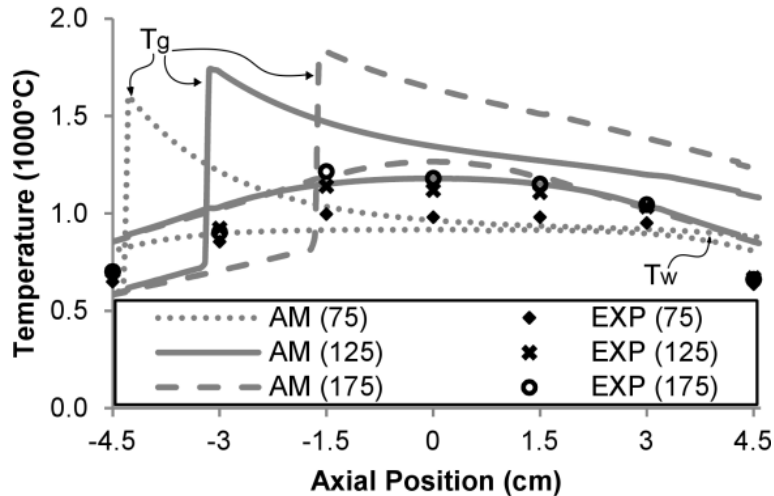


**Figure D.3: Analytical model (AM) gas ( $T_g$ ) and wall ( $T_w$ ) temperatures and experimental (EXP) temperatures measured along axial position in channel for varying  $u$  and  $\phi = 0.44$**

In both cases, the inlet temperature was specified at 577 °C to account for preheating that occurs in the reactor heads. The combustion zone is identified by a sharp increase in gas temperature, while the wall temperature shows a broader profile. The combustion zone adjusts its location towards the center of the reactor following a decrease of  $\phi$  or an increase in  $u$  in Figures D.2 and D.3, respectively. For increasing  $\phi$  (at fixed  $u$ ), the temperature of the flame increases and less preheat is required for the mixture to react and so the flame stabilizes nearer the entrance than for the cases at lower  $\phi$  which require greater preheating (Fig. D.2). For increasing  $u$  (at fixed  $\phi$ ), the reactants travel further into the channel before reaching the critical temperature for combustion (Fig. D.3). Through this adjustment in combustion zone location a burning velocity is attained that equals the inlet velocity.

Wall temperatures also respond to changes in  $\phi$  or  $u$ , both in magnitude and broadness of temperature profile. As  $\phi$  is increased (Fig. D.2) or  $u$  is decreased (Fig. D.3) and the combustion zone shifts upstream, hot products flow over the remaining length of the channel. This condition, as well as conduction through the wall, results in the broad profile predicted by the model. Similarly, as  $\phi$  is decreased or  $u$  is increased and the reaction zone shifts towards the center of the reactor, the central portion of the wall receives more heat and the peak temperature zone in the wall is narrower. Experimental temperature measurements are in qualitative agreement with the results of the analytical model in terms of relative values at the tested operating points.

While the analytical results can only be interpreted qualitatively due to simplifications in the model, they do accurately capture temperature trends and the general conditions under which flashback and blowoff occur, which are at high  $\phi$ -low  $u$  and low  $\phi$ -high  $u$ , respectively. The results of this study can also be compared to a previous study in which the counterflow reactor was operated as a fuel reformer, and the analytical model was used to predict its behavior under

fuel rich conditions [10]. In that study the model similarly predicted changes in combustion zone location in response to changes in  $\phi$  and  $u$ . In the case of fuel rich conditions the combustion zone migrated downstream for increases in  $u$ , as in this study. However, the zone migrated downstream for increases in  $\phi$  because more preheating is required to attain the same peak reaction temperature as a rich mixture becomes progressively richer, analogous to the case for a lean mixture becoming progressively leaner. Therefore the model indicates that the stabilization method for rich and lean mixtures in the counterflow reactor is similar.

### **D.3.2 Experimental results**

#### **Operating Range**

##### **Methane**

Figure D.4 shows the stable operating range of the reactor operating on methane/air reactants in terms of inlet velocity and both standard and normalized equivalence ratio [23]. The combustion process becomes unstable due to either flashback, in which the reaction front propagates upstream past a section of porous flow straightener, blowoff, in which the reaction front propagates out of the outlet of the reactor channel, or extinction. In addition to the data presented in this paper for operation in the lean regime, data from an earlier study [16] on rich methane/air mixtures is also shown. The stable operating points on both the rich and lean sides are beyond the conventional flammability limits.

In terms of standard equivalence ratio, the stable operating range on the lean side is considerably narrower than that on the rich side. Stability is strongly influenced by the temperature of the products and the resultant preheating of the reactants in the neighboring channel. It is well known that in comparison to the rich side of stoichiometric, the temperature of the products changes more significantly with standard equivalence ratio on the lean side resulting in a smaller range of stable conditions. Due to the asymmetry inherent in the standard equivalence ratio definition, the stability range is also presented in terms of normalized equivalence ratio. In normalized form, the width of the stable range in the rich regime is approximately 60% broader than the lean, which is attributed to differences in chemical kinetics between the two regimes.

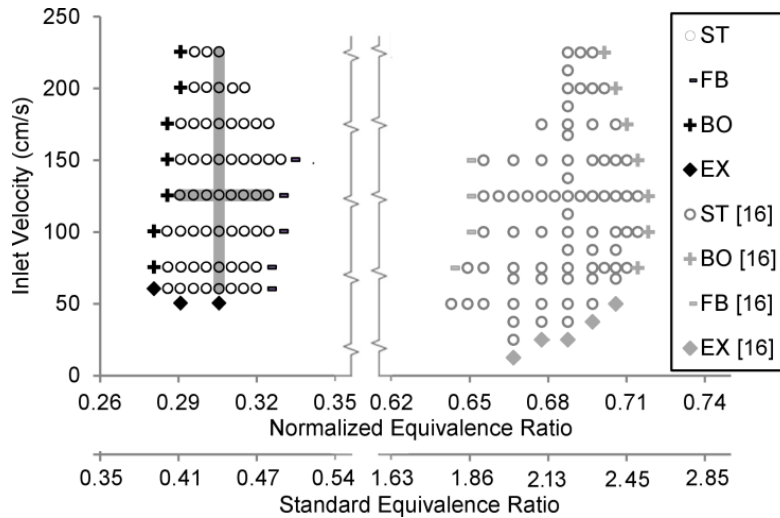


**Figure D.4: Stability map for counterflow reactor operating on lean (this study) and rich ([16]) methane/air reactants, with both stable (ST) and unstable points due to flashback (FB), blowoff (BO) and extinction (EX) shown as a function of inlet velocity and both standard and normalized equivalence ratios**

Propane

Figure D.5 is a stability plot for counterflow reactor operation on propane/air reactants, where operating conditions are defined in terms of inlet velocity and both standard and normalized equivalence ratio. Normalized equivalence ratio, defined as  $\phi/(1+\phi)$ , permits direct comparison of rich and lean operating regimes because it compensates for the inherent asymmetry in the definition of standard equivalence ratio [23].

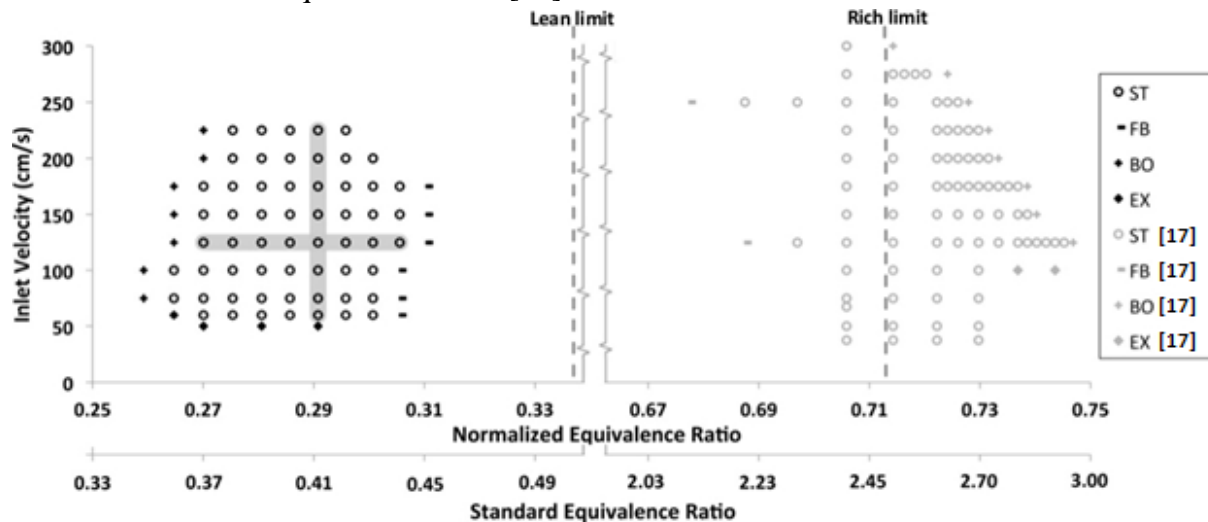


**Figure D.5: Stability map for counterflow reactor operation on lean and rich [17] propane/air reactants, with stable (ST) and unstable points due to flashback (FB), blow-off (BO) and extinction (EX) shown as a function of inlet velocity and both standard and normalized equivalence ratios. Lean and rich flammability limits for propane/air reactants at inlet conditions are indicated.**

The conditions where the reactor operates stably, as well as conditions where operation becomes unstable, are shown. Combustor instability can occur as flashback, in which the reaction front propagates upstream past a section of porous flow straightener; blow-off, in which the reaction front propagates out of the outlet of the reactor channel; or extinction, in which the rate of heat loss exceeds the rate of heat release and combustion is not sustained. In addition to stability data acquired for lean combustor operation, previously obtained data for reactor operation on fuel-rich mixtures of propane [17] are included in the plot. Taken together, a broader understanding of stable reactor operation is attained.

Some operating points were not tested at high inlet velocities in order to avoid damage to the reactor due to high temperatures. Lean operation is achieved at minimum and maximum propane standard equivalence ratios of 0.36 and 0.44, over a range of inlet velocities from 60 to 225 cm/s. These conditions correspond to Reynolds numbers of approximately 100-600 based upon inlet conditions, putting reactor operation in the laminar regime. Stable operation in the lean regime is entirely below the conventional lean flammability limit of propane,  $\phi = 0.51$ , while the stable rich range spans from below to above the conventional rich flammability limit,  $\phi = 2.5$  [24]. In normalized form, the width of the stable rich regime is approximately 35% broader than the lean.

### Heptane

Figure D.6 is a stability plot for counterflow reactor operation on heptane/air reactants, where operating conditions are defined in terms of inlet velocity and both standard and normalized equivalence ratio. The operating conditions where the reactor operates stably, as well as conditions where operation becomes unstable due to flashback, blow-off or extinction, are shown. In addition to stability data acquired for lean combustor operation, previously obtained data for reactor operation on fuel-rich mixtures of heptane [18] are included in the plot.

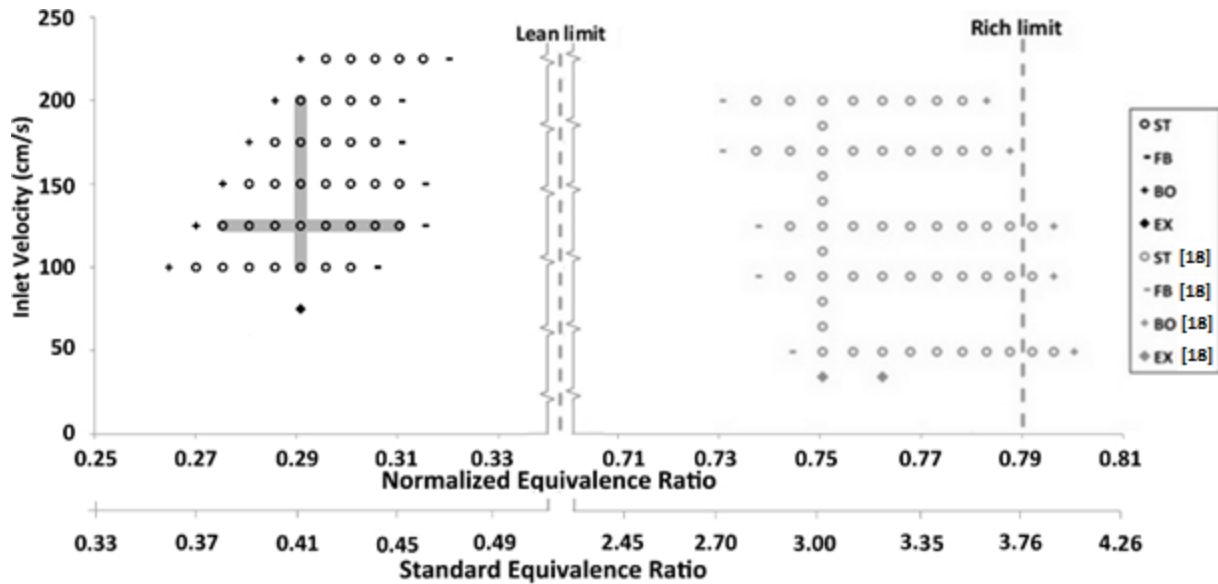


**Figure D.6: Stability map for counterflow reactor operation on lean and rich [18] heptane/air reactants, with stable (ST) and unstable points due to flashback (FB), blow-off (BO) and extinction (EX) shown as a function of inlet velocity and both standard and normalized equivalence ratios. Lean and rich flammability limits for heptane/air reactants at inlet conditions are indicated.**

Lean operation is achieved at minimum and maximum heptane standard equivalence ratios of 0.37 and 0.46, over a range of inlet velocities from 100 to 225 cm/s. The minimum stable inlet velocity, 100 cm/s, is significantly higher than previously tested fuels, methane and propane, which stabilized at 60 cm/s. Destabilization by extinction at the lower velocity limit, which occurs at 75 cm/s for heptane combustion at  $\phi = 0.41$  in the counterflow reactor, has been observed in previous studies as well [16-18]. This mode of destabilization results from the low rate of enthalpy input at low inlet velocities, while the rate of heat loss is a function of reactor temperature, which does not change proportionately. Stable operation in the lean regime is significantly below the conventional lean flammability limit of heptane,  $\phi = 0.56$ , while the stable rich range spans from below to slightly above the conventional rich flammability limit,  $\phi = 3.8$  [24]. In both standard and normalized form, the width of the stable rich regime is significantly broader than the lean.

### Emissions

Exhaust emissions of CO, NO<sub>x</sub> and UHCs, and peak wall temperature measurements are reported for lean reactor operation on methane, propane and heptane. Results are presented for two sets of tests: variation of inlet velocity with equivalence ratio held constant, and variation of equivalence ratio with inlet velocity held constant.

### Effect of Inlet Velocity

For a specified equivalence ratio, the equilibrium temperature is fixed and is not affected by volumetric flow rate. In a practical reactor, however, increasing the inlet velocity at a specified equivalence ratio increases the firing rate while altering the ratio of volumetric heat release to external heat loss, which is primarily affected by convection from the outside surface area. In addition, the residence time in the reactor decreases with increasing velocity. These two factors of temperature and residence time are important in the formation of emissions.

Figure D.7a shows CO exhaust concentrations and peak measured wall temperatures for lean reactor operation on heptane, propane and methane as a function of inlet velocity. Figure D.7b shows UHC exhaust concentrations and peak wall temperatures for propane and methane. For heptane, UHCs were undetected at all points and are not included in Figure D.7b. In order to facilitate direct comparison of the data presented in this study to other bodies of work, these results are presented in terms of standard equivalence ratio. Inlet velocity varies from 60 to 225 cm/s with equivalence ratio held constant at  $\phi = 0.44$  for methane and  $\phi = 0.41$  for propane, and from 100 to 200 cm/s for heptane at  $\phi = 0.41$ . Calculated adiabatic equilibrium temperatures for each fuel at the tested equivalence ratios are shown. Propane and heptane data were acquired at  $\phi = 0.41$ , as highlighted in the stability maps shown in Figs. D.5 and D.6, where broad ranges of stable inlet velocities were achieved for both fuels. Methane flames stabilized over a broad range of inlet velocities at an equivalence ratio of  $\phi = 0.44$ , as highlighted in Fig. D.4. Although this small difference in equivalence ratio complicates the comparison of the different fuels, it is still instructive to examine the trends associated with changes in inlet velocity which significantly affect reactor temperatures. This effect is attributed to an increase in the ratio of volumetric heat release within the reactor to heat losses from the surface of the reactor as inlet velocity increases. The change in reactor temperatures strongly impacts reaction rates, and therefore emissions.

Additionally, regions of combustor operation are defined based upon peak wall temperatures, and are indicated in Figures D.7a and D.7b. While peak gas temperatures are expected to be superadiabatic at all operating points based upon previous theoretical analyses [10], peak wall temperatures are a readily measured indicator of reactor conditions. Peak wall temperatures are the lowest temperatures experienced by the reaction zone; this has significant implications for reaction chemistry and quenching, and therefore emissions. The operating regions are designated as subadiabatic, near-adiabatic, and superadiabatic depending on the value of the peak reactor wall temperature relative to the adiabatic temperature, where near-adiabatic operation is identified where peak reactor temperatures are within approximately 50°C.

Propane combustion produces peak reactor wall temperatures that vary from 890 to 1233°C at the lowest and highest tested inlet velocities, respectively, and are superadiabatic at inlet velocities above 100 cm/s. The positive correlation of peak wall temperature with inlet velocity

is also shown for methane as well as in previous studies [16-18]. This is a result of increased rate of heat release within the reactor with increasing velocity compared to rate of heat loss to the surroundings. Heptane combustion produces a similar temperature trend, with peak wall temperatures increasing from 1046 to 1149°C with increasing inlet velocity. Heptane has a narrower stable operating range than propane and methane at the tested equivalence ratios; instability occurs at inlet velocities below 100 cm/s and above 200 cm/s.

The CO concentration from heptane combustion decreases from 259 ppm to 133 ppm with increasing inlet velocity. CO concentration from propane also decreases with increasing inlet velocity above 75 cm/s, with minor variation at the highest tested inlet velocities that is within calculated uncertainty. At the lowest tested inlet velocity of 50 cm/s, the concentration of CO is significantly less than the peak value of 123 ppm that occurs at 75 cm/s. UHCs from propane are detected at inlet velocities of 50 and 75 cm/s.

The results of propane combustion show temperature and CO trends that are similar to methane. Detection of UHCs at the lowest tested inlet velocities indicates incomplete fuel breakdown for both fuels. The absence of measured UHCs for heptane is attributed to the narrower stable operating range of heptane within the counterflow reactor, which is limited to a minimum inlet velocity of 100 cm/s. It is anticipated that UHC would be detected if heptane flames could be stabilized in the reactor at lower inlet velocities, following trends observed for methane and propane, however the current reactor geometry does not support heptane flames at inlet velocities below 100 cm/s at  $\phi = 0.41$ .

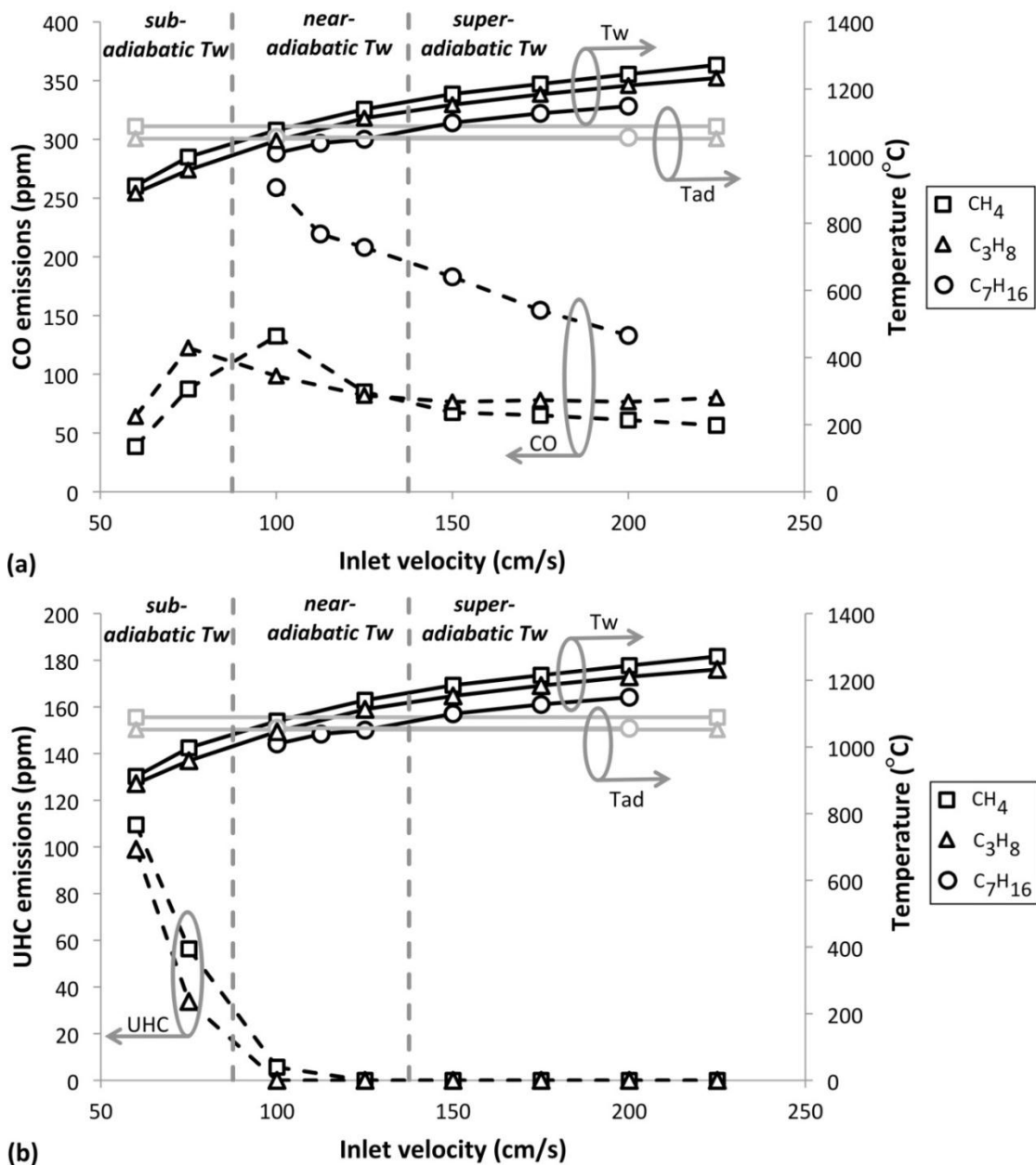
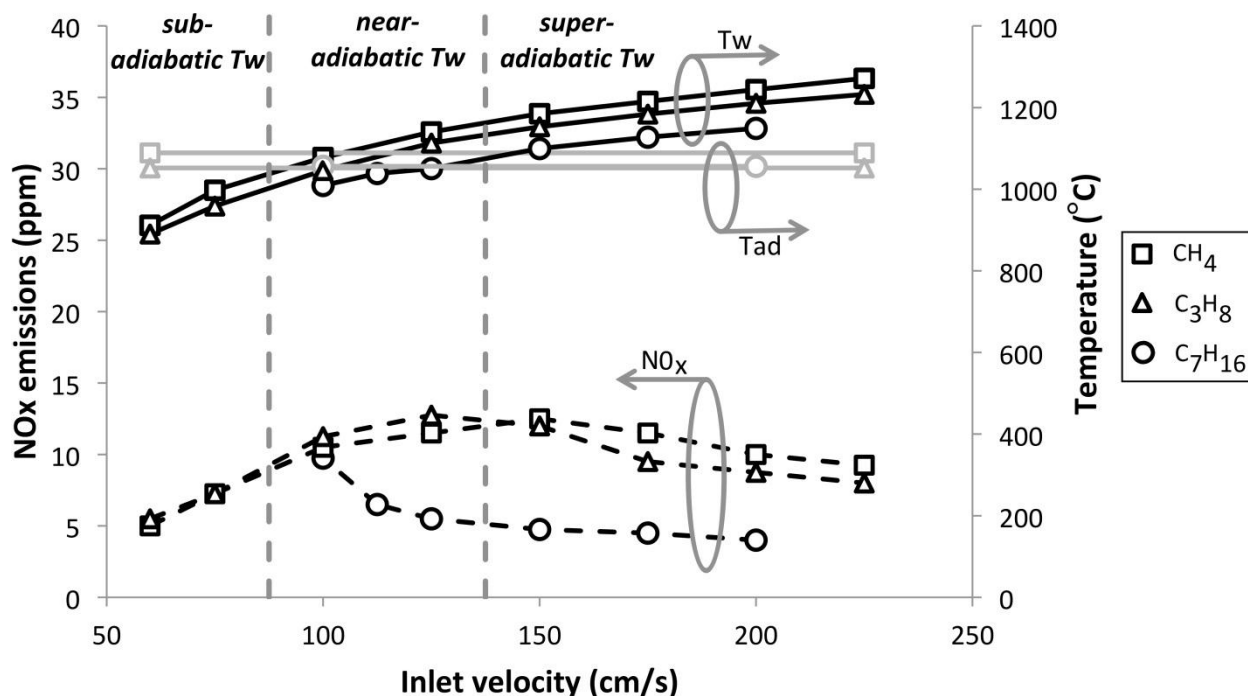


Figure D.7: (a) CO exhaust concentration and peak wall temperature ( $T_w$ ) for lean counterflow combustor operation on heptane, propane and methane, and (b) UHC exhaust concentration and peak wall temperature measured for lean counterflow combustor operation on propane and methane are shown. UHC are undetected at all tested heptane operating points and are not shown. A range of inlet velocities are tested with equivalence ratio held constant at  $\phi = 0.41$  for heptane and propane, and  $\phi = 0.44$  for methane. Calculated adiabatic equilibrium temperatures ( $T_{ad}$ ) for the tested equivalence ratios of each fuel are shown. Subadiabatic, near-adiabatic and superadiabatic operating regions, defined in terms of peak wall temperature, are also shown.

Figure D.8 shows NO<sub>x</sub> exhaust concentrations for combustion of lean heptane, propane and methane. Results are presented for inlet velocities from 60 to 225 cm/s with equivalence ratio held constant at  $\phi = 0.41$  for propane and  $\phi = 0.44$  for methane, and from 100 to 200 cm/s for heptane at  $\phi = 0.41$ . Peak measured wall temperatures and calculated adiabatic equilibrium temperatures are shown. Additionally, regions of combustor operation, defined by subadiabatic, near-adiabatic and superadiabatic peak wall temperatures, are indicated.



**Figure D.8: NO<sub>x</sub> exhaust concentration and peak wall temperature ( $T_w$ ) measured for lean counterflow combustor operation on heptane, propane and methane. Inlet velocity is varied with equivalence ratio held constant at  $\phi = 0.41$  for heptane and propane, and  $\phi = 0.44$  for methane. Adiabatic equilibrium temperatures ( $T_{ad}$ ) for the range of tested equivalence ratios of each fuel are shown. Subadiabatic, near-adiabatic and superadiabatic operating regions, defined in terms of peak wall temperature, are also shown.**

NO<sub>x</sub> concentration is below 13 ppm at all tested points. The highest NO<sub>x</sub> measurements occur at 125 cm/s for propane, and the concentrations decrease with increasing and decreasing inlet velocities from that point. The same trend is observed for methane combustion. The initial increase in NO<sub>x</sub> with inlet velocity is attributed to temperature dependence, whereas the variation at higher inlet velocities is largely within the estimated uncertainty. A slight decrease at the highest tested inlet velocities is attributed to decreased residence times at these conditions.

Heptane combustion produces the highest NO<sub>x</sub> concentration at the lowest tested inlet velocity. Concentration decreases with an increase in inlet velocity, and remains constant within the estimated uncertainty over the remainder of the tested inlet velocities.

Effect of Equivalence Ratio

For a fixed inlet velocity, a change in equivalence ratio changes the reactor firing rate while maintaining an approximately constant residence time. The necessary firing rate is determined by process requirements, while environmental considerations dictate acceptable emissions levels.

Figure D.9 shows CO exhaust concentrations and peak wall temperatures for lean reactor operation on heptane, propane and methane. Equivalence ratios are varied from 0.38 to 0.45 for heptane, 0.37 to 0.44 for propane and 0.41 to 0.48 for methane, with inlet velocity held constant at  $u = 125$  cm/s. Calculated adiabatic equilibrium temperatures for each fuel at the tested equivalence ratios are also shown. The widths of stable equivalence ratio ranges are the same for each fuel at an inlet velocity of 125 cm/s, where all emissions were measured for equivalence ratio variation. However, as can be seen in the stability maps shown in Figs. D.4, D.5 and D.6, the upper and lower limits of these stable ranges vary between the different fuels. Methane in particular exhibits a stable range that is shifted more significantly towards stoichiometric as compared to the other two tested fuels. Because there are no flameholders in the counterflow reactor, stable operation is obtained when the inlet flow is balanced by the burning rate, which is a function of equivalence ratio, preheat temperature, heat losses and recirculation, and fuel chemistry.

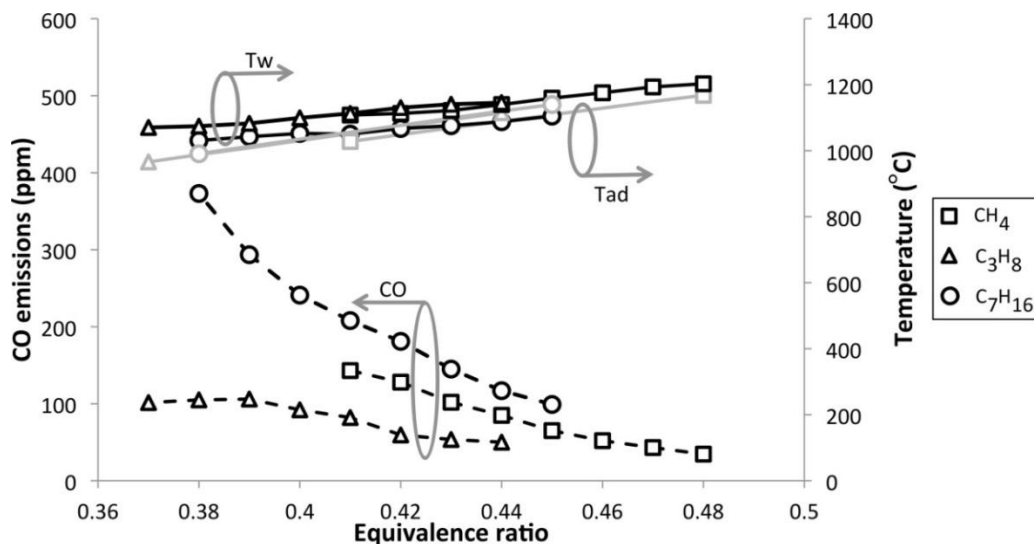


**Figure D.9: CO exhaust concentration and peak wall temperature (Tw) measured for lean counterflow combustor operation on heptane, propane and methane with varying  $\phi$  and inlet velocity held constant at  $u = 125$  cm/s are shown, as well as calculated adiabatic equilibrium temperatures (Tad) for the range of tested equivalence ratios of each fuel**

Methane, propane and heptane combustion result in modest increases of peak wall temperatures with equivalence ratio. For example, for heptane and propane, temperatures increase from 1046 to 1149°C and 1071 to 1146°C, respectively. The positive correlation of temperature with equivalence ratio for both fuels is also in agreement with trends predicted by chemical equilibrium. Comparison of measured and equilibrium temperatures shows that peak wall temperatures are superadiabatic at all tested methane and propane equivalence ratios. Peak wall temperatures for heptane are superadiabatic at equivalence ratios below 0.42, and are subadiabatic at the highest tested equivalence ratios. Peak wall temperatures as a function of equivalence ratio are generally within 50°C of the adiabatic equilibrium temperature for all fuels, and are considered to be in the near-adiabatic regime, thus the three operating regimes identified in Figures D.7 and D.8 are not identified in Figures D.9 and D.10.

The measured CO concentration for propane combustion initially increases slightly with increasing equivalence ratio from  $\phi = 0.37$  to  $\phi = 0.39$ , however the variation in this range is within calculated uncertainty. At higher equivalence ratios, CO concentration decreases with increasing equivalence ratio from a peak value of 106 ppm to 50 ppm at the highest tested equivalence ratio of 0.44. Likewise, the measured CO concentration for heptane combustion decreases from a peak value of 373 ppm at the lowest tested equivalence ratio of 0.38 to 99 ppm at the highest tested equivalence ratio of 0.45. This trend is in agreement with the results for methane, which show a decrease in CO concentration with increasing equivalence ratio across the tested range. As with methane, this negative correlation is in contrast to chemical equilibrium, which indicates an increase in CO concentration as equivalence ratio approaches stoichiometry. However, the measured values for heptane and propane combustion are significantly in excess of equilibrium, which predicts less than 1 ppm of CO at all tested equivalence ratios. Mesoscale reactors are particularly prone to reaction quenching at the channel walls as compared to larger reactors due to increased surface area-to-volume ratios, which leads to incomplete combustion. An additional challenge of high area-to-volume ratios in mesoscale reactors is the increased heat loss at channel walls, which produces lower reaction temperatures and therefore decreased reaction rates. Reactor temperatures and heat loss are also highly dependent on inlet conditions, including inlet velocity and equivalence ratio, which significantly impact the rate of volumetric heat release. The observed CO trend is attributed to a dependence on reactor temperature, which increases with equivalence ratio and drives the oxidation of CO toward CO<sub>2</sub> and equilibrium.

Figure D.10 shows NO<sub>x</sub> exhaust concentrations for lean reactor operation on heptane, propane and methane. Results are presented for varying equivalence ratio with inlet velocity held constant at  $u = 125$  cm/s. Again, peak wall temperatures and calculated adiabatic equilibrium temperatures are shown. The measured NO<sub>x</sub> concentration for heptane and propane combustion

increases with increasing equivalence ratio from 5 ppm at  $\phi = 0.37$  to 17 ppm at  $\phi = 0.44$ . The same trend is observed for methane combustion.

Unburned hydrocarbons are undetected at all tested equivalence ratios for lean heptane, propane and methane combustion, indicating complete fuel breakdown.

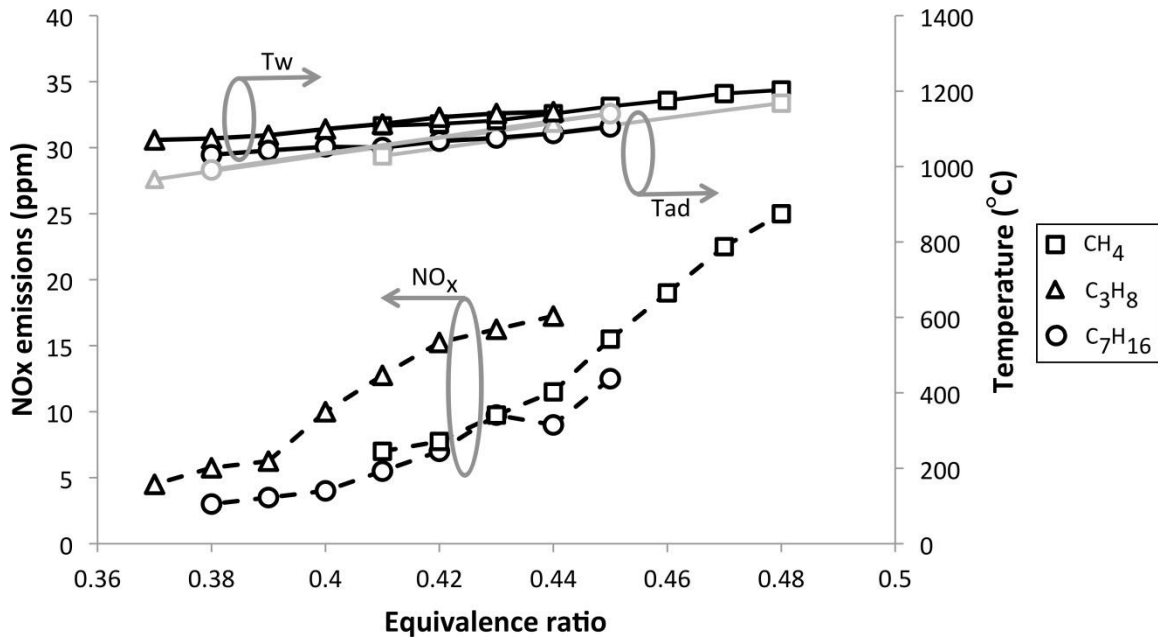


**Figure D.10: NO<sub>x</sub> exhaust concentration and peak wall temperature ( $T_w$ ) measured for lean counterflow combustor operation on heptane, propane and methane with varying  $\phi$  and inlet velocity held constant at  $u = 125$  cm/s are shown, as well as adiabatic equilibrium temperatures ( $T_{ad}$ ) calculated for the range of tested equivalence ratios of each fuel**

### Effect of Superadiabatic Operation

The peak reactor wall temperatures measured during experiments are categorized as subadiabatic, near-adiabatic and superadiabatic relative to the calculated adiabatic equilibrium temperature of the unburned fuel mixture, and are labeled accordingly in Figs. D.7 and D.8. In a reactor that operates without heat recirculation, temperatures will necessarily be subadiabatic everywhere because of unavoidable heat losses from the system. In a heat-recirculating reactor, however, temperatures in excess of the adiabatic equilibrium temperature can be achieved through conduction and radiation by the solid structure of the reactor, and through convection by the gas. Previous theoretical analyses of the counterflow reactor indicate that peak gas temperatures within the reactor channels are significantly in excess of wall temperatures [10]. Furthermore, experiments and computations of stationary flames in ducts constructed of low thermal conductivity materials show that wall temperatures in such systems are significantly less than centerline peak temperatures and adiabatic temperatures [25-27]. While peak gas temperatures at the centerlines of the reactor channels are therefore expected to be significantly

higher than peak wall temperatures, the latter are more readily measured without interfering with reactor dynamics, such as by flameholding. Furthermore, reactor wall temperatures are quite important in determining quenching and heat loss rates. Therefore, peak wall temperatures provide an important and practical metric by which reactor performance can be evaluated and monitored. The results of this study reveal common trends in fuel emissions as the peak wall temperatures change with varying inlet conditions of equivalence ratio or inlet velocity. Regions of operation can be distinguished in terms of peak wall temperature, where distinct trends are noted depending on the value of the peak wall temperature relative to the calculated adiabatic equilibrium temperature. The results highlight the importance of achieving significantly superadiabatic peak temperatures within the reactor channels, which will result in near-adiabatic or superadiabatic wall temperatures due to heat losses at external surfaces, in achieving favorable emissions.

The current analysis of peak reactor wall temperature relative to calculated adiabatic equilibrium temperature is distinguished from a global definition of superadiabatic performance that is used in the discussion of heat recirculating reactors, which refers to the peak temperature in the gas phase of the reactor relative to the calculated adiabatic equilibrium temperature. The peak wall temperatures observed in this study approach or are above the calculated adiabatic equilibrium temperatures for each fuel. Therefore, based upon previous theoretical and experimental analyses of heat recirculating reactors which account for heat losses at the wall at all conditions, all reported cases in this study most likely exhibit superadiabatic temperatures at the centerline of the reactor channel, and operation would therefore be deemed superadiabatic by global definition. The current analysis, however, focuses on the categorization of peak wall temperature relative to calculated equilibrium temperature, and uses the designation of subadiabatic, near-adiabatic and superadiabatic to convey the relative magnitudes of these values.

Inlet velocity has a significant effect on the peak wall temperature, which is as much as 200°C greater than the adiabatic temperature at the conditions tested in this study. In Figures D.7 and D.8, regions of subadiabatic, near-adiabatic, and superadiabatic peak wall temperature conditions have been identified. Stable operation for heptane was not obtained at significantly subadiabatic wall temperature conditions. For methane and propane, high levels of UHCs are detected at subadiabatic wall temperature conditions, and NO<sub>x</sub> concentrations are low. These results are consistent with incomplete combustion.

At conditions where near-adiabatic wall temperatures were measured, CO peaks and then decreases with increasing inlet velocity for all fuels and UHCs are not detected at the highest tested inlet velocities in this regime. The variation of NO<sub>x</sub> among the different fuels in this region is not consistent: concentrations increase for propane and methane and decrease for heptane. It should be noted, however, that all NO<sub>x</sub> concentrations are less than 15 ppm.

At conditions where superadiabatic peak wall temperatures were measured, the emissions of all reported species are fairly constant with the exception that CO for heptane/air continues to decrease.

A negative correlation of CO with temperature is observed in all data, except those points where UHCs are detected for methane and propane (Figures D.7 and D.9). These products are far from equilibrium values, which predict less than 1 ppm for both CO and UHCs. In contrast, no UHCs are detected for heptane combustion. Likewise, no significantly subadiabatic wall temperatures are measured at any stable heptane operating points. The stable range of inlet velocities is narrower for heptane as compared to methane and propane. Flashback occurs at a higher inlet velocity for heptane compared to the other two fuels, and the lowest stable velocity is limited to approximately where the measured peak wall temperatures become subadiabatic. In contrast, methane and propane are able to stabilize at significantly subadiabatic wall temperatures, but UHCs are measured at these points (Figure D.7).

Heptane is likewise limited at the high end of the tested inlet velocity range by blow-off at 225 cm/s, whereas methane and propane are stable at this condition. Peak wall temperature values are lower for heptane than methane and propane across the tested range of inlet velocities (Figures D.7 and D.8). Flame temperature and speed are strongly dependent on reactant temperature; therefore peak wall temperature and burning rate within the reactor are expected to be highly dependent on the extent of counterflow heat exchange from combustion products in order to preheat counterflowing reactants in adjacent channels. Since the counterflow reactor requires burning rate to equal reactant velocity in order to operate stably, insufficient preheating of reactants leads to heptane blow-off at high inlet velocities.

The results of lean methane, propane and heptane combustion suggest significant changes in stability and emissions behavior when the peak wall temperatures become subadiabatic. Emissions concentrations indicate that low wall temperatures in the subadiabatic peak wall temperature regime do not promote sufficient reaction rates for complete fuel breakdown, and increasing wall temperatures into the adiabatic and superadiabatic regimes drive reactions toward equilibrium. Emissions and stability range results suggest that combustor operation with peak wall temperatures in the near-adiabatic and superadiabatic regimes is desirable for allowing increased firing rates and decreased emissions. The most significant decline in emissions is seen in the transition from subadiabatic to near-adiabatic peak wall temperatures, while further temperature increase into the superadiabatic regime produces marginal additional advantage. The more significant advantage of operation in the superadiabatic wall temperature regime is found in extension of the stable combustor operating range, as highlighted by the absence of heptane stability in the subadiabatic wall temperature regime. This finding is in agreement with a previous investigation of preheated flames [28].

In contrast to the previous cases in which peak wall temperature was significantly affected by changes in velocity, the peak wall temperature as a function of equivalence ratio (Figures D.9 and D.10) is generally within 50°C of the adiabatic equilibrium temperature at the tested inlet velocity of 125 cm/s for each fuel, and is considered to be in the near-adiabatic regime. Emissions of CO decrease and NO<sub>x</sub> increase with increasing equivalence ratio for all three fuels. Measured concentrations are significantly above equilibrium values, and the observed trends are attributed to temperature dependence.

While the data for equivalence ratio variation with an inlet velocity of 125 cm/s show peak wall temperatures in the near-adiabatic regime, Figures D.7 and D.8 indicate that an increase or decrease in the inlet velocity may result in a shift of the peak wall temperatures into the superadiabatic or subadiabatic regimes. The effects of such a shift on stability and emissions can be anticipated based upon the results for inlet velocity variation.

#### **D.4 Conclusion**

Lean premixed combustion of methane, propane and heptane was studied in a heat recirculating mesoscale counterflow reactor. This reactor design has previously been used to study the conversion of rich methane, propane and heptane reactant mixtures to hydrogen-rich synthesis gas. The current study expands the established capability of the counterflow reactor to operate in the lean combustion regime on increasingly complex fuels. In particular, liquid fuels are generally easier and safer to transport than gaseous fuels, and are studied because of their logistical importance.

Results included reactor stability maps for methane, propane and heptane combustion that show stable operating points, as well as points where operation became unstable due to flashback, blow-off or extinction, for rich and lean reactant mixtures. Emissions of CO, NO<sub>x</sub> and UHC were presented for lean methane, propane and heptane operation. Additionally, operating regions were defined in terms of peak reactor wall temperatures. Similarities in trends between the three tested fuels highlight the correlation of emissions with peak reactor wall temperature, and support previous findings that a minimum firing rate is necessary for optimal performance. Further analysis highlights the importance of achieving peak wall temperatures near, or in excess of, the calculated adiabatic equilibrium temperature of the fuel at inlet conditions in heat-recirculating reactors for emissions minimization and stable range extension.

#### **D.5 References**

1. A.C. Fernandez-Pello, Proc. Combust. Inst. 29 (2002) 883–899.
2. F.J. Weinberg, D.M. Rowe, G. Min, P.D. Ronney, Combust. Flame 135 (2003) 421–439.
3. J. Vican, B.F. Gajdeczko, F.L. Dryer, D.L. Milius, I.A. Aksay, R.A. Yetter, Proc. Combust. Inst. 29 (2002) 909–916.

4. S. Wood, A.T. Harris, *Prog. Energy Combust. Sci.* 34 (2008) 667– 684.
5. T.L. Marbach, A.K. Argrawal, *J. Propul. Power* 22(1) (2006) 145-150.
6. C. Keramiotis, B. Stelzner, D. Trimis, M. Founti, *Energy* 45 (2012) 213-219.
7. V. Bubnovich, M. Toledo, L. Henríquez, C. Rosas, J. Romero, *Appl. Therm. Eng.* 30(2–3) (2010) 92-95.
8. L.A. Kennedy, J.P. Bingue, A.V. Saveliev, A.A. Fridman, S.I. Foutko, *Proc. Combust. Inst.* 28(1) (2000) 1431-1438.
9. R.V. Fursenko, S.S. Minaev, V.S. Babkin, *Combust. Explos. Shock Waves* 37(5) (2001) 493–500.
10. I. Schoegl, J.L. Ellzey, *Combust. Flame* 151(1-2) (2007) 142–159.
11. Y. Ju, B. Xu, *Proc. Combust. Inst.* 30 (2005) 2445–2453.
12. Y. Ju, C.W. Choi, *Combust. Flame* 133 (2003) 483–493.
13. P.D. Ronney, *Combust. Flame* 135 (2003) 421–439.
14. N.I. Kim, S. Aizumi, T. Yokomori, S. Kato, T. Fujimori, K. Maruta, *Proc. Combust. Inst.* 31 (2007) 3243–3250.
15. J. Ahn, C. Eastwood, L. Sitzki, P.D. Ronney, *Proc. Combust. Inst.* 30 (2005) 2463–2472.
16. I. Schoegl, J.L. Ellzey, *Proc. Combust. Inst.* 32(2) (2009) 3223–3230.
17. I. Schoegl, S.R. Newcomb, J.L. Ellzey, *Int. J. Hydrogen Energy* 34 (2009) 5152–5163.
18. E.L. Belmont, S.M. Solomon, J.L. Ellzey, *Combust. Flame* 159 (2012) 3624–3631.
19. H.J. Curran, P. Gaffuri, W.J. Pitz, C.K. Westbrook, *Combust. Flame*, 114 (1998) 149–177.
20. B.J. Matkowsky, G.I. Sivashinsky, *SIAM J. Appl. Math.* 37 (3) (1979) 686–699.
21. D.G. Goodwin, *Proc. CVD XVI and EuroCVD Fourteen*, Electrochem. Soc. (2003) 155-162.
22. G.P. Smith, D.M. Golden, M. Frenklach, N.W. Moriarty, B. Eiteneer, M. Goldenberg, C.T. Bowman, R.K. Hanson, S. Song, J.W.C. Gardiner, V.V. Lissianski, Z. Qin, *GRI-Mech 3.0*, available at <[http://www.me.berkeley.edu/gri\\_mech/version30/](http://www.me.berkeley.edu/gri_mech/version30/)> (1999).
23. C.K. Law, *Combustion Physics*, Cambridge University Press, 2006.
24. M.G. Zabetakis. (Bulletin 627). US Bureau of Mines, Wash., D.C. (1965).
25. V. Zamashchikov, E. Tikhomolov, *Int. J. Hydrogen Energy* 36(14) (2011) 8583–8594.
26. C.J. Evans, D.C. Kyritsis, *Combust. Sci. Tech.* 183(9) (2011) 847 -867.
27. I.M. Schoegl, J.L. Ellzey, *Combust. Sci. Tech.* 182(10) (2010) 1413-1428.
28. C.H. Smith, D.I. Pineda, J.L. Ellzey, *Combust. Flame* 160(3) (2013) 557-564.

## **Appendix E: Syngas production from burner-stabilized methane/air flames: the effect of preheat**

The funding from ARO was leveraged with support from supplemental sources which permitted the investigation of other questions related to the conversion of a hydrocarbon fuel/air mixture to syngas. The work below is published in C.H. Smith, D.I. Pineda, and J.L. Ellzey, “Syngas Production From Burner-Stabilized Methane/Air Flames: The Effect of Preheated Reactants”, *Comb. Flame* (160) pp. 557-564, 2013.

### **E.1 Introduction**

Heat recirculating reactors, in which heat is transferred from hot products to cold reactants, allow the combustion of mixtures with equivalence ratios ( $\phi$ ) outside the conventional flammability limits and with burning velocities far in excess of laminar flame speeds [1-3]. In addition, local peak temperatures can be superadiabatic, i.e. greater than those predicted by equilibrium. Because of these unique characteristics, heat recirculating reactors have been proposed as low emissions radiant heaters and combustors [4-6] and fuel reformers. A significant amount of work has been done on fuel reforming in particular, where a rich mixture of fuel and oxidizer is reacted to produce syngas—a mixture of hydrogen ( $H_2$ ), carbon monoxide (CO) and other species [3-11].

Generally, in these reactors both conduction and radiation are enhanced over gaseous values by the presence of a solid surface, and in some designs, such as a packed bed or filtration reactor, mass transfer is enhanced over the gas phase levels [12, 13]. The complexity of the transport processes in these reactors makes analysis and the determination of the critical design parameters difficult.

Previous research has shown that the stable operating range, defined as the sets of  $\phi$  and inlet velocity ( $V$ ) where stable combustion is attained, varies widely depending on the reactor design even when operating on the same fuel. For example, when operating on methane stable operation in a packed bed reactor was demonstrated up to  $\phi = 5.0$  [14] while for a counterflow reactor the limit was at  $\phi = 2.5$  [15]. When the reaction front was stabilized at the interface of two sections of porous media the limit was  $\phi = 1.9$  [10].

The conversion of the reactants to syngas also depends on the reactor design. Experiments reforming methane to syngas with filtration reactors [14, 16], a counterflow reactor [15] and another type of porous media reactor [7] showed a variety of syngas yields with maximum  $H_2$  yields ranging from 40% to more than 70% amongst the different reactors. Furthermore, experiments reforming heptane to syngas with two different reactor types [17, 18] showed different reforming efficiencies. The filtration reactors typically produce the highest syngas yields, but since the stable operating conditions of the various reactors typically do not overlap, a direct comparison is difficult.

Several computational studies have shown the importance of conduction, radiation, and solid-to-gas heat transfer in these reactors [19-22]. The significant outcome of these enhanced processes is that the reactants are preheated and will therefore react even at extreme equivalence ratios. In these devices, the preheat temperature is a function of both the properties of the reactor and the combustion process. In one study [6], the inlet mixture to a porous reactor was preheated externally to a controlled temperature but since additional heat transfer takes place within the reactor, the effective preheat temperature is difficult to discern. The development of an optimal design is challenging because the level of preheat required for conversion and the specific effect of preheat temperature on the conversion are unclear. An additional complication is that preheating sometimes occurs under conditions where mass transfer is substantially enhanced.

The purpose of our work was to understand the effect of preheat temperature on the conversion of rich mixtures of methane/air to syngas. In order to examine the specific effect of preheat temperature, we investigated flames stabilized on flat flame burners. In contrast to heat recirculating reactors, flat flame burners allow the control of preheat temperature and do not have enhanced transport processes that complicate the analysis.

There has been very substantial work on premixed methane/air laminar flames stabilized by various methods including on flat flame burners. Most studies have focused on lean or near-stoichiometric conditions, though there are many published investigations of rich burner-stabilized flames as well. Most of the experiments with rich flames were studies of detailed flame structure conducted at low-pressure [23]. It is known that kinetics can differ between low and high pressure [23, 24] so studies at high pressure are important to supplement the detailed low-pressure flame investigations. The studies at atmospheric pressure [25-28], have typically focused on flame structure or measurements of flame speed rather than the concentrations of species over a wide range of conditions as is reported in this work. In one exception [26], CO concentrations over a range of equivalence ratios were measured. Previous studies of rich premixed methane/air flames with preheated reactants have not included exhaust product measurements with the exception of NO<sub>x</sub> [29-33].

In this study, we examined experimental measurements and computational predictions of exhaust products for rich methane/air flames with and without preheated reactants. Chemical kinetic and flame models have not been validated extensively for very rich equivalence ratios [34], therefore we include comparisons of various global flame characteristics such as standoff distance, flame temperature, and stable operating range to establish confidence in these models to make adequate predictions. The models are then used to compare to the experimental data from rich flames with and without preheated reactants and also to extend the range of temperature conditions that are investigated.

## E.2 Numerical and analytical approach

One dimensional simulations of burner-stabilized flames and laminar freely-propagating flames were performed using Cantera [35] with GRI3.0 [36]. GRI3.0 was initially modified to include a CH\* reaction using a set of reactions by Hai Wang (personal communication), though we found that the location of the CH\* and CH were nearly identical. Because of this similarity, the original GRI3.0 mechanism was used for all simulations.

For a burner-stabilized flame, the energy equation was solved with an upstream boundary condition of constant temperature and a downstream boundary condition of zero temperature gradient. The species conservation equation was solved with multicomponent transport. The upstream species boundary condition is zero concentration, and the downstream condition was zero gradient. The domain was 1 cm for all simulations.

For a freely-propagating flame, the energy equation was solved with upstream and downstream boundary conditions of zero temperature gradient. The species conservation equation was solved with multicomponent transport. The upstream and downstream species boundary conditions were zero gradient. The domain was 30 cm. The details of the burner-stabilized flame model and the freely-propagating flame model can be found in the Cantera documentation [35].

In addition to the detailed computational models, the analytical solution of Law [37] was used to compute the standoff distance as a function of operating conditions and to understand the basic behavior of burner-stabilized flames. The nondimensional governing equations for flame temperature, standoff distance and heat loss are:

$$\tilde{f}^2 = \left(\frac{\tilde{T}_f}{\tilde{T}_{ad}}\right)^4 \exp\left[-\tilde{T}_a\left(\frac{1}{\tilde{T}_f} - \frac{1}{\tilde{T}_{ad}}\right)\right] \quad (\text{E.1})$$

$$\tilde{f}[\tilde{T}_{ad} + (\tilde{T}_s - \tilde{T}_u)] - \tilde{L}_s = \tilde{f}\tilde{T}_f \quad (\text{E.2})$$

$$\tilde{L}_s = \frac{\tilde{f}(\tilde{T}_f - \tilde{T}_s)}{e^{\tilde{f}\tilde{x}_f} - 1} \quad (\text{E.3})$$

where the nondimensional variables for mass flux, temperature, standoff distance and heat loss are given by:

$$\tilde{f} = \frac{f}{f^\circ}, \tilde{T} = \frac{T}{T_{ad} - T_u}, \tilde{x} = \frac{xf^\circ}{\rho D}, \tilde{L}_s = \frac{d\tilde{T}}{d\tilde{x}}$$

and  $f$  is the mass flux,  $f^\circ$  is the laminar burning flux,  $T$  is the temperature,  $T_{ad}$  is the adiabatic flame temperature based on the unburned reactant temperature,  $T_u$ ,  $x$  is the standoff distance,  $\rho$  is the density, and  $D$  is the mass diffusion coefficient.

To obtain dimensional values for the quantities of interest, laminar burning fluxes and adiabatic flame temperatures obtained from Cantera solutions were used. Two other parameters, the activation temperature,  $T_a$ , and the product,  $\rho D$ , required dimensional values. Both of these parameters were set by calibration to experimental data. The activation temperature was set to 15098 K such that the flame temperature given by the analytical model matched the flame temperature, 1850 K, for methane/air at  $\phi = 1.2$ ,  $V = 11$  cm/s as reported by [27]. Setting  $\rho D = 5.5E-5$  yielded the best fit to our experimental data for standoff distance at  $\phi = 1.25$ . This value of  $\rho D$  corresponded to the mass average value of  $\rho D$  for a mixture of methane and air with  $\phi = 1.25$  at approximately 1025 K.

We also performed equilibrium calculations for varying  $\phi$  and initial reactant temperature to compare with data from combustion processes that approach equilibrium in the limit of infinitely fast kinetics and adiabatic conditions [11, 17]. In these calculations, the initial temperature and  $\phi$  were selected and enthalpy and pressure were held constant for equilibration. The equilibrium calculations provide insight into the thermodynamic properties of the mixtures, and equilibrium has been assumed to represent the species concentrations in the post-flame region of burner-stabilized flames [27, 38]. These calculations were performed in Cantera with thermodynamic data from GRI3.0. Solid carbon formation was included in all of the presented equilibrium calculations. These calculations show that no solid carbon is formed for methane/air mixtures until  $\phi$  exceeds approximately 3.3.

The models are used to predict flame standoff distance in terms of the location of maximum CH concentration, flame temperature, stability limits and species yields. Experimentally, we define a stability limit as  $\phi$ ,  $V$  pair where if  $V$  is increased the flame ceases to be flat. For the burner-stabilized flame model, the limit is defined as the maximum  $V$  for a given  $\phi$  that produces a converged solution. An additional limit comparison is based on the laminar flame speed of a mixture where the predicted laminar flame speeds are compared to the limiting velocities determined experimentally at each  $\phi$ . Lastly, the models and experiments were compared in terms of exhaust species yields. A summary of the conditions for comparison is shown in Table E.

	Measured Value	Calculated Value Burner Stabilized Flame	Calculated Value Free Flame
Given $\phi$ , V	Standoff distance	Standoff distance	NA
Given $\phi$ , V	Flame temperature from [27]	Flame temperature	NA
Given $\phi$	Maximum V for flat flame	Maximum V at which solution converged	Laminar flame speed for given $\phi$
Given V	Maximum $\phi$ for flat flame	Maximum $\phi$ at which solution converged	$\phi$ at which laminar flame speed equals given V
Given $\phi$ , V	Species yields	Species yields	Species yield if laminar flame speed = V at given $\phi$

**Table E.1: Conditions for comparing models and experiment. In each row the quantity of interest for comparison is listed for operating condition(s) given in the far left column.**

### E.3 Experimental approach

#### Experimental Apparatus

Experiments were performed with two different burners. Experiments without preheat were conducted on a water-cooled McKenna burner (Holthius & Associates), which has a sintered porous bronze plate as the burner-surface. The water flow was  $\sim 13$  g/s for all experiments, efficiently cooling the burner surface. The McKenna burner was used to establish a baseline with which to compare the experiments with preheated reactants and to determine the accuracy of the models since the McKenna burner is well-established for this comparison. We constructed a second burner, similar to that used in other studies of flat flames [33, 39], for experiments with preheated reactants. This burner was a square channel mullite ceramic matrix with 1.34 mm channels and 0.35 mm walls. The matrix was 51 mm long and 55 mm in diameter. A diagram of this burner is shown in Fig. E.1.

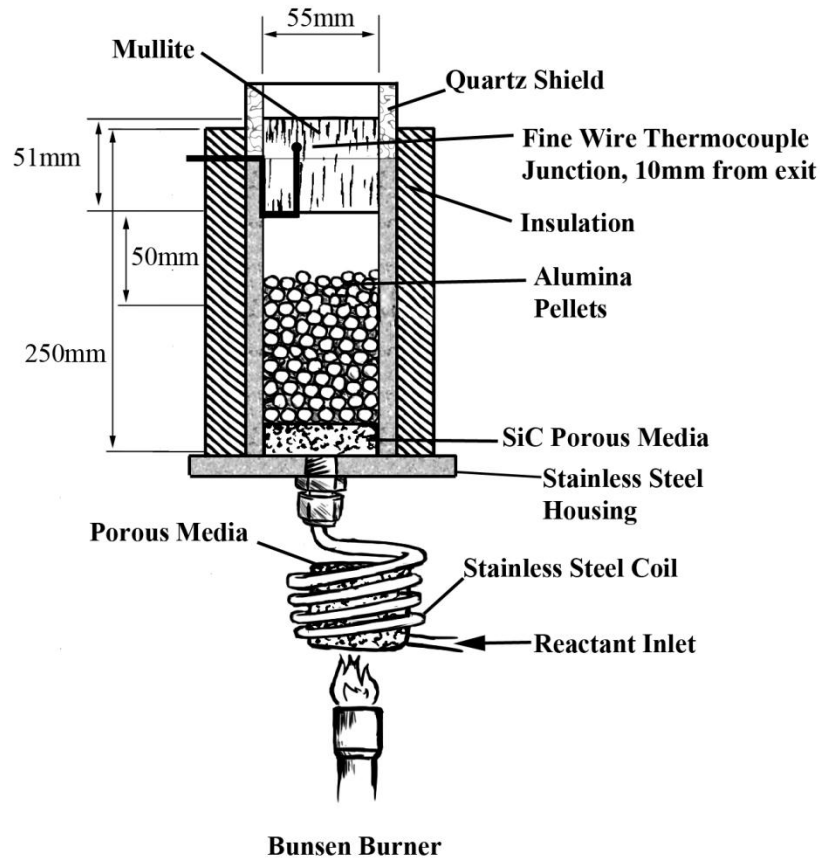


**Figure E.1: Diagram of ceramic burner**

As described by Law [37], when the mass flux and mixture properties ( $\phi$ , unburned gas temperature) are specified in Equation E.1, the flame temperature is determined and is independent from the surface temperature and standoff distance. Since the reaction zone is confined to a thin region at or very near the flame temperature, this flame temperature can be considered the controlling temperature for the chemical reactions and product species. Therefore the product species distributions for the ceramic burner, which does not have a controlled surface temperature, the McKenna burner and the burner-stabilized flame model may be directly compared when the mass flux and mixture properties are identical. In addition they may be compared in terms of limit conditions because under limit conditions there is no thermal interaction between the flame and the burner surface.

The standoff distances are not compared to the modeling results for preheated reactants because the standoff distance is a function of the surface temperature, which is not controlled in these experiments using the ceramic burner. In contrast to the McKenna burner where the surface temperature is effectively controlled by the temperature of the cooling fluid, in the ceramic burner the surface temperature is a function of operating conditions. Stabilization is achieved

through heat loss to the environment primarily by radiation from the burner surface. The required heat loss and burner surface temperature, then, determine the standoff distance.

In all experiments, a quartz tube of 55 mm ID was used to shield the flames from external air. The quartz tubes were used instead of inert gas shielding because the exhaust gas samples were extracted from the center of the flame, where the quartz tube boundary had no effect. We found no observable difference in any measurements by running experiments with and without the quartz tube as a shield.

The flows were controlled with calibrated Hastings mass flow controllers. The air was compressed, dry laboratory air, and the methane was CP grade from Air Liquide. Preheating was accomplished by running the premixed methane/air through a helical coil of stainless steel heated by a Bunsen-burner before entering the reactor housing. The temperature of the reactants was monitored by a fine wire K-type thermocouple placed within the ceramic plug upstream of the preheat zone of a burner-stabilized flame. It was confirmed that fuel breakdown did not occur due to preheating before reaching the flame by sampling the gases after heating but without a flame.

We also built a system to measure the spatial location and intensity of CH\* chemiluminescence for the measurement of flame standoff distance and flatness. This system was a digital webcam (Logitech™ C910 HD), a vertical traverse with a micrometer head, and a LabVIEW™ control system, along with a  $430\pm 10$  nm optical bandpass filter.

### **Species measurement**

Measurements of species concentrations in the exhaust were taken with a Varian (Agilent) CP-4900 gas chromatograph, which measures H<sub>2</sub>, CO, nitrogen (N<sub>2</sub>), carbon dioxide (CO<sub>2</sub>), methane (CH<sub>4</sub>), ethylene (C<sub>2</sub>H<sub>4</sub>), acetylene (C<sub>2</sub>H<sub>2</sub>) and select higher hydrocarbons. No compounds greater than C<sub>2</sub> were detected in any experiments. The samples were all drawn from 1 cm above the burner surface with a water-cooled sample probe. The probe had a 1 mm OD injection point to minimize system disturbance. The sources of uncertainty were in the flow rates of methane and air, the calibration standards, and the gas chromatograph calibration. Uncertainties in species measurements were calculated using a Student-t distribution, and uncertainties for calculations were based on sequential perturbation. The species results are reported in terms of dry species concentrations.

### **Determination of flame flatness**

When a flame approaches a blow-off condition, the flame loses its flatness, and when a flame is in a flashback condition, it is not visible. Since we wanted to compare our experimental results to one-dimensional computational models of burner-stabilized flames, it was important to establish

a criterion for a “flat” flame that was also not in a flashback condition. In addition, we define the stability limit as the as the  $\phi$ ,  $V$  pair beyond which a flame would not be flat if the inlet velocity was increased at the given  $\phi$ . We found these limiting conditions by perturbing  $\phi$  and  $V$  while monitoring the flame flatness through  $\text{CH}^*$  chemiluminescence imaging. A representative grayscale  $\text{CH}^*$  chemiluminescence image is shown in Fig. E.2.

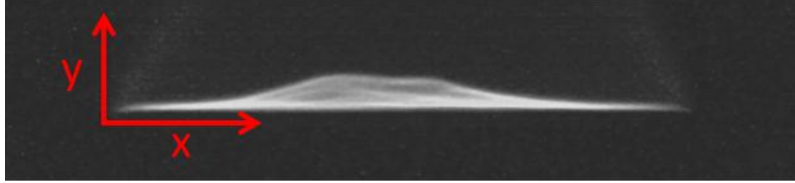


**Figure E.2: Pictorial diagram describing the flatness metric used in this study on a highly non-flat flame**

The flame flatness was quantified by finding the variance of the full width (in  $y$  direction) at half maximum (FWHM) grayscale intensity along the  $x$  axis. By this definition, a perfectly flat flame has zero FWHM intensity variance.

To determine the experimental limiting conditions (the conditions where increases in  $\phi$  or  $V$  would produce a nonflat flame), velocity was held constant while  $\phi$  was adjusted by increments of 0.005 for five different values of  $\phi$  surrounding a suspected limit and images were taken to determine the FWHM variance for each condition. A limit value of  $\phi$  was defined as a tested  $\phi$  limit where the FWHM variance found in the set of five conditions at least doubled. Flames with operating conditions within the bounds of the limiting conditions were considered flat, and in this paper we only report measurements from flat flames.

#### **E.4 Results and discussion**

Previous research on the conversion of rich fuel/air mixtures has shown that optimal production of syngas may occur beyond the conventional flammability limits. Optimization, however, of reactor performance remains challenging because the level of preheat necessary is unclear. In the following sections, we discuss experimental, computational, and analytical results which provide some insight into the importance of preheating for conversion of rich methane/air mixtures.

##### **Comparison of experimental and numerical modeling data**

Since combustion models are not extensively compared to experimental data in the rich regime [34], we present comparisons of standoff distance, stability, and temperature in order to gain confidence in the predictions of the models, which are subsequently used to investigate a broader range of conditions than was investigated experimentally. In this section the computational

models were compared to the results from experiments on the McKenna burner and the analytical model under non-preheated conditions.

### Standoff distance

For a flat flame to stabilize on the surface of a burner, the burning velocity of the flame must match the inlet velocity. Matching of these velocities occurs because heat loss to the burner decreases the flame temperature and therefore decreases the burning velocity as described in detail in the literature [37, 40, 41]. The standoff distance, which we use for comparison between the model and experiment, is a fundamental characteristic of burner-stabilized flames and has been used by other researchers for such comparison [42, 43].

Experimental, computational, and analytical results show that the flame standoff distance decreases with increasing inlet velocity, as shown in Fig. E.3. In the range of inlet velocities tested, the model and experiment agreed very well in both trend and magnitude, and the analytical model fits the data very well. This trend has been observed by other researchers and is explained in detail in the literature [32, 41].

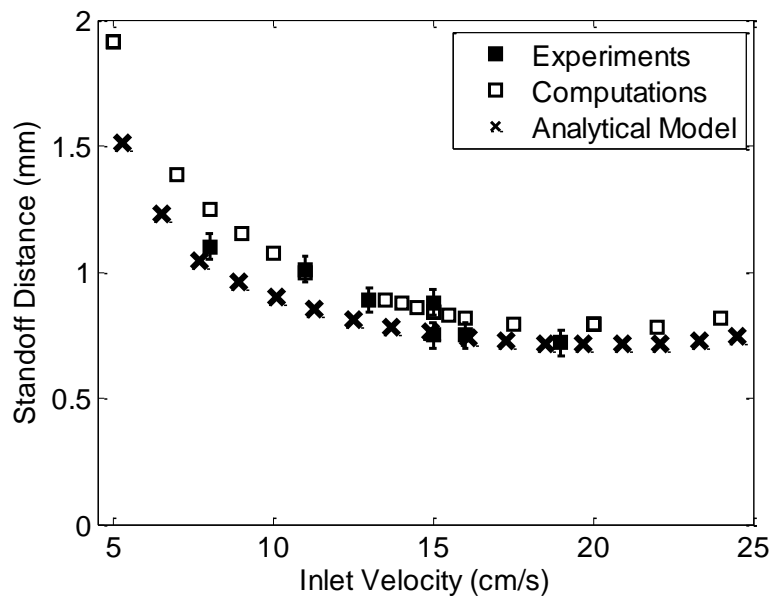


**Figure E.3: Standoff distance vs. inlet velocity at equivalence ratio =  $1.25 \pm 0.05$**

We also compared the modeling predictions with the experimental measurements of standoff distance as a function of  $\phi$  while  $V$  was held constant at 15 cm/s (Fig. E.4). Again, the agreement between the experiments, the burner-stabilized flame model and the analytical model is very good. The same trend was observed by Ferguson and Keck [40], and their standoff distance measurements were within about 1 mm of those reported here even though the reactant temperature in their experiments was 50 K greater than the temperature of the reactants in our experiments.

The standoff distance is one of the fundamental global parameters that characterize burner-stabilized flames. Over a range of  $V$  and  $\phi$ , the burner-stabilized flame model was a very good predictor of standoff distance. Law's analytical model also fits the experimental and modeling data very well in trend and in magnitude except for a slight overprediction near stoichiometric.

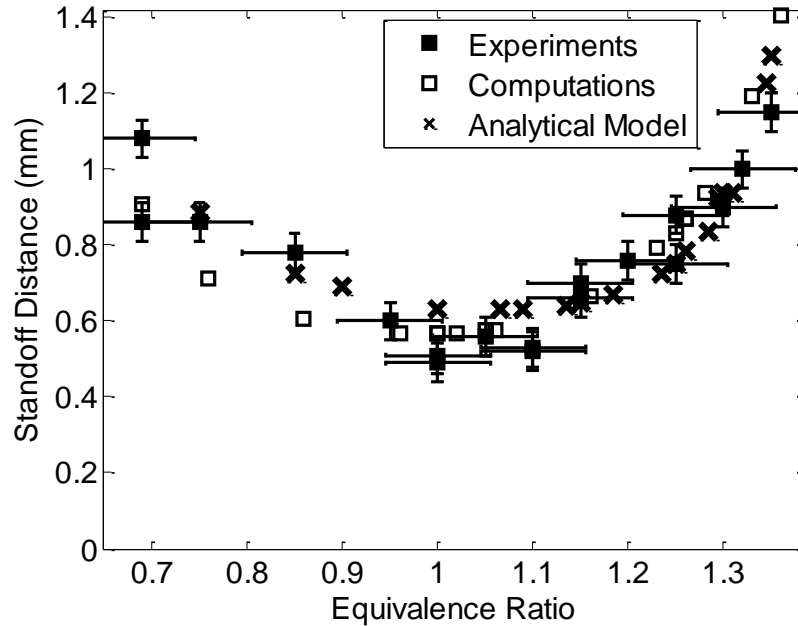


**Figure E.4: Standoff distance vs. equivalence ratio at inlet velocity =  $15 \pm 0.2$  cm/s**

### Flame Temperature

Simulations of burner-stabilized flames are often conducted using experimental temperature profiles as inputs rather than solving the energy equation for the temperature profile. In our case, the energy equation was solved and the temperature profile was a simulation output. The model results for flame temperature were compared to experimental data from published CARS measurements [27]. The maximum difference between the model prediction of flame temperature was 80 K and the average difference was 26 K at all conditions, from  $\phi = 1$  to 1.4 and inlet velocities from 7 to 15 cm/s.

### Limit conditions

In practice a flat flame can be stabilized on the burner, and if the velocity is increased the standoff distance decreases. At some velocity, the standoff distance is minimum, and a further small ( $\sim 1$  cm/s) increase of the inlet velocity causes the flame to lose its flatness. Further increase always results in the flame becoming less flat either forming corrugated or cellular shapes as described in the literature [40] or under very rich conditions forming more of a cone or dome shape (Figure E.2 is an example) sometimes with an inversion in the center.

As described previously, the intention of this study is to understand the behavior of flat flames and 1-D numerical models only. In the burner-stabilized flame simulations, as the velocity is increased there is a velocity beyond which a converged solution is not obtained, and converged solutions should not be obtained under conditions where stable, flat flames are not observed experimentally. The comparison between the experimental limiting conditions and the maximum velocities for which converged solutions to the burner stabilized flame simulation is shown in Fig. E.5. Additionally, as described in the literature, flames stabilized on a McKenna-type burner should become non-flat when the flame is nearly adiabatic [31, 40]. Therefore the experimental limiting conditions are also compared to the calculated laminar flame speeds in Fig. E.5. Throughout the range of equivalence ratios, the match between the experiments and burner-stabilized flame computations is very good. From  $\phi = 0.6$  to  $\phi \approx 1.2$  the flame loses its flatness below the laminar flame speed especially near stoichiometric. When  $\phi$  is moderately rich, the flame loses its flatness at an inlet velocity near the laminar flame speed, but then at lower inlet velocities in comparison to the laminar flame speed as the equivalence ratio approaches the maximum value tested ( $\phi \approx 1.6$ ).

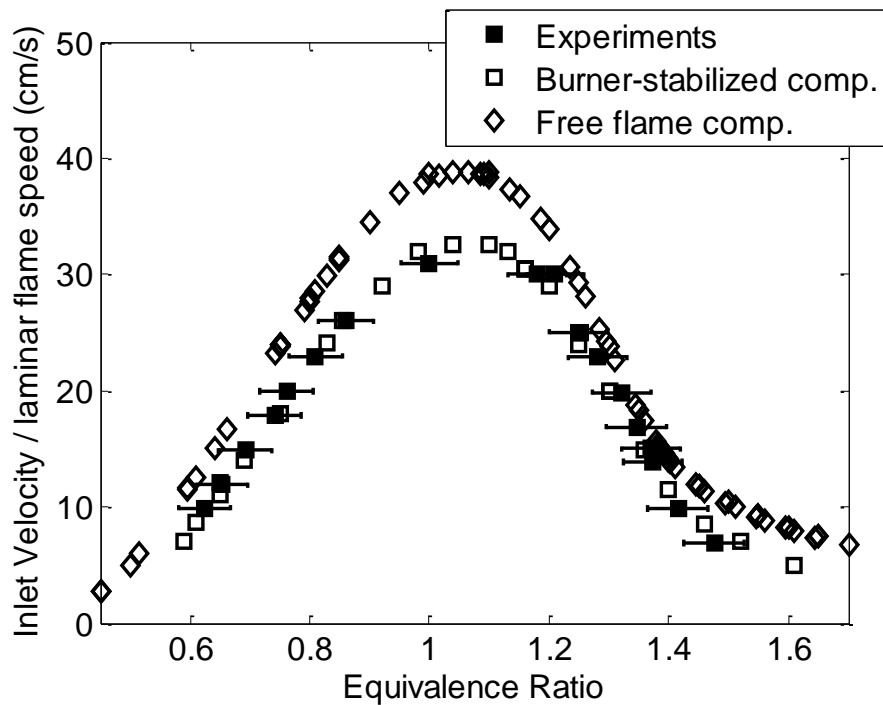


**Figure E.5: Limit inlet velocity and laminar flame speed vs. equivalence ratio**

These comparisons indicate that the computational model predicts flame standoff distance and temperature across a broad range of  $\phi$ . In addition, the limit velocities for the experiments show excellent agreement with the velocities of maximum convergence for the burner-stabilized flame model. The laminar flame speeds exceed the limit velocities determined experimentally under

lean and near stoichiometric conditions, but not as substantially under richer conditions, which are the focus of this paper. These comparisons establish confidence that the models can be used to predict the behavior of burner-stabilized flames especially at rich conditions.

**Effect of preheating on the conversion of rich mixtures to syngas**

To provide a baseline for comparison to the results for flames with preheated reactants, experiments and simulations were conducted with reactants at standard conditions. These data are important also to complete the comparison between the models and experiments and to establish the similarity between the two burners used experimentally. Then data are presented for experiments and modeling of burner-stabilized flames with preheated reactants to show the effect of preheat on syngas production.

**Comparison of McKenna and ceramic burner at baseline (unheated) conditions**

As was discussed previously, the McKenna burner cannot withstand the preheat temperatures of interest in this study so we constructed a ceramic burner for this purpose. In Fig. E.6, the concentrations of H<sub>2</sub>, CO and CO<sub>2</sub> are shown for experiments with both burners as well as predictions from burner-stabilized flame simulations, freely-propagating flame simulations, and equilibrium calculations. The error bars shown in Fig. E.6 are the maximum uncertainties in the presented experimental data. The average uncertainty in the concentration measurements are as follows: ±0.29 for [H<sub>2</sub>], ±0.32 for [CO], ±0.4 for [CO<sub>2</sub>].

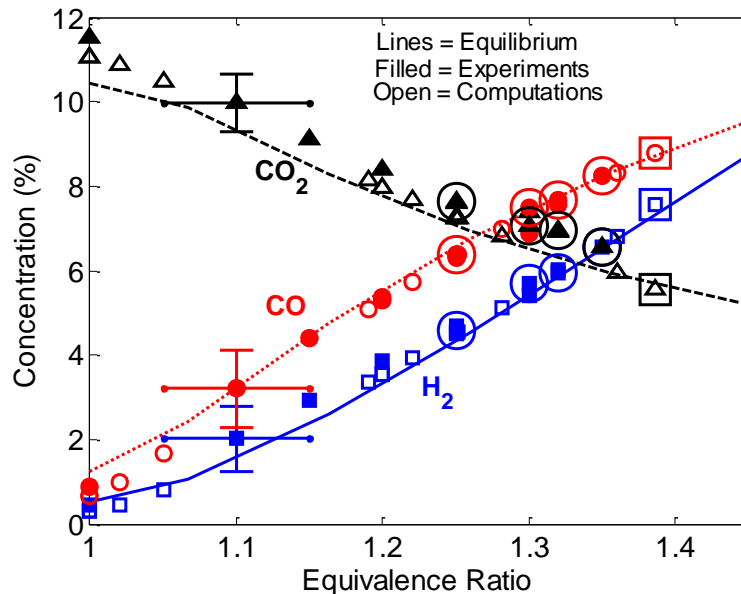


**Figure E.6: Concentration vs. equivalence ratio at inlet velocity = 15 ± 0.2 cm/s (circled points indicate ceramic burner data, all computational data are from burner-stabilized flame model except boxed points indicating free flame computations at  $\phi = 1.38$ )**

As Fig. E.6 shows, the experimental data from both reactors and the models match in concentration extremely well over the tested range of  $\phi$ . The ceramic burner has a flashback limit, so data are presented for  $\phi$  from 1.25 to 1.35 where flat flames were stabilized on the surface of the burner. At stoichiometric conditions, very nearly all of the carbon in methane is converted to CO<sub>2</sub> and little CO is observed. As  $\phi$  increases, the amount of carbon converted to CO<sub>2</sub> decreases as the amount converted to CO increases. Negligible amounts of small hydrocarbons were measured by the GC. Therefore, as  $\phi$  is increased, more hydrogen in methane is converted to H<sub>2</sub> at the expense of H<sub>2</sub>O. Both computations and experiments showed very nearly equilibrium levels of CO<sub>2</sub>, CO and H<sub>2</sub>. Lastly, the concentration of syngas increases monotonically with  $\phi$  suggesting that even richer  $\phi$  might improve syngas production if stable operation could be accomplished.

Concentrations for CO, CO<sub>2</sub> and H<sub>2</sub> are almost identical to the equilibrium values and are consistent with the trend of species concentrations seen in the burner-stabilized flame experiments and models. In the experiments if  $\phi$  is increased, the standoff distance increases, but the flame remains flat (burner-stabilized) until the  $\phi \approx 1.32$  on the McKenna burner and  $\phi \approx 1.35$  on the ceramic burner. When  $\phi$  is increased further, the flame becomes unstable because the laminar flame speed of the mixture approaches  $V$ ; under this condition the flame can be considered nearly adiabatic, and the predictions of the freely-propagating flame model become appropriate for comparison. At 300 K, a free flame of methane and air has a laminar flame speed of 15 cm/s when  $\phi \approx 1.38$ .

We measured species concentrations while varying  $V$  and holding  $\phi$  constant at 1.25 to determine if the two burners and the model results were consistent across a range of  $V$ . These data are shown in Fig. E.7.

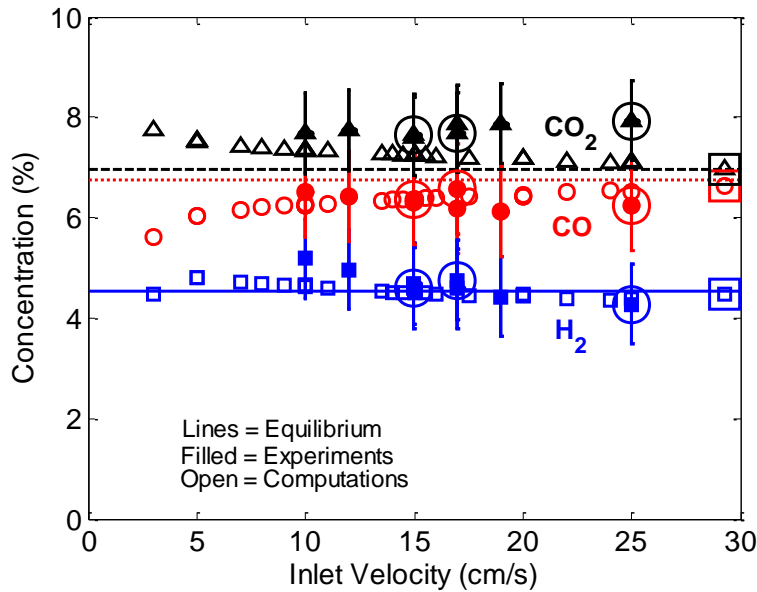


**Figure E.7: Concentration vs. inlet velocity at equivalence ratio =  $1.25 \pm 0.05$  (circled points indicate ceramic burner data, all computational data are from burner-stabilized flame model except boxed points indicating free flame computations at  $V = 29$  cm/s)**

The computations predict almost no change in species concentration as a function of  $V$  in the range of inlet velocities that were tested experimentally. However, at very low inlet velocities the computations predict that more methane is converted to  $\text{CO}_2$  at the expense of  $\text{CO}$ . The experiments show almost no change in concentration for both the McKenna burner and the ceramic burner. The equivalence ratio strongly affects species concentrations, as shown in Fig. E.6, and there is uncertainty in  $\phi$  for all experimental data points when  $V$  is varied and  $\phi$  is held constant. The uncertainties in species concentration due to uncertainty in  $\phi$  around  $\phi = 1.25$  are estimated as follows:  $\pm 0.8$  for  $[\text{H}_2]$ ,  $\pm 0.9$  for  $[\text{CO}]$  and  $\pm 0.8$   $[\text{CO}_2]$ . Because of these uncertainties, which are shown in Fig. E.7 because they are larger than the raw measurement uncertainty, no variation in the experimental data as a function of inlet velocity is implied in Fig. E.7.

The major conclusions from the previously presented data are that the ceramic burner and the McKenna burner produce nearly identical species concentrations across a range of  $\phi$  and  $V$ . In addition, the burner-stabilized flame model and the free flame model were very accurate in predictions of standoff distance, limit conditions and  $[\text{CO}]$ ,  $[\text{CO}_2]$  and  $[\text{H}_2]$  at all  $\phi$  and  $V$  tested.

*Results from experiments and modeling with preheated reactants*

Using the ceramic burner, we performed experiments with preheated reactants. Fig. E.8 shows concentration as a function of  $\phi$  with  $V$  held constant at 25 cm/s and the reactants preheated to 617 K. Under unheated conditions on the ceramic burner for  $V = 25$  cm/s the limit  $\phi$  is 1.26.

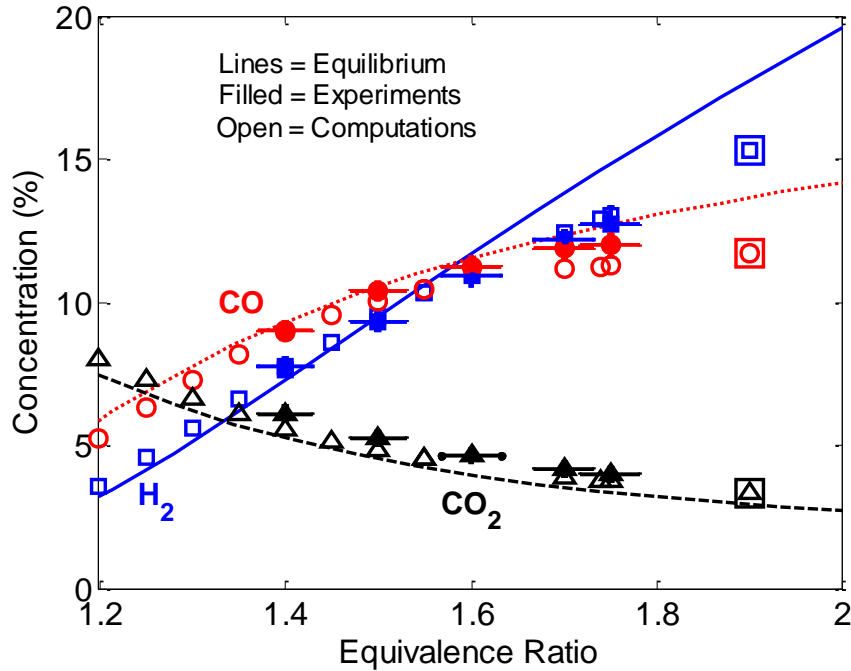


**Figure E.8: Concentration vs. equivalence ratio at inlet velocity =  $25 \pm 0.05$  cm/s and reactant temperature =  $617 \pm 10$  K (all computational data are from burner-stabilized flame model except boxed points indicating free flame computations at  $\phi = 1.9$ , uncertainty in temperature is  $\pm 10$  K)**

The burner-stabilized flame model matches the experimental data very closely. Under this preheat condition, a stable flame was obtained up to  $\phi = 1.75$ , which is greater than the conventional flammability limit of 1.67 and significantly greater than the operating limit observed when reactants were unheated ( $\phi = 1.26$ ). The maximum [H<sub>2</sub>] and [CO] achievable under unheated conditions at  $V = 15$  cm/s were 6.5% and 8.3%, respectively, both occurring at  $\phi = 1.35$  as shown in Fig. E.5. With reactants preheated, the maximum [H<sub>2</sub>] was 12.7% and the maximum [CO] was 12%. These data show that preheating significantly extends the operating range of burner-stabilized flames such that the stable burning of mixtures that produce high syngas yields can be achieved. The data also show that the burner-stabilized flame model produces very good predictions of species at  $\phi$  even beyond the rich flammability limit.

It has been shown that the limiting conditions for the experiments, the burner stabilized flame model and the laminar flame speed/equivalence ratio pairs were nearly coincident for flames with unheated reactants. As shown in Fig. E.8 with reactants preheated to 617 K the limiting

equivalence ratio ( $\phi = 1.75$ ) for a converged solution with the burner-stabilized flame model is nearly identical to the experimental value as well. However, the mixture equivalence ratio ( $\phi = 1.9$ ) having a flame speed of 25 cm/s was significantly greater than the experimental and model limit for the burner-stabilized flame.

A difference between these data and the data with unheated reactants is that the experimental results and the computational results do not match the equilibrium values at the highest values of  $\phi$ . Up to the maximum achievable  $\phi$  for the burner-stabilized flame, the experiments and the model concentrations are very close to equilibrium for [CO<sub>2</sub>], however [CO] begins to diverge from equilibrium slightly and [H<sub>2</sub>] begins to diverge significantly when  $\phi$  is greater than about 1.4. This divergence is somewhat unexpected since preheating should increase the rate at which the mixture reaches equilibrium relative to unheated conditions. However, under the preheated conditions, the  $\phi$  that were accessible were all relatively high ( $\phi > 1.4$ ); at high  $\phi$  the heat release is low, thus slowing the kinetic processes, and the relatively slow water-gas shift reaction becomes important. Even though preheating increases the range of accessible  $\phi$  by increasing reaction rates, the reaction rate increase is not great enough to allow full equilibration of the mixture. At very rich equivalence ratios, the relatively slow steam reforming reaction becomes important. Lastly, the freely-propagating flame model shows even more substantial divergence from equilibrium for both [CO] and [H<sub>2</sub>] while [CO<sub>2</sub>] remains very close to the equilibrium value. The concentrations for the freely-propagating flame are consistent with the trend in concentration for the burner-stabilized flame. However, the difference between the limit  $\phi$  for the burner-stabilized flame model and experiment and the  $\phi$  having a flame speed of 25 cm/s casts doubt on the accuracy of the freely-propagating flame model under this preheated condition.

The effect of reactant temperature was investigated by preheating reactants while the equivalence ratio was held at 1.4 and the inlet velocity was held at 24 cm/s (Fig. E.9). The minimum temperature at which a stable flame was observed for these conditions was 365 K, and the maximum temperature to which reactants were preheated in experiments was 630 K.

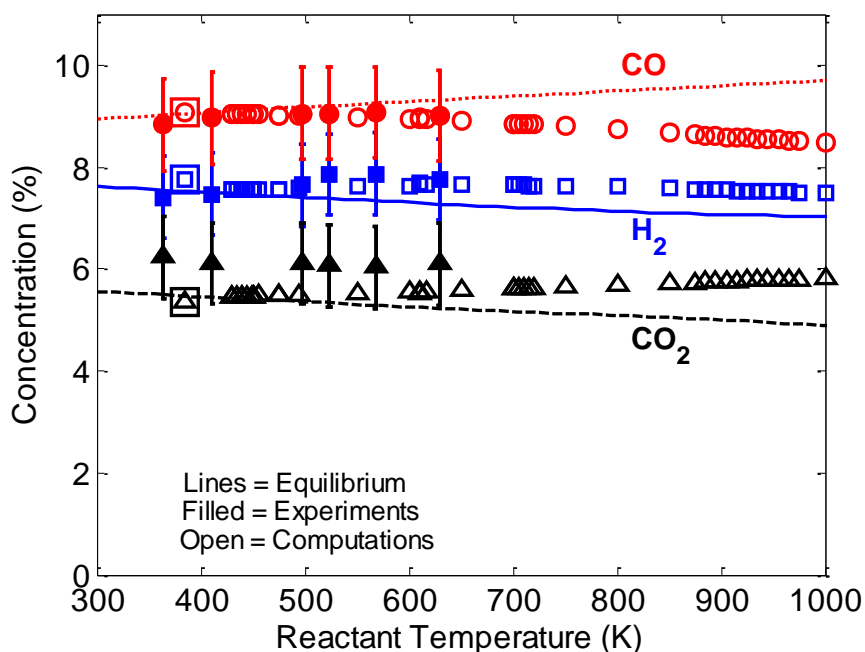


**Figure E.9: Concentration vs. reactant temperature at inlet velocity =  $24 \pm 2$  cm/s and equivalence ratio =  $1.4 \pm 0.05$  (all computational data are from burner-stabilized flame model except boxed points indicating free flame computations at temperature = 385 K)**

In the range of temperature where there was overlap between the experiments and computations, the computations predicted [H<sub>2</sub>] and [CO] very well while under-predicting [CO<sub>2</sub>] slightly. As was shown in all of the previously presented data, the experimental results, burner-stabilized flame model and freely-propagating flame model had species concentrations nearly identical to the equilibrium values at unheated conditions. As the preheat temperature increases beyond 700 K, the difference between equilibrium and the burner-stabilized flame model increases for both [CO] and [CO<sub>2</sub>], however the difference between the model and equilibrium in terms of [H<sub>2</sub>] does not increase significantly with temperature. Lastly, the overall yield of syngas ([H<sub>2</sub>] and [CO]) remains constant with preheat temperature indicating that preheating is important for stabilizing a reaction, but not for improving syngas yield. The concentration uncertainties shown in this plot are due to uncertainty in equivalence ratio because these uncertainties are larger than the raw measurement uncertainties.

The minimum temperature at which a solution converged with the burner-stabilized flame model was within 90 K of the limit temperature, which is the minimum temperature at which a stable, flat flame was observed experimentally. The preheat temperature at which the freely-propagating flame model reported a flame speed of 25 cm/s was within 20 K of this limit temperature. The coincidence of this temperature amongst the models is another indication that the models are accurate in their prediction of flame characteristics at low reactant temperature conditions.

## E.5 Concluding Remarks

An experimental and modeling study of burner-stabilized flames was conducted to understand the effect of preheat on syngas production. First experiments were conducted with unheated reactants so that confidence in the models could be gained for their prediction of combustion characteristics, especially species yields, at high equivalence ratios. The effect of preheat was investigated by preheating reactants up to 630 K while holding the inlet velocity and equivalence ratio constant.

The results showed that the burner stabilized flame model accurately predicts standoff distance, limit conditions and species yields for experiments with flat flame burners. Experiments with preheated reactants demonstrated that the operating limits for a flat flame burner increase substantially with increased reactant temperature, allowing the stable operation of the burner at richer equivalence ratios—where syngas yields are greater—than those achievable with unheated reactants. The specific effect of inlet temperature was investigated, and it was found that inlet temperature did not affect the yield of syngas under the tested range of temperatures. Burner-stabilized flames with preheated reactants showed deviations from equilibrium results in terms of species yields, in contrast with unheated conditions where equilibrium predicts species yields for burner-stabilized flames very well. The burner-stabilized flame model was able to predict the deviation from equilibrium when reactants were preheated to ~630 K. At high preheat temperatures, the limiting operating conditions of the experiment were well-predicted by the burner-stabilized flame model but not by the laminar flame speed.

These results have important implications with regards to heat recirculating reactors. First, the models, and therefore the kinetics mechanism, performed very well up to richest equivalence ratio examined of 1.75, which exceeds the conventional rich flammability limit. The only significant difference between the models and the experiments was the difference between the limit equivalence ratio and the equivalence ratio where the laminar flame speed was 25 cm/s when the reactants were preheated to 617 K. This means that those working on reactor models for rich combustion should have confidence in GRI3.0 for predicting syngas production even beyond the rich flammability limit. In heat-recirculating reactors, preheat is accomplished by transport enhancement, which occurs in proximity to the reaction zone, as part of the reactor design. In the experiments described here, the preheat occurred far upstream of the reaction zone and was input from an external source. This experimental design provided a means to study the effect of preheat temperature independent of enhanced transport mechanisms and interaction with the reaction zone. The results show that preheat is necessary to attain stable operation at extreme equivalence ratios. This was the expected result since conditions (such as downstream propagation of the reaction zone in a filtration reactor) that enhance preheat have been observed in heat-recirculating reactors when mixtures expected to be unstable are burned. It was also found that further preheat does not enhance syngas production. This result aids in the design of

heat recirculating reactors because it indicates that maximal heat recirculation may not be necessary for conversion of fuel to syngas.

## E.6 References

1. Weinberg, F.J., *Combustion Temperatures: The Future?* Nature, 1971. 233: p. 239.
2. Jones, A.R., S.A. Lloyd, and F.J. Weinberg, *Combustion in Heat Exchangers*. Proc. R. Soc. Lond. A, 1978. 360: p. 97-115.
3. Brenner, G., K. Pickenacker, O. Pickenacker, D. Trimis, K. Wawrzinek, and T. Weber, *Numerical and Experimental Investigation of Matrix-Stabilized Methane/Air Combustion in Porous Inert Media*. Combust. Flame, 2000. 123: p. 201-213.
4. Sathe, S.B., M.R. Kulkarni, R.E. Peck, and T.W. Tong, *An Experimental and Theoretical Study of Porous Radiant Burner Performance*. Proc. Combust. Inst., 1990. 23: p. 1011-1018.
5. Wood, S. and A.T. Harris, *Porous burners for lean-burn applications*. Progress in Energy and Combustion Science, 2008. 34(5): p. 667-684.
6. Kim, N.I., S. Kato, T. Kataoka, T. Yokomori, S. Maruyama, T. Fujimori, and K. Maruta, *Flame Stabilization and Emission of Small Swiss-Roll Combustors as Heaters*. Combust. Flame, 2005. 141: p. 229-240.
7. Al-Hamamre, Z., S. Voß, and D. Trimis, *Hydrogen production by thermal partial oxidation of hydrocarbon fuels in porous media based reformer*. International Journal of Hydrogen Energy, 2009. 34(2): p. 827-832.
8. Kennedy, L.A., J.P. Bingue, A.V. Saveliev, A.A. Fridman, and S.I. Foutko, *Chemical structures of methane-air filtration combustion waves for fuel-lean and fuel-rich conditions*. Proceedings of the Combustion Institute, 2000. 28(1): p. 1431-1438.
9. P. Bingue, J., A. V. Saveliev, A. A. Fridman, and L.A. Kennedy, *Hydrogen production in ultra-rich filtration combustion of methane and hydrogen sulfide*. International Journal of Hydrogen Energy, 2002. 27(6): p. 643-649.
10. Pedersen-Mjaanes, H., L. Chan, and E. Mastorakos, *Hydrogen production from rich combustion in porous media*. International Journal of Hydrogen Energy, 2005. 30(6): p. 579-592.
11. Pastore, A. and E. Mastorakos, *Rich n-heptane and diesel combustion in porous media*. Experimental Thermal and Fluid Science, 2010. 34(3): p. 359-365.
12. Koch, D.L., R.G. Cox, H. Brenner, and J.F. Brady, *The Effect of Order on Dispersion in Porous Media*. J. Fluid Mech, 1989. 200: p. 173-188.
13. Hackert, C.L., J.L. Ellzey, O.A. Ezekoye, and M.J. Hall, *Transverse Dispersion at High Peclet Numbers in Short Porous Media*. Exp. Fluids, 1996. 21: p. 286-290.
14. Dhamrat, R.S. and J.L. Ellzey, *Numerical and Experimental Study of the Conversion of Methane to Hydrogen in a Porous Media Reactor*. Combustion and Flame, 2006. 144: p. 698-709.

15. Schoegl, I. and J.L. Ellzey, *A mesoscale fuel reformer to produce syngas in portable power systems*. Proceedings of the Combustion Institute, 2009. 32(2): p. 3223-3230.
16. Drayton, M.K., A.V. Saveliev, L.A. Kennedy, A.A. Fridman, and Y. Li, *Syngas Production Using Superadiabatic Combustion of Ultra-Rich Methane-Air Mixtures*. Proc. Combust. Inst., 1998. 27: p. 1361-1367.
17. Dixon, M.J., I. Schoegl, C.B. Hull, and J.L. Ellzey, *Experimental and numerical conversion of liquid heptane to syngas through combustion in porous media*. Combustion and Flame, 2008. 154(1-2): p. 217-231.
18. Belmont, E., S.M. Solomon, and J.L. Ellzey, *Syngas Production from Heptane in a Non-catalytic Counterflow Reactor*. Combustion and Flame, 2012. In Press.
19. Barra, A.J. and J.L. Ellzey, *Heat Recirculation and Heat Transfer in Porous Burners*. Combust. Flame, 2004. 137: p. 230-241.
20. Ronney, P.D., *Analysis of Non-Adiabatic Heat-Recirculating Combustors*. Combust. Flame, 2003. 135: p. 421-439.
21. Chen, C.-H. and P.D. Ronney, *Three-dimensional effects in counterflow heat-recirculating combustors*. Proceedings of the Combustion Institute, 2010. 33(2): p. 3285-3291.
22. Mishra, S.C., M. Steven, S. Nemoda, P. Talukdar, D. Trimis, and F. Durst, *Heat transfer analysis of a two-dimensional rectangular porous radiant burner*. International Communications in Heat and Mass Transfer, 2006. 33(4): p. 467-474.
23. Khose-Hoinghaus, K. and J.B. Jeffries, eds. *Applied Combustion Diagnostics*. Combustion: An International Series. 2002, Taylor & Francis: New York.
24. Hansen, N., T.A. Cool, P.R. Westmoreland, and K. Kohse-Hoinghaus, *Recent contributions of flame-sampling molecular-beam mass spectrometry to a fundamental understanding of combustion chemistry*. Progress in Energy and Combustion Science, 2009. 35(2): p. 168-191.
25. Marinov, N.M., W.J. Pitz, C.K. Westbrook, M.J. Castaldi, and S.M. Senkan, *Modeling of Aromatic and Polycyclic Aromatic Hydrocarbon Formation in Premixed Methane and Ethane Flames*. Combustion Science and Technology, 1996. 116-117(1-6): p. 211-287.
26. Schoenung, M. and R.K. Hanson, *CO and Temperature Measurements in a Flat Flame by Laser Absorption Spectroscopy and Probe Techniques*. Combustion Science and Technology, 1980. 24(5-6): p. 227-237.
27. Weigand, P., R. Luckerath, and W. Meier, *Documentation of Flat Premixed Laminar CH<sub>4</sub>/Air Standard Flames: Temperatures and Species Concentrations*, D.I.o.C.T. ([http://www.dlr.de/vt/PortalData/29/Resources/dokumente/ch4\\_air\\_flames.pdf](http://www.dlr.de/vt/PortalData/29/Resources/dokumente/ch4_air_flames.pdf)), Editor. 2003: Stuttgart.
28. Gersen, S., A.V. Mokhov, and H.B. Levinsky, *Extractive probe/TDLAS measurements of acetylene in atmospheric-pressure fuel-rich premixed methane/air flames*. Combustion and Flame, 2005. 143(3): p. 333-336.

29. Kumar, K. and C.-J. Sung, *Laminar flame speeds and extinction limits of preheated n-decane/O<sub>2</sub>/N<sub>2</sub> and n-dodecane/O<sub>2</sub>/N<sub>2</sub> mixtures*. Combustion and Flame, 2007. 151: p. 209-224.
30. Liu, F.S. and O.L. Gulder, *Effects of pressure and preheat on super-adiabatic flame temperatures in rich premixed methane/air flames*. Combustion Science and Technology, 2008. 180(3): p. 437-452.
31. Bosschaart, K.J. and L.P.H. de Goey, *The laminar burning velocity of flames propagating in mixtures of hydrocarbons and air measured with the heat flux method*. Combustion and Flame, 2004. 136(3): p. 261-269.
32. Gibson, J., M. Ayoobi, and I. Schoegl, *Behavior of Preheated Premixed Flames at Rich Conditions*. Proc. Combust. Inst., 2012. 34(In Press).
33. Sepman, A., A.V. Mokhov, and H.B. Levinsky, *A laser-induced fluorescence and coherent anti-Stokes Raman scattering study of NO formation in preheated, laminar, rich premixed, methane/air flames*. Proceedings of the Combustion Institute, 2002. 29: p. 2187-2194.
34. Hidaka, Y., K. Sato, Y. Henmi, H. Tanaka, and K. Inami, *Shock-tube and modeling study of methane pyrolysis and oxidation*. Combustion and Flame, 1999. 118(3): p. 340-358.
35. Goodwin, D.G. (2012) *Cantera - An object-oriented software toolkit for chemical kinetics, thermodynamics, and transport processes*. <http://code.google.com/p/cantera/>
36. Smith, G.P., D.M. Golden, M. Frenklach, N.W. Moriarty, B. Eiteneer, M. Goldenberg, C.T. Bowman, R.K. Hanson, S. Song, J.W.C. Gardiner, V.V. Lissianski, and Z. Qin, *GRI-Mech 3.0 URL <http://www.me.berkeley.edu/gri-mech/version30/>*. 1999.
37. Law, C.K., *Combustion Physics*. 2006: Cambridge University Press.
38. Sutton, G., A. Levick, G. Edwards, and D. Greenhalgh, *A combustion temperature and species standard for the calibration of laser diagnostic techniques*. Combustion and Flame, 2006. 147: p. 39-48.
39. Mokhov, A.V. and H.B. Levinsky, *A LIF and cars investigation of upstream heat loss and flue-gas recirculation as NO<sub>x</sub> control strategies for laminar, premixed natural-gas/air flames*. Proceedings of the Combustion Institute, 2000. 28(2): p. 2467-2474.
40. Ferguson, C.R. and J.C. Keck, *Stand-off distances on a flat flame burner*. Combustion and Flame, 1979. 34: p. 85-98.
41. Kurdyumov, V.N. and M. Matalon, *The porous-plug burner: Flame stabilization, onset of oscillation, and restabilization*. Combustion and Flame, 2008. 153: p. 105-118.
42. Williams, B.A. and J.W. Fleming, *Comparison of species profiles between O<sub>2</sub> and NO<sub>2</sub> oxidizers in premixed methane flames*. Combustion and Flame, 1995. 100(4): p. 571-590.
43. Evertsen, R., J.A. Van Oijen, R.T.E. Hermanns, L.P.H. De Goey, and J.J. Ter Meulen, *Measurements of absolute concentrations of CH in a premixed atmospheric flat flame by cavity ring-down spectroscopy*. Combustion and Flame, 2003. 132: p. 34-42.